

Karlsruher Institut für Technologie

**Schriftenreihe**

**Kontinuumsmechanik im Maschinenbau**

22

**Juliane Lang**

---

Thermomechanical Modeling and  
Experimental Characterization of  
Sheet Molding Compound Composites



Juliane Lang

**Thermomechanical Modeling and  
Experimental Characterization of  
Sheet Molding Compound Composites**

**Schriftenreihe**  
**Kontinuumsmechanik im Maschinenbau**  
**Band 22**

Karlsruher Institut für Technologie (KIT)  
Institut für Technische Mechanik  
Bereich Kontinuumsmechanik

Hrsg. Prof. Dr.-Ing. habil. Thomas Böhlke

Eine Übersicht aller bisher in dieser Schriftenreihe erschienenen Bände  
finden Sie am Ende des Buchs.

# **Thermomechanical Modeling and Experimental Characterization of Sheet Molding Compound Composites**

by  
Juliane Lang

Karlsruher Institut für Technologie  
Institut für Technische Mechanik  
Bereich Kontinuumsmechanik

Thermomechanical Modeling and Experimental Characterization  
of Sheet Molding Compound Composites

Zur Erlangung des akademischen Grades einer Doktorin der  
Ingenieurwissenschaften von der KIT-Fakultät für Maschinenbau des  
Karlsruher Instituts für Technologie (KIT) genehmigte Dissertation  
von Juliane Lang, M.Sc.

Tag der mündlichen Prüfung: 23. Juni 2022  
Hauptreferent: Prof. Dr.-Ing. Thomas Böhlke  
Korreferent: Prof. Dr. Jeffrey T. Wood

#### Impressum



Scientific  
Publishing

Karlsruher Institut für Technologie (KIT)  
KIT Scientific Publishing  
Straße am Forum 2  
D-76131 Karlsruhe

KIT Scientific Publishing is a registered trademark  
of Karlsruhe Institute of Technology.  
Reprint using the book cover is not allowed.

[www.ksp.kit.edu](http://www.ksp.kit.edu)



*This document – excluding parts marked otherwise, the cover, pictures and graphs –  
is licensed under a Creative Commons Attribution-Share Alike 4.0 International License  
(CC BY-SA 4.0): <https://creativecommons.org/licenses/by-sa/4.0/deed.en>*



*The cover page is licensed under a Creative Commons  
Attribution-No Derivatives 4.0 International License (CC BY-ND 4.0):  
<https://creativecommons.org/licenses/by-nd/4.0/deed.en>*

Print on Demand 2023 – Gedruckt auf FSC-zertifiziertem Papier

ISSN 2192-693X  
ISBN 978-3-7315-1232-5  
DOI 10.5445/KSP/1000149634





# Zusammenfassung

Faserverstärkte Kunststoffe sind eine high-performance Materialklasse mit einem breiten Anwendungsspektrum. Die wichtigsten Eigenschaften sind hohe Festigkeit und Steifigkeit kombiniert mit geringer Dichte und kleiner thermischer und elektrischer Leitfähigkeit. Zwei spezielle Klassen von faserverstärkten Kunststoffen sind diskontinuierlich glasfaser-verstärkte Sheet Molding Compound (SMC) Verbundwerkstoffe und kontinuierlich kohlefaser-verstärkte SMC Verbundwerkstoffe. Erstere haben die Vorteile eines ökonomischeren Herstellungsprozesses und großer Flexibilität in der Formgebung, während letztere über eine höherer Festigkeit und Steifigkeit verfügen. In dem internationalen Graduierten Kolleg GRK 2078 wird eine neue Materialklasse betrachtet, die diese beiden Materialklassen kombiniert um die Vorteile beider zu vereinen. Die Forschung der vorliegenden Arbeit ist eingebettet in dieses Projekt mit Fokus auf das diskontinuierliche SMC.

Das Ziel dieser Arbeit ist die Modellierung und experimentelle Charakterisierung des anisotropen temperaturabhängigen thermomechanischen Verhaltens des diskontinuierlich glasfaser-verstärkten SMC Verbundwerkstoffs auf der Makroskala unter Berücksichtigung der Mikrostruktur. Dies führt zu drei Hauptthemen, die eng miteinander verknüpft sind: Materialmodellierung, experimentelle Untersuchungen und die Kombination von beidem um die Materialparameter zu identifizieren und das Modell zu validieren.

Bei der Modellierung wird zunächst das linear elastische anisotrope Materialverhalten durch ein thermodynamisch konsistentes Materialmodell beschrieben. Dies beinhaltet die folgenden Material-

Koeffizienten: Steifigkeit/Nachgiebigkeit, thermischer Ausdehnungs-/Spannungs-Koeffizient, Wärmekapazität, Wärmeleitfähigkeit. Es werden zwei Varianten des Modells präsentiert, eine mit konstanten Koeffizienten und eine mit temperaturabhängigen Koeffizienten. Das Versagens-Verhalten wird mittels eines Tsai-Wu Versagenskriteriums modelliert, wodurch unter anderem Anisotropie berücksichtigt wird. In einem nächsten Schritt wird für beide Modelle die Mikrostruktur mit einbezogen. Die gerichteten thermoelastischen Material-Koeffizienten und die Versagens-Koeffizienten werden linear in Faserorientierungstensoren ausgedrückt.

Die temperaturabhängigen thermoelastischen Materialeigenschaften werden mit Hilfe von Experimenten an verschiedenen Prüfständen bestimmt. Um Anisotropie zu untersuchen werden die Versuche in unterschiedlichen Richtungen durchgeführt. Schädigung und Versagen werden untersucht, indem Zugversuche an uniaxialen und speziellen biaxialen Proben durchgeführt werden. Die Verknüpfung zur Mikrostruktur wird hergestellt, indem Proben mit einer gemittelten bekannten Faserorientierung betrachtet werden. Diese Mikrostruktur-Informationen stammen aus Mikro-CT Scans.

Die Parameter der Materialmodelle werden durch Experimente und CT-Informationen bestimmt. Um den gesamten Prozess zu validieren werden exemplarische Proben untersucht. Aus den Materialmodellen, welche die identifizierten Parameter enthalten, und der Mikrostrukturinformation zu diesen exemplarischen Proben werden alle betrachteten Materialeigenschaften berechnet und anschließend mit experimentellen Ergebnissen verglichen. Der ganzheitliche Umgang mit Modellierung und Experimenten stellt einen besonderen Fokus dieser Arbeit dar.

# Summary

Fiber reinforced plastics are a high-performance class of materials with a wide range of applications. The most important properties are high strength and stiffness combined with low density and low thermal and electrical conductivity. Two special classes of fiber reinforced plastics are discontinuous glass fiber reinforced sheet molding compound (SMC) composites and continuous carbon fiber reinforced SMC composites. The former have the advantages of more economical manufacturing process and greater flexibility in shaping, while the latter possess higher strength and stiffness. In the international research training group (IRTG) GRK 2078 a new material class that combines these two classes of materials to merge the advantages of both. The research of the present thesis is embedded in this IRTG project focusing on discontinuous SMC.

The aim of this work is to model and experimentally characterize the anisotropic temperature-dependent thermomechanical behavior of SMC composites on the macroscale with consideration of the microstructure. This leads to three main topics which are closely connected: material modelling, experimental investigations, and the combination of both to identify the material parameters and validate the model.

For the modeling, the linear elastic anisotropic thermomechanical material behavior is described first by a thermodynamically consistent material model. This includes the following material coefficients: stiffness/compliance, thermal expansion/stress coefficient, heat capacity, thermal conductivity. Two variants of the model are presented, one

with constant coefficients and one with temperature-dependent coefficients. The failure behavior is modeled by means of a Tsai-Wu failure criterion, which also takes anisotropy into account. In a next step, the microstructure is taken into account. The directional thermoelastic material coefficients and the failure coefficients are expressed linearly in terms of fiber orientation tensors.

The temperature-dependent thermoelastic material properties are determined by means of experiments with different testing devices. To account for anisotropy, the experiments are executed in different material directions. Damage and failure are investigated by performing tensile tests on uniaxial and special biaxial specimens. The connection to microstructure is accomplished by considering specimens with an averaged known fiber orientation. This microstructure information is obtained from micro-CT scans.

The parameters of the material models are determined by experiments and CT information. In order to validate the whole process, sample specimens are investigated. From the material models, containing the identified parameters, and the microstructure information of these sample specimens, all considered material properties are calculated and subsequently compared with experimental results. The holistic approach of modeling and experiments is a special focus of this work.

# Acknowledgments

First of all, I would like to thank my supervisor Thomas Böhlke for giving me the opportunity to work, teach, and do research at the Institute of Engineering Mechanics (ITM), as well as for supervising my doctoral thesis, where I had support and freedom at the same time, the former mainly in the field of material modeling and the latter mainly in the field of experimental investigations. I would also like to thank him for his interesting lectures that shaped my studies from the beginning (TM1 was my "favorite" subject). A great thanks goes to Jeff Wood, my co-supervisor, especially for the inspiring discussions in experimental mechanics that he contributed to with his vast knowledge and creativity. I would like to thank Britta Nestler for chairing the committee, which she did in a very pleasant manner.

I also want to thank the team at ITM. In the following I want to mention a few by name: My first room colleague, Rudolf, for our "Sinfonie- und Harmonie-Büro", making the best beginning I could have; Barthel, for sharing his large knowledge about testing devices and for teaching me a passion for the experimental realm in the cellar already years ago; Malte for leading me to the institute via my master thesis; Alex for the common interest in experiments and the pleasant cooperation in teaching engineering mechanics; Julian for the support and cooperation in all technical matters; Ute und Helga for best organization, and conversations on non-mechanical topics; Tom for everything (PC, teaching, organization, ...) and the very pleasant cooperation and communication. I would also like to thank my colleagues from the IRTG project for the excellent collaboration; in

particular Ludwig Schöttl for providing CT-Scans; Julian Bauer for the collaboration and discussions where we similarly attempted to achieve a deep understanding of the research content and for making me aware of the importance of git and similar things, Sergej Illinzeer for producing SMC plates, Miriam Bartkowiak for the pure resin material, Jannis Langer for milling the cruciform specimens. I want also to thank Florian for spontaneous support in manufacturing specimens. I would like to thank my students Carola, Johanna and Fabian for the fruitful and pleasant cooperation and the endless hours in the basement laboratory.

I want to thank my friends for their support in a wide variety of ways and for accepting that I had barely time during the completion of my dissertation, my flatmates for cooking for me and being there, especially in home office times. I would like to thank Kai, for supporting me both emotionally as well as practically. I am really fortunate that I had him by my side during the completion of this dissertation. I want to thank my family; Illa for her thoughtful support from afar during my defense and her interest in my field of study; Reinhart for the words "aus dir wäre eine gute Ingenieurin geworden" during my medicine studies; my mum and dad for supporting me during my studies and doctoral dissertation and for giving me a childhood that gave me the chance to be interested, curious, creative and open minded; and my sister just for being my sister and for making me laugh even in very stressful times.

The research documented in this doctoral thesis has been funded by the German Research Foundation (DFG) within the International Research Training Group Integrated engineering of continuous-discontinuous long fiber reinforced polymer structures (IRTG 2078). The support is gratefully acknowledged. We acknowledge support by the KIT-Publication Fund of the Karlsruhe Institute of Technology.

Karlsruhe, May 2023

Juliane Lang

# Contents

<b>Zusammenfassung</b> . . . . .	i
<b>Summary</b> . . . . .	iii
<b>Acknowledgments</b> . . . . .	v
<b>1 Introduction</b> . . . . .	1
1.1 Motivation . . . . .	1
1.2 Research Objectives and Originality of this Thesis . . . . .	5
1.2.1 Research Objectives of this Thesis . . . . .	5
1.2.2 Originality of this Thesis . . . . .	7
1.3 State of the Art . . . . .	9
1.4 Structure of this Thesis . . . . .	18
1.5 Acronyms, Symbols, Notation and Operators . . . . .	20
1.5.1 Symbols and Abbreviations . . . . .	20
1.5.2 Notation and Operations . . . . .	24
<b>2 Fundamentals</b> . . . . .	27
2.1 Materials . . . . .	27
2.1.1 Discontinuous Glass Fiber Reinforced SMC Composites . . . . .	27
2.1.2 Continuous Carbon Fiber Reinforced SMC Composites . . . . .	31
2.1.3 Continuous-Discontinuous Fiber Reinforced SMC Composites . . . . .	31
2.1.4 Materials used in this Thesis . . . . .	32

2.2	Continuum Mechanics . . . . .	35
2.2.1	Kinematics . . . . .	35
2.2.2	Balance Equations . . . . .	37
2.2.3	Material Theory . . . . .	41
2.3	Damage and Failure . . . . .	48
2.3.1	Damage . . . . .	48
2.3.2	Failure . . . . .	51
2.4	Note on Viscoelasticity . . . . .	52
2.5	Micromechanics . . . . .	58
2.5.1	Microstructure of Fiber Reinforced Composites . . . . .	58
2.5.2	Fiber Orientation Distribution . . . . .	59
2.5.3	Fiber Orientation Tensors . . . . .	60
<b>3</b>	<b>Material Model . . . . .</b>	<b>63</b>
3.1	Thermoelastic Modeling . . . . .	63
3.1.1	Thermoelasticity with Constant Coefficients . . . . .	63
3.1.2	Thermoelasticity with Temperature-Dependent Coefficients . . . . .	68
3.2	Micromechanical Modeling of Thermoelasticity . . . . .	75
3.2.1	Constant Coefficients . . . . .	75
3.2.2	Temperature-Dependent Coefficients . . . . .	77
3.3	Modeling of Failure . . . . .	78
3.4	Micromechanical Modeling of Failure . . . . .	81
<b>4</b>	<b>Experimental Investigations . . . . .</b>	<b>83</b>
4.1	Experimental Facilities . . . . .	83
4.1.1	Biaxial Testing Device . . . . .	83
4.1.2	Dynamical Mechanical Analysis . . . . .	85
4.1.3	Dilatometer . . . . .	87
4.1.4	Laser Flash Analysis . . . . .	88
4.2	Specimens . . . . .	90

4.3	Thermoelastic Material Parameters . . . . .	93
4.3.1	Introducing Remarks and Data Evaluation . . . . .	93
4.3.2	Stiffness . . . . .	95
4.3.3	Thermal Expansion . . . . .	98
4.3.4	Thermal Diffusivity . . . . .	101
4.3.5	Heat Capacity . . . . .	105
4.3.6	Thermal Conductivity . . . . .	108
4.4	Damage and Failure . . . . .	112
4.4.1	Damage . . . . .	112
4.4.2	Failure . . . . .	128
4.5	Additional Investigations . . . . .	133
4.5.1	Biaxial Specimen Design Investigations . . . . .	133
4.5.2	DIC Investigations . . . . .	136
4.5.3	Comparison of Viscoelastic and Damage Effect on Stiffness of SMC . . . . .	138
4.6	Summary and Discussion of Experimental Results . . . . .	141
<b>5</b>	<b>Parameter Identification - Merging Modeling and Experiments . . . . .</b>	<b>145</b>
5.1	Thermoelastic Model . . . . .	145
5.1.1	Introducing Remarks . . . . .	145
5.1.2	Constant Coefficients . . . . .	146
5.1.3	Temperature-Dependent Coefficients . . . . .	155
5.2	Micromechanical Thermoelastic Model . . . . .	163
5.2.1	Introducing Remarks . . . . .	163
5.2.2	Stiffness . . . . .	164
5.2.3	Coefficient of Thermal Expansion . . . . .	167
5.2.4	Thermal Diffusivity and Conductivity . . . . .	170
5.2.5	Remark on Micromechanical Temperature Dependent Thermoelastic Model . . . . .	172
5.3	Failure Model . . . . .	172
5.4	Micromechanical Failure Model . . . . .	176

5.5	Summary and Discussion of Results . . . . .	180
5.5.1	Thermoelastic Model . . . . .	180
5.5.2	Micromechanical Thermoelastic Model . . . . .	182
5.5.3	Failure Model . . . . .	184
5.5.4	Micromechanical Failure Model . . . . .	185
<b>6</b>	<b>Applications</b> . . . . .	<b>187</b>
6.1	Thermoelasticity . . . . .	187
6.2	Failure . . . . .	191
<b>7</b>	<b>Summary and Conclusion</b> . . . . .	<b>193</b>
<b>A</b>	<b>Appendix</b> . . . . .	<b>201</b>
A.1	Specimen Designation . . . . .	201
A.2	Preliminary Study on Dilatometer Measurements . . . . .	202
A.3	Statistics . . . . .	203
A.3.1	Statistical Quantities . . . . .	203
A.3.2	Boxplot Representation . . . . .	204
A.4	Values of the Optimized Material Parameters . . . . .	206
A.4.1	Thermoelasticity . . . . .	206
A.4.2	Micromechanical Modeling of Thermoelasticity . . . . .	207
A.4.3	Micromechanical Failure Modeling . . . . .	208
A.5	Additional Tables Parameter Identification of Micromechanical Failure Model . . . . .	208
A.6	Orientation Tensors of Specimens . . . . .	211
	<b>Bibliography</b> . . . . .	<b>213</b>

## Chapter 1

# Introduction

## 1.1 Motivation

Fiber reinforced composite materials are a very versatile high-performance class of materials with a broad range of applications. The overall benefits are a high strength and stiffness combined with low density, making fiber reinforced materials an ideal lightweight construction material. They consist of fibers, which mainly carry the load, and a matrix material, which holds the fibers in place and determines the shape of the component.

Variation possibilities lie in fiber shapes and alignments, in different material combinations and different manufacturing processes. There are discontinuous (short, long) and continuous (endless) fibers which can be aligned or randomly distributed and oriented. Standard polymers such as thermosets and thermoplastics are commonly used as matrix materials, and glass or carbon fibers are most commonly used as fiber materials. But also recyclable polymers or polymers from renewable resources as matrix and natural fibers such as bamboo or wood fibers are gaining importance in connection with an increasing environmental awareness (Reddy, 2015). In manufacturing, there are various options, e.g., hot pressing of semi-finished products or injection molding.

One special fiber composite material class, mainly considered in this thesis, are sheet molding compound (SMC) composites. They belong to

the discontinuous long fiber reinforced plastics (DiCoFRPs) and consist, as standard, of a thermoset polymer as matrix and, in most cases, of glass or carbon fibers. The matrix can be mixed with additional components to change the properties, as for example mechanical properties or color. In recent developments also bio plastic and natural fibers are used and investigated (Mehta et al., 2005). In addition to the general properties of fiber reinforced materials mentioned above, SMC composites have further particularly pronounced benefits. These are low and economical manufacturing efforts and costs, the flexibility in shaping also for filigree parts, the high surface quality, thermal and electrical properties and resistance against external conditions. Furthermore, these characteristics can be adapted by different material combinations and compositions.

This leads to many different application fields, some of which are mentioned in the following (Murali et al. (2013), Reyers (2018), Mehta et al. (2005)):

- Electric and electronics: Due to the electrical and thermal isolating properties (dielectrical strength, low temperature diffusivity) and high temperature resistance, many parts protecting sensitive electrical output devices are made of SMC. This application field is becoming increasingly important because of the growing market in in electric and electronics.
- Renewable energy applications: Typical components in which SMC can also be used are, for example, solar power tiles. In addition to the electrical properties, SMC has also a high resistance to enviromental influences, notably to UV radiation.
- Transportation: Currently, mainly non-structural parts in the automotive and other transportation sectors are made of SMC. Using SMC as a typical lightweight material to replace metals reduces the total weight and thus lowers emissions and energy consumption.

- Medical applications: SMC delivers many material characteristics for the application as instrumental components in medical science. These are the adaptability of the material properties, which often have to be very specific in medical technology, the flexibility in filigree shaping and the resistance to high temperature and disinfectants for sterile parts.
- Building: Construction components must be durable for long time periods and maintain an aesthetically pleasant appearance, even when exposed to environmental influences as UV, moisture and temperature changes. Additionally the fire resistance of SMC composites plays an important role.
- Further: There are also some niche fields in which SMC composites are used. More common is the use for sports equipment, but there are also applications in artistic fields, for example for design furniture or modern musical instruments.

Research possesses permanent relevance according to the constantly developing compositions and characteristics of SMC composites. Apart from this, also in the already well known material compositions, there is still a lack of understanding of the complex material behavior of SMC composites, concerning the anisotropic behavior induced by the complex microstructure, damage and failure behavior and temperature-dependent properties. The complete understanding is very important to ensure a high reliability, e.g., for the use also as structural parts in transportation or a wider use in medical science. Furthermore via good dimensioning a long-term durability and material savings can be achieved.

A second class of fiber reinforced polymers are continuous fiber reinforced polymers (CoFRPs), which consist of a polymer matrix and aligned fibers whose length corresponds to the component dimensions. In comparison to DiCoFRP a higher strength and stiffness can be achieved due to a possible higher fiber volume content and due to the

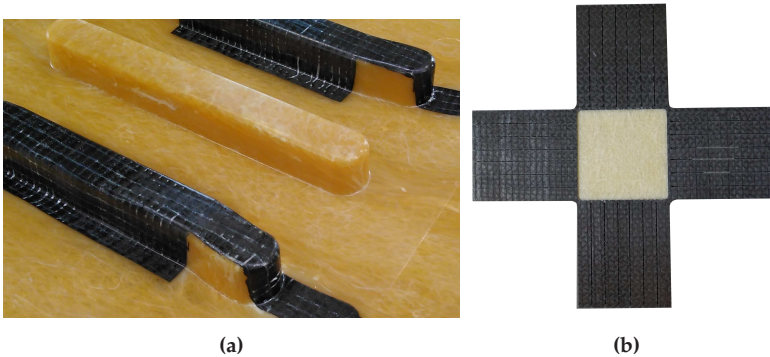


**Figure 1.1:** CoDiCoFRP applications in GRK2078. (a) Detail from reference structure made of glass DiCoFRP with carbon CoFRP reinforcements (manufactured at Fraunhofer Institute of Chemical Technology (ICT) Pfinztal), (b) Biaxial cruciform specimen made of glass DiCoFRP with carbon CoFRP reinforced arms (detailed exploitation in Section 4.5.1).

aligned fibers. The known fiber orientation allows for more straightforward modeling. Disadvantages are significantly higher production costs and effort, and a lower flexibility in shaping.

One idea is to combine these two FRP classes, DiCoFRPs and CoFRPs, in order to fusion the advantages of both. Exactly this combined material class, CoDiCoFRPs, is considered in the international research training group (IRTG) GRK2078, in which this thesis is embedded. The goal of this IRTG is an integrated engineering approach for all process steps around CoDiCoFRP parts, consisting of a discontinuous glass fiber reinforced thermoset (SMC composite) with local continuous carbon fiber reinforcements (Böhlke et al, 2019). Figure 1.1a shows a sample demonstrator part. The research training group consists of four different Research Areas: Technology, Design, Simulation, Characterization. This thesis represents the project S2 and belongs to the simulation research area, but has also a pronounced experimental part. It addresses the modeling and characterization on the macroscale with consideration of microstructure with focus on the DiCoFRP (SMC

composite). The continuous reinforcements are used for SMC composite measurements with special specimens (see Figure 1.1b).

In this framework, this work provides on the one hand a step towards a better understanding of the material composition considered in the IRTG. On the other hand the methodology, i.e. the modeling approach, the characterization methods and especially the combination of these two, can also be applied to other materials and serve as a basis for further research.

## **1.2 Research Objectives and Originality of this Thesis**

### **1.2.1 Research Objectives of this Thesis**

The overall objective is to model and to characterize the anisotropic temperature-dependent thermomechanical behavior of SMC composites on the macroscale, taking into account the microstructure. This leads to three main subjects: Firstly, the material model development, secondly a detailed experimental investigation, and thirdly, the combination of both, to identify the material parameters and to validate the model. In addition, some sub-topics are covered that are important for dealing with these main topics; especially in the field of experimental investigations.

In order to accomplish the objectives an iterative process is carried out. Starting point are the basic aspects of material modeling, i.e., the various phenomena such as elasticity, viscoelasticity, damage, etc. Considering these basic aspects, preliminary experiments are carried out to check which are the important components the material model should represent. Taking into account the preliminary tests and, of course, the thermomechanical and thermodynamically fundamentals, the material model is developed. This process leads to the final material

models and experimental setups, which are described in the present thesis. In the following, the different main subjects are described in detail.

**Material modeling.** In a first step, the linear elastic anisotropic thermo-mechanical material behavior is described by a thermodynamically consistent material model. This includes the following material constants: stiffness/compliance, thermal expansion coefficient/thermal stress coefficient, heat capacity, thermal conductivity. Two models are presented, one with constant coefficients and one with temperature-dependent coefficients. In a second step, the micromechanical structure is taken into account by microstructure tensors describing the fiber orientation distribution. The material parameters (stiffness, thermal expansion coefficient, heat capacity, thermal conductivity) are expressed linearly in terms of these fiber orientation tensors. Information about the fiber orientation tensor is taken from micro-CT data. In addition to the linear elastic material behavior, the failure behavior is considered. The failure surface is expressed linearly in terms of the fiber orientation tensors, too. This approach is combined with a Tsai-Wu failure criterion.

**Experimental investigations.** The temperature-dependent thermomechanical material parameters of the linear elastic material model are determined by experiments with various testing devices for the SMC composite and the pure resin material. Stiffness is determined via DMA measurements and via a electromechanical biaxial testing device, a dilatometer allows the measurement of the coefficient of thermal expansion and a laser flash apparatus can measure thermal diffusivity and heat capacity from which thermal conductivity can be determined. These measurements can be performed always in one direction, but by performing experiments in different directions, anisotropy can be addressed.

Damage behavior is investigated with focus on stiffness degradation

as one main phenomenon of damage. Therefore uniaxial and biaxial experiments are performed using the biaxial testing device to investigate the influence of initial anisotropy and load case on the anisotropic stiffness degradation behavior. Failure is also investigated with the biaxial testing device. Uniaxial, biaxial (and shear) tests are performed to determine the planar failure surface.

To account for microstructure, the above mentioned experiments are performed using specimens with a known averaged fiber orientation. The orientation information is provided by micro-CT scans. This establishes the connection of the thermomechanical and failure relevant material parameters with the microstructure.

As a prerequisite for the biaxial experiments, another focus lies on the development and investigation of a cruciform specimen design suitable for biaxial testing, especially with regard to the damage and failure investigations.

**Combination of modeling and experiments.** Modeling and experiments are combined in a parameter identification and an application. The parameters of the material model are determined by detailed tests that are adapted to the material model and a parameter identification procedure. As a final step, all aspects of the material model with the identified parameters are applied to reference specimens to validate the model with the identified parameters.

### 1.2.2 Originality of this Thesis

**Biaxial damage and failure investigation.** The anisotropic stiffness degradation as one main phenomenon of damage is investigated via biaxial experiments with cruciform specimens for SMC composites. Furthermore the anisotropic failure behavior is investigated. These investigations are possible due to a new *cruciform specimen design with reinforced arms*, introduced by Schemmann et al. (2018c). This

specimen design is further investigated and validated in this thesis.

**Experimental investigation of temperature-dependent thermomechanical material coefficients.** In this theses, the thermomechanical parameters stiffness, thermal expansion coefficient, heat capacity, thermal conductivity, are measured in dependence of temperature, for the pure resin material as well as for the SMC composite material. The novelty here lies on the one hand in the detailed investigation of temperature-dependent behavior of thermosets in general and in particular in the consideration of a *new material class* considered in this work, a glass fiber reinforced unsaturated polyester polyurethane hybrid resin system.

**Material model with temperature-dependent thermomechanical material coefficients.** The linear elastic thermomechanical material model is derived in a totally thermodynamically consistent way, for the variant with constant coefficients and especially for the variant with temperature-dependent coefficients.

**Assumption of linearity in fiber orientation tensor.** All directional thermomechanical coefficients as well as the failure surface are expressed linearly in terms of the fiber orientation tensor via a deviatoric and harmonic decomposition of the coefficients. This provides a relatively simple approach that directly accounts for the microstructure.

**Modeling and Experiments - holistic approach.** A particular focus of this work is the combination of modeling and experimental investigations, in such a way that both influence each other. In this approach, even the thermomechanical phenomena, which are not taken into account in the model, are considered for attention in experiments and for a comparison of the magnitudes of the different phenomena. This approach allows a deeper understanding of the overall material behavior.

## 1.3 State of the Art

Research on fiber reinforced composites, both on the experimental and on the material modeling side, has been relevant for many decades. In the following, an overview of literature on investigations on fiber reinforced composites, with a focus on SMC composites is given, structured into modeling of effective thermoelastic properties, modeling of damage and failure, experimental investigations of thermoelastic properties, and experimental investigations of damage and failure, ending here with a special focus on biaxial investigations.

**Modeling of effective thermoelastic material behavior.** Fundamentals on thermodynamic consistent material modeling, which represent a basis for modeling effective thermoelastic material behavior are elaborated, for example, in Bertram (2014) and Haupt (2002). The procedure for modeling properties of composite materials, in particular also (glass) fiber reinforced (thermoset) polymers, derived from microstructure is generally as follows. Microstructural information, especially on fiber length, geometry, orientation and volume fraction is provided either by modeling the manufacturing process, such as flow simulations as for example performed in Hohberg et al. (2017) and Meyer et al. (2020), or by experimental investigations on the finished part or specimen, mostly by micro-CT scans as described in Pinter et al. (2018) and Schöttl et al. (2021). This information can be provided in the form of a spatially resolved description of the different components, or, for orientation, in form of fiber orientation distribution functions (FODF) or fiber orientation tensors (FOT) such as introduced and described in Advani and Tucker (1987) and Kanatani (1984). Using this microstructure data, and eventually further information on the properties of the individual components of the material and interface properties, for instance, different approaches are applied to model the material behavior of the composite material. The fundamentals and key assumptions for these

approaches can be found in Torquato (2002), Mura (1987) or Nemat-Nasser and Hori (1999).

One field of approaches are full field homogenization schemes. Here, the individual phases are spatially resolved, a load is applied and the material behavior is calculated for a small (representative) volume element. The response of the small representative volume element to the applied load is used to calculate the material properties, which can then be applied to the entire component or specimen. Calculation methods are here FFT, FEM, or phase field methods. Examples where these methods have been applied for (SMC) composites are provided by Kehrer et al. (2017) and Kehrer (2019) using FFT on experimentally determined microstructure and Görthofer et al. (2020) using FFT based methods for rapid computational homogenization on generated microstructure.

Another area of approaches are mean field homogenization schemes. The basis of these methods is that the fields on the microscale are volume averaged, wherein the inhomogeneous material is smeared to an effective material (Müller, 2015; Hori and Nemat-Nasser, 1999). Mean field homogenization traces back to Voigt (1889) and Reuss (1929), providing results for effective material properties representing upper and lower bounds for a physically meaningful effective material behavior (Hill, 1952). Where these methods only account for volume fractions as micromechanical information, Hashin Shtrikman bounds (Hashin and Shtrikman, 1962) take also geometry into account. Many approaches estimating effective material behavior are based on Eshelby's solution for ellipsoidal single inclusion problem (Eshelby, 1957). For example, the simplest one is the dilute distribution method (Torquato, 2002), where no interactions between several inclusions are assumed. One frequently applied method is the Mori Tanaka homogenization scheme (Mori and Tanaka, 1973). The widespread use is due to the relatively simple derivation and implementation combined with sufficient complexity and accuracy for many applications. Numerous validations can

be found in literature. Several authors have applied such mean field methods to fiber composites, and also in particular to SMC composites, from which a few are mentioned in the following. Müller and Böhlke (2016) applied self consistent method (Kröner, 1977) and interaction direct derivative method (Zheng and Du, 2001) to calculate effective stiffness for short fiber reinforced polymers. One recent application of the Mori Tanaka homogenization scheme is given by Brylka (2017). Anagnostou et al. (2018) present a hierarchical homogenization scheme based on Mori Tanaka scheme and composite cylinders method for stiffness estimation of SMC composites. Kehrer et al. (2020) elaborated a two step Hashin-Shtrikman method for stiffness and thermal expansion calculation of SMC composites. Her investigations are combined with detailed experimental characterization, considering also temperature-dependent material behavior. In most of the above publications, fiber orientation is considered via FOTs as mentioned above.

A further approach to model the effective stiffness, also using FOTs, is given in Schemmann et al. (2018a). Here, linearity of stiffness in fiber orientation is assumed using the harmonic decomposition of the stiffness tensor (Böhlke and Brüggemann, 2001). For this approach a combination with an experimental setup and a parameter identification is performed.

**Damage and failure modeling.** Damage and failure are both occurrences that mean that a material loses its functionality due to thermomechanical impact. Failure can be described as breakage of material. Damage can be considered as the preliminary changes on the microscale in the material, that exist prior to complete failure. The final state of damage corresponds to failure. These preliminary microscopic changes may change the macroscopic properties such as stiffness. Dependent on the material, these changes of material properties can vary in magnitude and failure occurs in a more or less sudden way, accordingly. The microscopic changes of the material

leading to damage and failure vary dependent on the material class. For fiber reinforced composites there are mainly three mechanisms: matrix cracks, fiber breakage and fiber matrix interface debonding (Talreja and Singh, 2012; Gross et al., 2007). Dependent of the composite material the different mechanisms are differently pronounced. For SMC composites a number of authors has found that for many compositions the dominant mechanism is fiber matrix debonding (Fitoussi et al., 1998; Jendli et al., 2004).

The basics of damage modeling go back to Kachanov (1958) who invented the idea of a one-dimensional surface damage variable. Rabotnov (1969) used this idea and introduced the effective stress concept. The strain equivalence principle was proposed by Lemaitre (1971). These concepts allow to describe damage as stiffness degradation via a damage variable based on bearing surface reduction due to micro defects. For this damage variable an evolution law is required which can be motivated phenomenological via macroscopic quantities or micromechanically. An overview of the fundamentals on damage mechanics is given in a textbook by Lemaitre (1992).

There are various recent publications on damage modeling of fiber reinforced polymers, most of them considering stiffness degradation as main phenomenon of damage. Some models are purely phenomenological considering only macroscopic processes and quantities. Others are taking microstructural aspects into account, either in combination with phenomenological model or combined with homogenization schemes. Schulenberg et al. (2017) present a phenomenological damage model for long fiber reinforced thermoplastics using the above mentioned basic concepts. Here, anisotropic stiffness degradation is realized via stiffness degradation matrix including six instead of one damage parameters. The evolution law for the damage variables is a function of the maximum macroscopic strain. One advantage is the computationally efficiency of this damage model. An other example for an anisotropic phenomenological damage model applicable to fiber

reinforced composites is given by Mir et al. (2005). This model is based on a macroscopic approach using internal variables together with a thermodynamic potential.

A micromechanical damage model for SMC composites is presented by Fitoussi et al. (1996a). Here, the focus lies on fiber matrix interface failure, for which the basis for modeling is given in Fitoussi et al. (1996b). This work is extended by probabilistic considerations in Fitoussi et al. (1998). Desrumaux et al. (2000) further developed this modeling approaches and considered all three typical damage mechanisms: fiber breakage, matrix cracking, and interface failure. Meraghni and Benzeggagh (1995) focus on the modeling of the effect of matrix degradation on the overall behavior of randomly oriented discontinuous-fiber composites. Microcrack density as micromechanical phenomenon of damage and its effect on stiffness degradation is considered, embedded in a Mori Tanaka scheme and Eshelby's equivalent inclusion method. In the publication of Meraghni et al. (1996), the focus lies on the modeling of interfacial debonding on the overall behavior of randomly oriented discontinuous fibre composites and the effect on stiffness degradation. The damage model for SMC composites introduced by Schemmann et al. (2018b) includes isotropic matrix damage and interface debonding leading to anisotropic damage in the overall behavior. Debonding is modeled as a reduction of the load-bearing fiber fraction in the directions subjected to sufficiently large equivalent interface stresses. The model is embedded in a Mori Tanaka homogenization scheme to calculate the corresponding macroscopic material behavior.

Failure can be modeled by so called strength hypotheses which consist of a scalar failure function dependent on the different stress or strain components. Failure criteria used in literature for fiber reinforced polymers include the maximum stress failure criterion (Gandhi et al., 2020) as a simple criterion or Tsai-Wu criterion (Tsai and Wu, 1971), which captures the anisotropy of the material and the interaction of different stress components (Daniel, 2007). These failure criteria are

phenomenological and set of experiments is necessary to identify all parameters. In many publications dealing with the Tsai-Wu criterion, additional assumptions are made, such as orthotropic or transverse isotropic material symmetry. Often the interaction terms are neglected or assumptions are made about them (Van Paepegem and Degrieck (2003), Li et al. (2017)). Osswald and Osswald (2018) present a new strength tensor based failure criterion for composite materials, considering also stress interaction terms, taking the Goldenblat-Kopnov criterion (Gol'denblat and Kopnov, 1965) as basis. Colón Quintana et al. (2021) applied this criterion to SMC composites. In Schwiedrzik et al. (2013) a mathematical good and clear representation of the Tsai-Wu and other failure criteria can be found. Catapano et al. (2012) compared different failure criteria. Daniel (2007) gives an overview of failure criteria for composite materials. These failure criteria can also be used to describe failure on the microscale. Fitoussi et al. (1996b) uses a Coulomb (cf. Gross et al. (2007)) criterion to predict fiber matrix interface failure and its effect on the macroscopic material behavior. Schemmann et al. (2018b) introduce an other failure criterion to predict interfacial debonding as a basis for their damage model for SMC composites. Another way to combine microstructural processes and the phenomenological failure criteria is to establish a relationship between microstructural information and parameters of the macroscopic phenomenological failure criteria. There are very few publications on this. Tang et al. (2020) and Chen et al. (2019) present a microstructure based Tsai-Wu criterion for SMC composites in which the parameters of the strength tensors are expressed in dependence on fiber orientation tensors. Here, only the diagonal components of second order fiber orientation tensors are considered, and for the coupling terms an empirical assumption presented by Wu (1972) is made. A comparison with a micromechanical computational failure model which is validated by uniaxial tensile experiments is made. Pang et al. (1992) present a modified Tsai-Wu Ansatz where the parameters

are calculated via micromechanical assumptions and properties of the constituents.

**Experimental investigation of thermomechanical material properties.**

The thermomechanical properties of SMC composites have been extensively investigated by many authors, especially considering stiffness. However, there are only very few that cover the full range of the different material coefficients (stiffness, thermal expansion, thermal conductivity, heat capacity) capturing anisotropy and temperature dependence. In the following, an overview of publications is given, each of which deals with partial aspects of the complete temperature-dependent anisotropic thermomechanical characterization of SMC composites or similar materials. Orgéas and Dumont (2011) give an overview of thermomechanical properties. This includes average values for Young's modulus, thermal expansion coefficient, thermal conductivity, heat capacity of standard SMC in automotive applications. The given values are valid for room temperature. Additionally the dependence of stiffness on fiber volume content is investigated here. Temperature dependency of heat capacity and thermal conductivity is considered by Cecen et al. (2009). They investigated fiber polymer composites with different fiber/matrix combinations by means of heat-flux differential scanning calorimetry (DSC). Also in the investigations of Dos Santos et al. (2005) temperature dependency is considered. They use an other measuring method to determine diffusivity of polymers, the laser flash technique. In Kia (2008) thermal expansion coefficient and Young's modulus of different types of SMC composites were measured at various temperatures. The work of Trauth (2018) provides detailed results on experiments on stiffness and Poisson's ratio of the glass fiber UPPH resin SMC composite material considered also in the present work. She addresses the anisotropic material behavior by performing her measurements in different directions. The influence of the manufacturing process on the inhomogeneity of a plate is also

investigated. Specimens are taken from different regions of the manufactured plate and two different flow variations are considered. All measurements are performed at room temperature. Kehrer (2019) considered the same SMC composite material in her work. She determined storage modulus in different directions in dependence on temperature and frequency via DMA. Thermal expansion is also considered, but only at a few selected temperatures and with mentioned measuring uncertainties.

**Experimental investigation of damage and failure.** Experimental investigation of damage and failure of fiber composite material includes the investigation of the micromechanical processes as well as the changes of the macroscopic material behavior, in particular stiffness degradation.

Shirinbayan et al. (2017b) investigated the damage behavior of two SMC composites, one with high and one with randomly oriented fibers, on the macro and on the microscale. They found as predominant mechanism fiber matrix debonding. From their experiments they derived a micro and a macro damage variable. The micro damage variable is defined by the ratio of detached fibers to all fibers, and the macro damage variable is defined by the ratio of Young's modulus of the damaged material to the initial Young's modulus. Similar behavior of both damage variables was found. Fiber matrix debonding as the main damage mechanism was also found by other authors, for example by Jendli et al. (2004), and Meraghni and Benzeggagh (1995). Shirinbayan et al. (2017a) investigated an SMC composite including additionally to the fibers, spheres for weight reduction. Here, the predominant mechanism is debonding at these spheres. Remarkable is the detailed experimental setup to capture damage on the micro- and macroscale. They apply CT-scan, microscopy, ultrasonic measurement, high speed and quasi static tensile tests (uniaxial), DIC, and in situ tensile tests using scanning electronic microscopy. As macroscopic

damage mechanism stiffness degradation is considered. To consider anisotropic stiffness degradation of an SMC composite Dano et al. (2006) conduct an interesting experimental setup. They apply uniaxial damaging load on an SMC composite plate. From this damaged plate they cut specimens in different angles to measure the stiffness degradation in dependence on the direction to the load.

Failure strength is investigated by Orgéas and Dumont (2011) and Taggart et al. (1979). They considered standard SMC composites and the influence of fiber content on uniaxial failure strength. In the above mentioned work of Trauth (2018) also failure of the SMC composite investigated. Here, too, different directions and different regions of plates of two flow variants are considered in uniaxial tensile and compression experiments. Failure strength is put into relation to the stiffness. A pronounced scattering of failure strength of SMC composites is pointed out. Urapakam Ramakrishnan and Mallick (2019) considered the compression tension quadrant in their SMC composite failure experiments.

In general, there are only barely multiaxial experimental damage and failure investigations in literature, especially for SMC composites. The main reason lies in the challenge to find an appropriate cruciform specimen for biaxial experiments. Often early failure in the arms occurs before damage can be observed in the interesting center area with the biaxial stress state. Additional requirements as homogeneity of strain state, large area of interest (compared to microstructure length scales) are important (Smits et al., 2006). In Schemmann et al. (2018c) a good overview of literature on biaxial specimen design is given. Many attempts have been made to find appropriate specimens, in most publications there remain still challenges. Some promising results are provided, most with reinforced arms, by Van Hemelrijck et al. (2007) or Serna Moreno et al. (2013) for example. Hartmann et al. (2018) provide critical analysis of different biaxial specimens with regard to homogeneity of strain/stress state, parameter identifiability, and large

strains in center area. The recommendation of reinforcements is also pointed out here.

Schemmann et al. (2018c) present a cruciform specimen for an SMC composite material (same material as in the present work) with unidirectional carbon fiber reinforced arms. Good results especially in terms of large strains in the center area and homogeneity of strain state are achieved. In Lang et al. (2018) and Lang et al. (2019), this specimen design is further investigated, thereby showing the suitability for damage investigations in terms of stiffness degradation. This specimen design is used for the biaxial damage and failure investigations of this thesis and further investigated in this scope.

## 1.4 Structure of this Thesis

Chapter 2 provides fundamentals on material and mechanics. It contains information on the production and typical properties of the SMC composite as well as the CoDiCoFRP material. The continuum mechanical and micromechanical fundamentals, which are important for material modeling, are presented.

Chapter 3 presents the material models. First, the thermomechanical linear elastic model with constant and with temperature-dependent coefficients is derived. Second, the micromechanical model with the approach linear in the fiber orientations is presented. Third, the macroscopic failure modeling is explained and fourth the microstructure is here taken into account, too.

Chapter 4 deals with the experimental investigations. The testing devices are presented and the experimental procedures are described. The results of the experimental investigations on thermomechanical, damage and failure behavior are shown and discussed in detail.

Chapter 5 deals with the combination of experiments and material models and includes parameter identification and validation of material

modeling.

Chapter 6 presents an application of all the results. The material model with the identified parameters is applied to reference specimens measured with all testing devices. The results of the model and the experiments are compared.

Chapter 7 provides a summary and a conclusion.

## 1.5 Acronyms, Symbols, Notation and Operators

### 1.5.1 Symbols and Abbreviations

#### Abbreviations and acronyms

arb.	Arbitrary
CR	Charge region
CoFRP	Continuous fiber reinforced polymer
CoDiCoFRP	Continuous-discontinuous fiber reinforced polymer
CT scan	Computed tomography scan
CV	Coefficient of variation
DIC	Digital image correlation
DiCoFRP	Discontinuous fiber reinforced polymer
DIL	Dilatometer
dir.	Direction
DMA	Dynamic mechanical analysis
DMTA	Dynamic mechanical thermo analysis
exp.	Experimental
FODF	Fiber orientation distribution function
FR	Flow region
FRP	Fiber reinforced polymer
ICT	Fraunhofer Institute for Chemical Technology
iqr	Inter quartile range

IRTG	International research training group
LFA	Laser flash analysis
MFD	(Mold) flow direction
Midaco	Mixed Integer Distributed Ant Colony Optimization
mod.	Modeled
no	number
NP	Number of Parameters
perp.	Perpendicular
PR	Pure resin
RT	Room temperature
SMC	Sheet molding compound (composite)
spec.	Specimen
std	Standard deviation
sym	Symmetric
UPPH	Unsaturated polyester polyurethane hybrid
var.	Variable
1D	One dimensional
3D	Three dimensional

**Latin letters**

$a, b, A, B, \mathcal{D}, \dots$	Scalar quantities
$\mathbf{a}, \mathbf{b}, \mathbf{c}, \dots$	Vector quantities
$\mathbf{A}, \mathbf{B}, \mathbf{C}, \dots$	Second-order tensors
$\mathbb{A}, \mathbb{B}, \mathbb{C}, \dots$	Fourth order tensors
$\mathbb{A}^{<k>}$	k-th order tensors
$a$	Thermal diffusivity
$A$	Cross sectional area
$A^I$	Area of interest (center region of bone and biaxial specimens)
$c$	Heat capacity
$c_\epsilon$	Heat capacity at constant strain
$d$	Slope of stiffness degradation
$E$	Young's modulus
$E^*$	Complex elasticity modulus
$E'$	Storage modulus
$E''$	Loss modulus
$E_C$	Creep modulus
$E_R$	Relaxation modulus
$f(\epsilon)$	Biax-Uniax-stress relation factor
$f$	Biax-Uniax-stress relation factor for large stresses
$f(\mathbf{n})$	Fiber orientation distribution function
$F_i$	Force in direction $e_i$
$H$	Heaviside function
$N_c$	Number of independent constants
$N_p$	Number of symmetry planes
$t$	Time
$V$	Viscosity modulus
$g$	Temperature gradient

$n$	Direction vector
$q$	Heat conduction
$t$	Stress vector
$u$	Displacement
$x$	Current position vector
$D$	Fiber orientation tensor of second order (Kanatani 3rd kind)
$F$	Strength tensor of second order
$I$	Second order identity tensor
$G$	Deformation gradient
$H$	Displacement gradient
$N$	Fiber orientation tensor of second order (Kanatani 1st kind)
$X$	Initial position vector
$C$	Stiffness tensor
$D$	Fiber orientation tensor of fourth order (Kanatani 3rd kind)
$F$	Strength tensor of fourth order
$\mathbb{I}^S$	Fourth order identity tensor on symmetric second order tensors
$N$	Fiber orientation tensor of fourth order (Kanatani 1st kind)
$\mathbb{P}_1$	First isotropic projector ( $\mathbb{P}_1 = \frac{1}{2}\mathbf{I} \otimes \mathbf{I}$ )
$\mathbb{P}_2$	Second isotropic projector ( $\mathbb{P}_2 = \mathbb{I}^S - \mathbb{P}_1$ )
$S$	Compliance tensor
$V$	Viscosity tensor

## Greek letters

$\Gamma$	Ratio
$\Gamma_{0/90}$	Anisotropy ratio
$\tan(\delta)$	Loss modulus
$\epsilon$	Error
$\epsilon_{\text{rel}}$	Relative error
$\eta$	Entropy
$\theta$	Temperature
$\nu$	Poisson's ratio
$\xi$	Arbitrary coefficient or parameter or quantity
$\rho$	Mass density
$\psi$	Free energy
$\alpha$	Thermal expansion coefficient (tensor)
$\beta$	Thermal stress coefficient (tensor)
$\epsilon$	Infinitesimal strain tensor
$\epsilon^I$	Averaged strain in the area of interest
$\kappa$	Thermal conductivity coefficient
$\sigma$	Cauchy stress tensor
$\sigma_f$	Failure stress

## 1.5.2 Notation and Operations

In this work, direct tensor notation is preferred. As listed in Appendix 1.5.1 scalar quantities are represented in normal thin letters ( $a, A, \dots$ ), vector quantities in lower case bold letters ( $\mathbf{a}, \mathbf{b}, \dots$ ), second order tensors in upper case bold letters ( $\mathbf{A}, \mathbf{B}, \dots$ ), and fourth order tensors in double-line upper case letters ( $\mathbb{A}, \mathbb{B}, \dots$ ). Components of vectors and tensors are expressed by Latin indices, referring to the orthonormal basis  $\{\mathbf{e}_1, \mathbf{e}_2, \mathbf{e}_3\}$ . Einstein's summation convention is applied here. In the following, operations of these quantities are listed.

## Operations

$AB$	Composition of two tensors
$A \cdot B$	Scalar product of two tensors
$\mathbb{B}[A]$	Linear mapping of a second order tensor by a fourth order tensor
$A \otimes B$	Dyadic product of two tensors
$\mathbf{n}^{\otimes k}$	Higher order dyadic product: $\mathbf{n} \otimes \mathbf{n} \otimes \dots \otimes \mathbf{n}$ ( $k$ times)
$(\cdot)^T$	Transpose of a vector or second order tensor
$(\cdot)^{TM}$	Main transpose of a fourth order tensor ( $C_{ijkl}^{TM} = C_{klji}$ )
$(\cdot)^{TL}$	Left minor transpose of a fourth order tensor ( $C_{ijkl}^{TM} = C_{klji}$ )
$(\cdot)^{TR}$	Right minor transpose of a fourth order tensor ( $C_{ijkl}^{TM} = C_{lkij}$ )
$\text{sym}(\cdot)$	Symmetric part of a quantity
$\text{symF}(\cdot)$	Full symmetrization, i.e. invariance with regard to all permutations of all indices
$(\cdot)^\circ$	Spherical part of a second order tensor ( $\varepsilon^\circ = \mathbb{P}_1[\varepsilon] = \frac{1}{3}\text{tr}(\varepsilon)\mathbf{I}$ )
$(\cdot)'$	Deviatoric part of a second order tensor ( $\varepsilon' = \mathbb{P}_2[\varepsilon] = \varepsilon - \frac{1}{3}\text{tr}(\varepsilon)\mathbf{I}$ )
$\text{div}(\cdot)$	Divergence of a quantity
$\text{grad}(\cdot)$	Gradient of a quantity
$(\dot{\cdot})$	Material time derivative
$\nabla$	Nabla operator
$ (\cdot) $	Absolute value of a quantity



## Chapter 2

# Fundamentals

## 2.1 Materials

### 2.1.1 Discontinuous Glass Fiber Reinforced SMC Composites

**Composition and typical properties.** As DiCoFRP, Sheet Molding Compound (SMC) composites are considered here, consisting of a thermosetting matrix and glass fibers and often additives and fillers. The properties of SMC composites result from the properties of the individual constituents and the interface properties. In the following the basic properties of the main components (thermosetting polymers and glass) and the general properties of the composite material are described.

Thermosetting polymers consist of macromolecules which are highly crosslinked by chemical primary valency bonds. They are not meltable after curing. The density of thermosetting polymers ranges from  $0.9 \text{ g/cm}^3$  up to  $1.5 \text{ g/cm}^3$ . Thermosets show a high chemicals and corrosion resistance. The temperature resistance can reach values of up to  $300^\circ\text{C}$ . The strength is around  $70 \text{ MPa}$  and the Young's modulus (storage modulus) around  $3000 \text{ MPa}$  (Neitzel and Mitschang, 2004). Typical values for the thermal conductivity are  $0.2 \text{ W/(mK)}$ , for the thermal expansion coefficient  $20 \cdot 10^{-6} \text{ 1/K}$  and for the specific heat

capacity 1.2 J/(gK). These values are taken from Ribeiro et al. (2003), Shimamura et al. (2020) and own measurements.

Glass fibers show a high strength based on the covalent bond between oxygen and silicon, which can reach values of up to 4500 MPa. The Young's modulus lies at 70000 MPa to 90000 MPa. The density of glass is around 2.5 g/mm<sup>2</sup>. SMC composites can contain fillers, as limestone, for economical reasons and additives, like color pigments, to modify the mechanical, thermal or optical properties.

The properties of SMC composites depend strongly on the composition and the manufacturing process. Also the combination of the individual components play a role, because the interface properties of fiber and matrix varies. Fiber volume content, which can have values of up to 40 vol%, and fiber shape and length have an influence on the properties. Typically, the fibers in SMC composites have a length of 10 mm up to 30 mm. Some general property ranges are given in the following. SMC composites have a strength of 80 MPa up to 250 MPa, a temperature resistance according to the temperature resistance of the polymer, a density of about 1.2 g/cm<sup>3</sup> to 2.2 g/cm<sup>3</sup>, a relatively brittle fracture behavior and a Young's modulus of 5000 MPa to 15000 MPa. Values for the thermal conductivity lie around 0.25 W/(mK), for the thermal expansion coefficient at  $15 \cdot 10^{-6}$  1/K and for the specific heat capacity at 1 J/(gK). These values are taken from Lang (2013), Oldenbo et al. (2003), and Trauth (2018), and from own measurements.

**Manufacturing process.** The manufacturing of SMC consists of many different steps, starting with the preparation of the pure materials and ending with post processing steps. Two sub steps are considered here in detail, the manufacturing of the semi finished molding compound and the hotpressing process. These steps influence mainly the thermo-mechanical properties.

The semi finished, flowable, flat molding compound is produced as shown in Figure 2.1. The matrix (mixture of resin, curing agent and

additives) is applied on a carrier film (release film). The chopped glass fibers (cut from fiber rovings by a cutter) trickle onto the resin film. The fiber content is controlled by the conveyor speed. Covered with a second carrier film, fibers and resin are rolled and thus mixed and compacted by multiple rollers in an impregnation belt. For thickening the few millimeters thick and up to 1.5 m wide SMC stripes are rolled up and stored for several days. This whole process induces a heterogeneous and randomly oriented fiber distribution in the semi finished product.

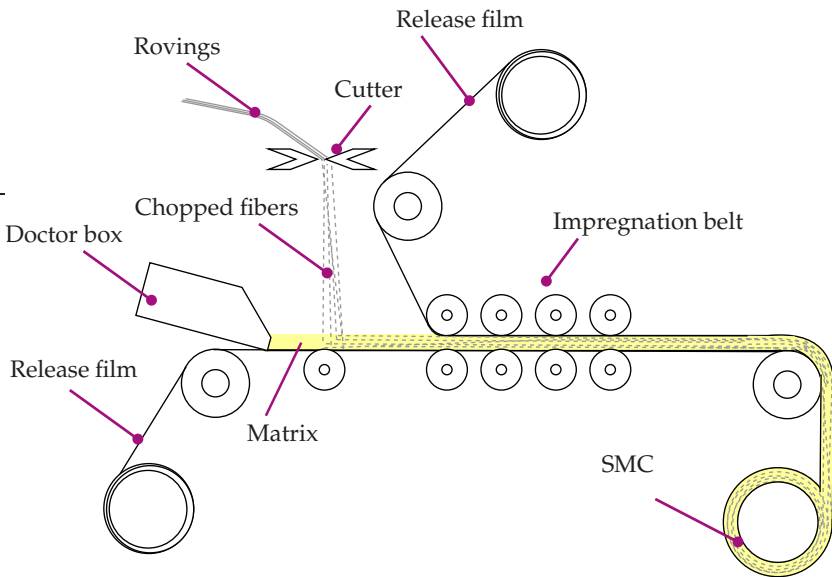


**Figure 2.1:** Manufacturing of the semi-finished SMC material.

To manufacture the plates or the parts of the finished composite material, the semi finished product is cut into pieces (see Figure 2.2) and placed into a heated mold and pressed by steel tools. The thickness

of the plate or the part can be varied by changing the amount of SMC, i.e. the number of cut SMC pieces, placed in the mold. Figure 2.3 shows the hotpressing process schematically.

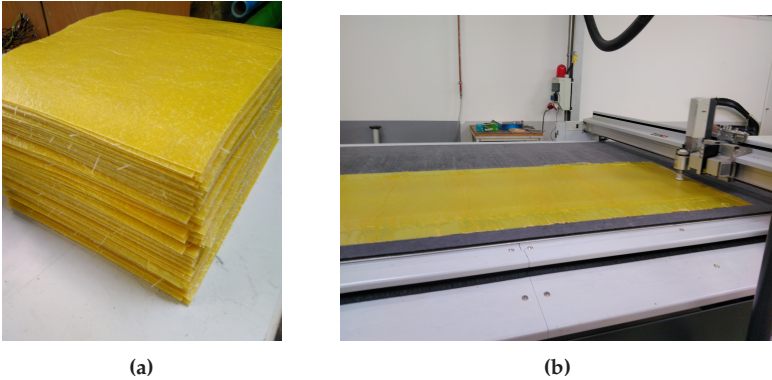


**Figure 2.2:** Semi finished SMC. (a) SMC pieces (250 mm x 300 mm) for placement in mold for hotpressing, (b) SMC cutting machine at Fraunhofer Institute of Chemical Technology (ICT) Pfinztal.

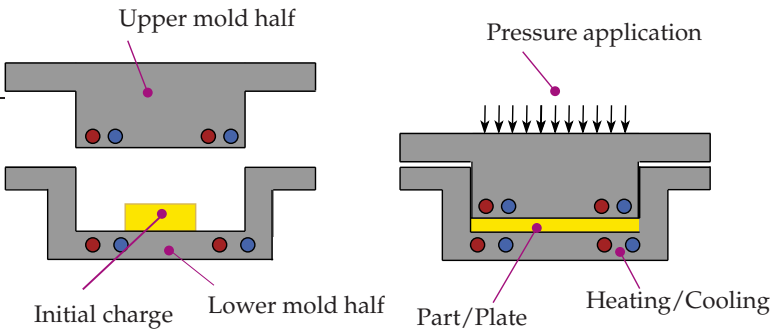


**Figure 2.3:** Hotpressing of the SMC composite part or plate.

Due to heat and pressure the material flows and fills the mold and the polymerisation is initiated and leads to the solidification of the material. The mold filling process can induce or reinforce the already existing anisotropies and heterogeneities. By changing the mold coverage and placement, the anisotropy can be deliberately varied.

### **2.1.2 Continuous Carbon Fiber Reinforced SMC Composites**

The CoFRPs considered here consist of a thermosetting polymer, too, as matrix and long (endless) carbon fibers. The properties of the composite material can reach values of about 120 GPa for the Young's modulus and 1700 GPa for the tensile strength in the direction tangential to the fiber alignment (Trauth, 2018).

The process to manufacture the semi finished CoFRPs material, that can be used for CoDiCoFRPs, is in principle similar to the one of DiCoFRPs, but with endless fibers instead of the chopped fibers. Before comolding, an intermediate step can be performed due to a particular characteristic of the resin system. The resin system can be cured in two-step process which provides a chemically stable and highly viscous B-stage ideal for cutting, preforming and handling of the prepregs prior to the comolding process (Bücheler, 2017).

### **2.1.3 Continuous-Discontinuous Fiber Reinforced SMC Composites**

The comolding process leading to the CoDiCoFRP material can be performed for DiCoFRP parts with local CoFRP reinforcements of complex shapes and for DiCoFRP plates fully reinforced with CoFRP layers. In each case, the CoFRP is cut and formed into the final

geometry using the stable B-stage. Specific layer structures consisting of more than one layer can be realized by stacking by the cut CoFRPs accordingly. The CoFRP prepregs are inserted into the mold at the appropriate location prior to hot pressing. Using mechanisms such as geometric form closure, the prepreg remains in the appropriate position. To manufacture a whole reinforced plate (as used in this work), one layer of the reinforcing CoFRP prepreg is placed filling the whole mold. On top of this, the SMC (semi-finished DiCoFRP) is placed in the desired mold coverage. A second layer of CoFRP is applied on top, which stays in shape due to the stiff prepreg and the supporting effect of the mold wall. When the press closes, only the SMC flows and the CoFRP prepregs maintain their shape. Details on the manufacturing process can be found in Bücheler (2017).

#### 2.1.4 Materials used in this Thesis

The SMC material which is mainly investigated in this work was manufactured at Fraunhofer Institute for Chemical Technology (ICT, Pfinztal). The resin system consists of a unsaturated polyester polyurethane hybrid resin (UPPH) without any fillers. The composition is listed in Table 2.1.

Component	Trade name	Weight fraction
UPPH resin	Daron ZW 14142	77 %
Adherent and flow aids	BYK 9085	1.5 %
Impregnation aid	BYK 9076	2.3 %
Deaeration aid	BYK A-530	0.38 %
Inhibitor	pBQ	0.0023 %
Peroxide	Trigonox 117	0.77 %
Isocyanate	Lupranat M20R	18 %

**Table 2.1:** Composition of the UPPH resin (Hohberg et al., 2017).

The fibers are made of e-glass and have a length of 25.4 mm. The fiber volume content is 42 wt% corresponding to 23 vol%.

The manufactured plates have a rectangular shape with a length of 800 mm and a width of 250 mm. The thickness varies around about 2 mm dependent on the plate. Two different mold coverages are realized and used in this work:

- Mold coverage of 40 % in the middle of the mold, with a long flow path and induced orientation of the fibers in length direction (in the following designated as "flow")
- Mold coverage of 100 % with no flow path and almost randomly orientation of the fibers in the plane (in the following designated as "full")

Figures 2.4 and 2.5 depict schematically the two variants. As designated by the arrows,  $0^\circ$ -direction corresponds always to the longitudinal direction (flow direction for the flow plates) and  $90^\circ$ -direction corresponds to the perpendicular direction in the plate plane. The direction perpendicular to the  $0^\circ$ - $90^\circ$  plate plane ("plate thickness direction") is designated by the suffix "perp." throughout this thesis.

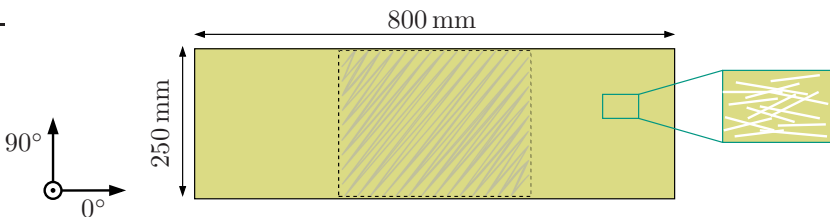


**Figure 2.4:** Rectangular SMC composite plates ("flow") of this work with mold coverage of 40 %; grey hatched area corresponds to the charge region (initial mold coverage). Detail framed in turquoise schematically shows the fiber orientation.

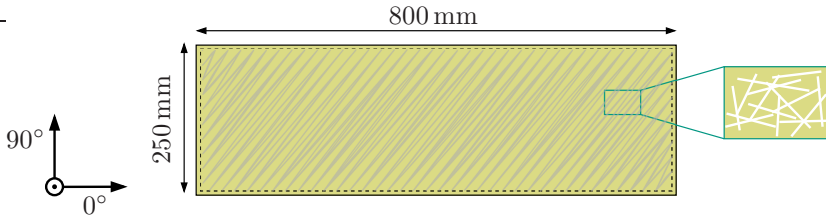


**Figure 2.5:** Rectangular SMC composite plates ("full") of this work with mold coverage of 100%; grey hatched area corresponds to the charge region (initial mold coverage). Detail framed in turquoise schematically shows the fiber orientation.

Additional to the pure glass SMC composite plates, continuous carbon fiber reinforced plates with the same geometry are considered. The reinforcements are on both sides in  $0^\circ$ - $90^\circ$ -layers to the length direction of the plate (see Figure 2.4). Figure 2.6 depicts schematically the layers in a cross sectional view.

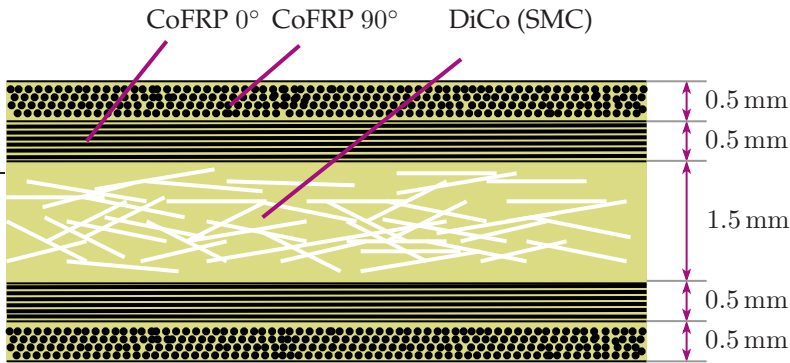


**Figure 2.6:** Schematic cross sectional view (detail) of the continuous fiber reinforced plate of the CoDiCo plate; the dimensions vary and represent here only an order of magnitude.

The specifications regarding the different mold coverages are the same as for the pure SMC. This material is not studied itself, but is used as an auxiliary material in the reinforcement of the special biaxial specimens

(see Section 4.5.1).

In addition to the reinforced material, also plates made from the pure resin material are considered. They are produced in a similar manufacturing process as the reinforced SMC plates. Some adaptations are necessary due to the differences in the material behavior during the manufacturing process.

## 2.2 Continuum Mechanics

### 2.2.1 Kinematics

The continuum mechanical fundamentals described in the following sections are treated in detail in textbooks, for example in Haupt (2002), Bertram (2014), Müller (2011), Truesdell and Toupin (1960). According to the definition in continuum mechanics, a body consists of a set of material points. Considering the body as boltzmann-continuum, the material points have three translational and no rotational degrees of freedom. The subject of kinematics is the description of the movement of such a body. During the movement the placement of the body changes, that means the volume and shape that the material points adopt change. The placement at the initial time  $t = t_0$  is the reference placement, the placement at the current moment ( $t > t_0$ ) is the current placement. The position of a material point in the reference placement of the body is given by the initial position vector  $\mathbf{X}$  and current placement of the body is given by its position vector  $\mathbf{x}$ . The current position can be described by the function

$$\mathbf{x} = \chi(\mathbf{X}, t). \tag{2.1}$$

The displacement of a material point  $\mathbf{u}(\mathbf{X}, t)$  is the difference between its initial and its current position

$$\mathbf{u}(\mathbf{X}, t) = \mathbf{x} - \mathbf{X}. \quad (2.2)$$

Figure 2.7 illustrates the movement of a body and the different vectors for a selected material point  $P$ .

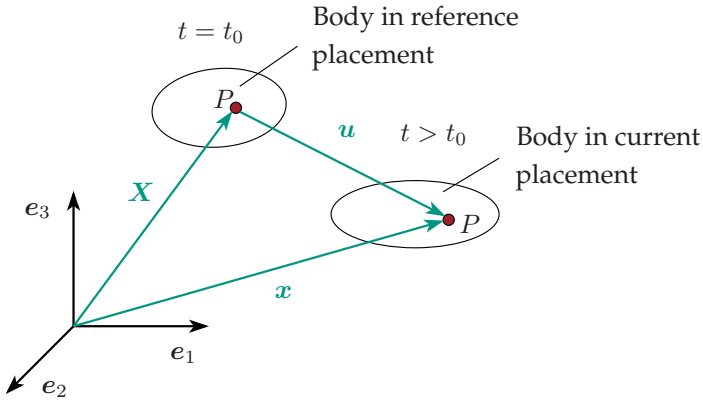


Figure 2.7: Movement of a body.

The velocity is given by the material time derivative of the current position

$$\mathbf{v}(\mathbf{X}, t) = \dot{\mathbf{x}} = \frac{\partial \chi(\mathbf{X}, t)}{\partial t}. \quad (2.3)$$

The deformation gradient  $\mathbf{G}$  is the partial derivative of  $\chi$  with respect to  $\mathbf{X}$ :

$$\mathbf{G} = \frac{\partial \chi(\mathbf{X}, t)}{\partial \mathbf{X}}. \quad (2.4)$$

The displacement gradient is defined analogously

$$\mathbf{H} = \frac{\partial \mathbf{u}(\mathbf{X}, t)}{\partial \mathbf{X}} = \mathbf{F} - \mathbf{I}. \quad (2.5)$$

In the case of small deformations ( $\|\mathbf{H}\| \ll 1$ ) a geometrically linear theory is valid. In this case the infinitesimal strain tensor describes the deformation state

$$\boldsymbol{\varepsilon} = \frac{1}{2} \left( \frac{\partial \mathbf{u}}{\partial \mathbf{x}} + \left( \frac{\partial \mathbf{u}}{\partial \mathbf{x}} \right)^T \right) = \begin{pmatrix} \varepsilon_{11} & \varepsilon_{12} & \varepsilon_{13} \\ \varepsilon_{21} & \varepsilon_{22} & \varepsilon_{23} \\ \varepsilon_{31} & \varepsilon_{32} & \varepsilon_{33} \end{pmatrix} \mathbf{e}_i \otimes \mathbf{e}_j. \quad (2.6)$$

The strain tensor can be decomposed into a spherical  $\boldsymbol{\varepsilon}^\circ$  and a deviatoric  $\boldsymbol{\varepsilon}'$  part

$$\boldsymbol{\varepsilon} = \boldsymbol{\varepsilon}^\circ + \boldsymbol{\varepsilon}'. \quad (2.7)$$

These parts can be calculated using the two isotropic projectors

$$\boldsymbol{\varepsilon}^\circ = \mathbb{P}_1[\boldsymbol{\varepsilon}] = \frac{1}{3} \text{tr}(\boldsymbol{\varepsilon}) \mathbf{I}, \quad \boldsymbol{\varepsilon}' = \mathbb{P}_2[\boldsymbol{\varepsilon}] = \boldsymbol{\varepsilon} - \frac{1}{3} \text{tr}(\boldsymbol{\varepsilon}) \mathbf{I}. \quad (2.8)$$

The spherical part describes the volume change and the deviatoric part describes the shape change.

## 2.2.2 Balance Equations

**General formulation.** Balance equations represent the change of an additive quantity in a limited volume in form of an equation. (It is not required that the quantity is a conserved quantity, balance equations are kind of an extension to conservation laws.) A field quantity in a volume  $V(t)$  can change by the production  $p_\varphi$  and the supply  $s_\varphi$  in the volume and by the flux  $\mathbf{q}_\varphi$  over the boundary of the volume  $\partial V(t)$ . So the general integral formulation of the balance equation for a field quantity  $\varphi(\mathbf{x}, t)$  reads

$$\frac{d}{dt} \int_{V(t)} \varphi \, dV = \int_{V(t)} p_\varphi + s_\varphi \, dV + \int_{\partial V(t)} \mathbf{q}_\varphi \cdot d\mathbf{A} \quad (2.9)$$

with  $d\mathbf{A} = \mathbf{n} dA$ , where  $dA$  is the surface element and  $\mathbf{n}$  is the outer normal unit vector of the boundary of the volume  $\partial V(t)$ .

The application of the divergence theorem and the Reynolds transport theorem leads to the local formulation of the balance equation in regular points

$$\frac{\partial \varphi}{\partial t} + \operatorname{div}(\varphi \mathbf{v}) = p_\varphi + s_\varphi + \operatorname{div}(\mathbf{q}_\varphi). \quad (2.10)$$

These are regular points when the field quantity is continuous and differentiable there.

For conserved quantities the production is zero. The general form of a balance equation of tensorial quantities is analogous to the scalar form. In continuum mechanics there are five important balance equations, these are the balance of mass, the balance of linear and angular momentum and the energy and entropy balance. In the following these balance equations are considered in the local formulation in regular points.

**Balance of mass.** Considering the mass density  $\varrho$  as field quantity leads to the balance of mass. As the production (mass is a conserved quantity), supply, and the flux are zero the local formulation of the mass balance is

$$\dot{\varrho} + \varrho \operatorname{div}(\mathbf{v}) = 0. \quad (2.11)$$

With  $\varrho(t) = \varrho_0(1 - \operatorname{tr}(\boldsymbol{\varepsilon}(t)))$  the mass density can be considered as approximately constant for small deformations.

**Balance of linear and angular momentum.** First, the stress tensor  $\boldsymbol{\sigma}$  is introduced because of its use in balance of linear and angular momentum. The stress vector  $\mathbf{t}$  at point  $P$  of a cut is defined as

$$\mathbf{t} = \lim_{\Delta A \rightarrow 0} \frac{\Delta \mathbf{f}}{\Delta A} = \frac{d\mathbf{f}}{dA}, \quad (2.12)$$

where  $\Delta \mathbf{f}$  is the force acting on the area  $A$ .

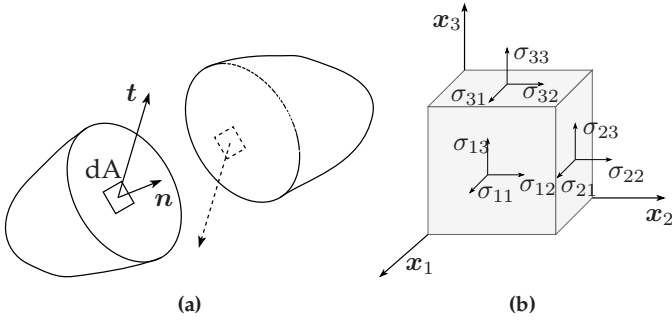


Figure 2.8: Stress vector (according to Gross and Seelig (2007)).

The stress vector  $\mathbf{t}$  depends on the orientation of the cut through  $P$  which is characterized by the normal unit vector  $\mathbf{n}$  (see Figure 2.8a). The stress tensor  $\boldsymbol{\sigma}$  is defined by three stress vectors which are perpendicular to each other. If the cutting plane is chosen perpendicular to the axes of orthonormal coordinate system, the components of the stress tensor can be represented in the form of the Cauchy stress tensor

$$\boldsymbol{\sigma} = \begin{pmatrix} \sigma_{11} & \sigma_{12} & \sigma_{13} \\ \sigma_{21} & \sigma_{22} & \sigma_{23} \\ \sigma_{31} & \sigma_{32} & \sigma_{33} \end{pmatrix} \mathbf{e}_i \otimes \mathbf{e}_j, \quad (2.13)$$

where  $\mathbf{e}_i$  and  $\mathbf{e}_j$  with  $i = 1, 2, 3$  are the unit vectors of the orthonormal base. The left index denotes the cutting plane (direction of the normal) and the right denotes the direction of the stress. The diagonal components are the normal stress components and the non-diagonal components are the shear stress components (see Figure 2.8b).

The stress tensor  $\boldsymbol{\sigma}$  can be decomposed in the same way as the strain tensor  $\boldsymbol{\varepsilon}$  (see Equation (2.7), Equation (2.8)).

The relation between stress tensor and stress vector is given by the Cauchy Lemma

$$\mathbf{t} = \boldsymbol{\sigma} \mathbf{n}. \quad (2.14)$$

In the linear momentum balance, the balanced field quantity is the momentum density  $\rho \mathbf{v}$ , a first order tensor. The production is zero, the supply is  $\rho \mathbf{b}$ , and the flux is the stress  $\boldsymbol{\sigma}$ . The local formulation of the balance of linear momentum under consideration of the mass balance (Equation (2.11)) yields the following

$$\rho \dot{\mathbf{v}} = \rho \mathbf{b} + \operatorname{div}(\boldsymbol{\sigma}). \quad (2.15)$$

with  $\dot{\mathbf{v}}$  being the second local time derivative of  $\mathbf{x}$ . For the quasi static case without any volume forces the balance of linear momentum simplifies to

$$\operatorname{div}(\boldsymbol{\sigma}) = 0. \quad (2.16)$$

In a Boltzmann continuum, the balance of angular momentum leads to

$$\boldsymbol{\sigma} = \boldsymbol{\sigma}^\top. \quad (2.17)$$

**Balance of energy and entropy.** The balance of mechanical energy is obtained by multiplying the balance of linear momentum by the velocity  $\mathbf{v}$

$$\frac{1}{2} \rho (\mathbf{v} \cdot \mathbf{v})' = \rho \mathbf{b} \cdot \mathbf{v} + \operatorname{div}(\boldsymbol{\sigma}^\top \mathbf{v}) - \boldsymbol{\sigma} \cdot \dot{\boldsymbol{\epsilon}}. \quad (2.18)$$

The flux is the power of external forces  $\operatorname{div}(\boldsymbol{\sigma} \mathbf{v}) = \operatorname{div}(\boldsymbol{\sigma}^\top \mathbf{v})$  (see Equation (2.17)),  $\rho \mathbf{b} \cdot \mathbf{v}$  is the supply of kinetic energy and the production is the stress power  $-\boldsymbol{\sigma} \cdot \dot{\boldsymbol{\epsilon}}$ .

The total energy is the sum of the kinetic energy  $\frac{1}{2} \rho (\mathbf{v} \cdot \mathbf{v})'$  and the inner energy  $\rho e$

$$\rho \dot{e} + \frac{1}{2} \rho (\mathbf{v} \cdot \mathbf{v})' = \rho \omega - \operatorname{div}(\mathbf{q}) + \rho \mathbf{b} \cdot \mathbf{v} + \operatorname{div}(\boldsymbol{\sigma} \mathbf{v}). \quad (2.19)$$

The vector  $\mathbf{q}$  is the heat flux vector giving with  $\boldsymbol{\sigma} \mathbf{v}$  the flux and  $\omega$  is the heat supply giving with  $\rho \omega + \rho \mathbf{b} \cdot \mathbf{v}$  the supply term. The total energy is a conserved quantity, the production is zero.

Subtracting the kinetic energy from the total energy gives the balance of the internal energy

$$\rho \dot{e} = \rho \omega - \operatorname{div}(\mathbf{q}) + \boldsymbol{\sigma} \cdot \dot{\boldsymbol{\varepsilon}}. \quad (2.20)$$

The internal energy contains only energy parts that are independent of a observer. It consists of the kinetic energy of the atomic movements, the potential energy of the intermolecular forces, the binding energy between molecules and nuclear energy.

For the entropy balance the balanced quantity is the volume specific entropy  $\psi = \rho \eta$ . The local form of the entropy balance reads

$$\rho \dot{\eta} = \frac{1}{\theta} \rho \omega - \operatorname{div}\left(\frac{\mathbf{q}}{\theta}\right) + \rho p_{\eta}. \quad (2.21)$$

Here,  $\rho \omega / \theta$  is the supply of entropy,  $\mathbf{q} / \theta$  is the flux and  $p_{\eta}$  is the production of entropy. The entropy is not a conserved quantity, so the production is in general not zero. The second law of thermodynamics states that the entropy production is non-negative

$$\eta \geq 0. \quad (2.22)$$

### 2.2.3 Material Theory

**Material functions.** The description of relations of movement, temperature and stress state for a body can be considered as one main goal of continuum mechanics. For this purpose, the balance equations serve as a basis, as they have to be valid universally. Assuming the volume forces  $\mathbf{b} = \mathbf{b}_0$  and the heat source  $\omega = \omega_0$  as constant and given, the quantities stress  $\boldsymbol{\sigma}$ , internal energy  $e$  and heat flux vector  $\mathbf{q}$  and entropy  $\eta$  remain in the balance equations, which have to be set into relation to the displacement and temperature field. These relations are the material functions. There are principles and restrictions for

the formulation of material functions, from which two crucial ones are shortly presented in the following: the objectivity and shape invariance, leading to the principle of invariance under superimposed rigid body motions (PISM); and the second law of thermodynamics.

**PISM.** The application of the PISM simplifies the material functions to be determined for thermoelastic solids from

$$\xi = \xi(\nabla \mathbf{u}, \mathbf{u}, \nabla \theta, \theta) \quad (2.23)$$

to

$$\xi = \xi(\boldsymbol{\varepsilon}, \theta, \mathbf{g}) \quad (2.24)$$

for a quantity  $a$  with the strain  $\boldsymbol{\varepsilon} = \nabla^S \mathbf{u}$  and the temperature gradient  $\mathbf{g}$ . This leads to the the following materials functions that are to be determined

$$\begin{aligned} \boldsymbol{\sigma} &= \boldsymbol{\sigma}(\boldsymbol{\varepsilon}, \theta, \mathbf{g}), \\ e &= e(\boldsymbol{\varepsilon}, \theta, \mathbf{g}), \\ \mathbf{q} &= \mathbf{q}(\boldsymbol{\varepsilon}, \theta, \mathbf{g}), \\ \eta &= \eta(\boldsymbol{\varepsilon}, \theta, \mathbf{g}). \end{aligned} \quad (2.25)$$

The stress  $\boldsymbol{\sigma}$  can be decomposed additively in a equilibrium part  $\boldsymbol{\sigma}^{\text{eq}}$  and a non-equilibrium part  $\boldsymbol{\sigma}^{\text{neq}}$ . The equilibrium part is the energetic part that is zero when strain rate and temperature gradient are zero and the non-equilibrium part is the dissipative part. Considering thermoelastic solids, the non-equilibrium stress is zero. Thus, there are only equilibrium stresses:

$$\boldsymbol{\sigma}^{\text{neq}} = \mathbf{0}, \quad \boldsymbol{\sigma} = \boldsymbol{\sigma}^{\text{eq}}. \quad (2.26)$$

**Dissipation inequality (Clausius-Duhem inequality).** The second law of thermodynamics is considered in form of the Dissipation Inequality

(Clausius-Duhem inequality)

$$\frac{1}{\rho} \boldsymbol{\sigma} \cdot \dot{\boldsymbol{\varepsilon}} - \dot{\psi} - \eta \dot{\theta} - \frac{1}{\rho \theta} \mathbf{q} \cdot \mathbf{g} \geq 0. \quad (2.27)$$

This equation is obtained by replacing the the heat supply  $\omega$  using the balance of internal energy (see Equation (2.20)) and by using the free Helmholtz energy

$$\psi = e - \eta \theta. \quad (2.28)$$

Inserting the material time derivative of the free Helmholtz energy

$$\dot{\psi}(\boldsymbol{\varepsilon}, \theta, \mathbf{g}) = \frac{\partial \psi}{\partial \boldsymbol{\varepsilon}} \cdot \dot{\boldsymbol{\varepsilon}} + \frac{\partial \psi}{\partial \theta} \dot{\theta} + \frac{\partial \psi}{\partial \mathbf{g}} \cdot \dot{\mathbf{g}}. \quad (2.29)$$

into Equation (2.27) leads to the following form of the dissipation inequality

$$\left( \frac{\boldsymbol{\sigma}}{\rho} - \frac{\partial \psi}{\partial \boldsymbol{\varepsilon}} \right) \cdot \dot{\boldsymbol{\varepsilon}} - \left( \eta + \frac{\partial \psi}{\partial \theta} \right) \dot{\theta} - \frac{\partial \psi}{\partial \mathbf{g}} \cdot \dot{\mathbf{g}} - \frac{1}{\rho \theta} \mathbf{q} \cdot \mathbf{g} \geq 0. \quad (2.30)$$

Due to linearity of this inequality in  $\dot{\boldsymbol{\varepsilon}}$ ,  $\dot{\theta}$ ,  $\dot{\mathbf{g}}$  and to arbitrariness of these, the following potential relations can be derived

$$\frac{\boldsymbol{\sigma}}{\rho} = \frac{\partial \psi}{\partial \boldsymbol{\varepsilon}}, \quad (2.31)$$

$$\eta = - \frac{\partial \psi}{\partial \theta}, \quad (2.32)$$

$$\frac{\partial \psi}{\partial \mathbf{g}} = \mathbf{0}. \quad (2.33)$$

It remains the reduced dissipation inequality

$$- \mathbf{q} \cdot \mathbf{g} \geq 0. \quad (2.34)$$

The free energy can not depend on the temperature gradient. This procedure to find these potential relations is called Coleman Noll procedure and can be found in Coleman and Noll (1963).

**Heat equation.** Further thermodynamical considerations, calculations and transformations are helpful for useful equations containing the quantities for which relations are sought. For example the heat equation is obtained by combining the balance of the internal energy (Equation (2.20)) with the free Helmholtz energy (Equation (2.28)) and the potential relations (Equations (2.31) and (2.32)). The entropy rate is obtained by inserting the potential relations in the free energy rate

$$\dot{\eta} = -\frac{\partial^2 \psi}{\partial \boldsymbol{\varepsilon} \partial \theta} \cdot \dot{\boldsymbol{\varepsilon}} - \frac{\partial^2 \psi}{\partial \theta^2} \dot{\theta}. \quad (2.35)$$

Inserting the potential relations (Equations (2.31) and (2.32)) and the free energy (Equation (2.28)) into the balance of internal energy (Equation (2.20)) gives

$$\rho \theta \dot{\eta} = \rho \omega - \operatorname{div}(\mathbf{q}). \quad (2.36)$$

Equation (2.35) and Equation (2.36) lead to the heat equation

$$\rho \dot{\theta} \frac{\partial^2 \psi}{\partial \theta^2} \cdot \theta = \rho \omega - \operatorname{div}(\mathbf{q}) + \rho \theta \frac{\partial^2 \psi}{\partial \boldsymbol{\varepsilon} \partial \theta} \cdot \dot{\boldsymbol{\varepsilon}}. \quad (2.37)$$

**Definition/Representations of material coefficients.** It is useful to define and consider material coefficients in order to express relations between the quantities (temperature, stress, strain, for instance). For these coefficients, assumptions (as constant, or linear in temperature, for instance) can be made to define a material model. Considering for example the heat equation (Equation (2.37)) the definition of the specific heat capacity at constant strains

$$c_{\boldsymbol{\varepsilon}} = -\theta \frac{\partial^2 \psi(\boldsymbol{\varepsilon}, \theta)}{\partial \theta^2} \quad (2.38)$$

and the definition of the thermal stress coefficient

$$\beta = -\varrho \frac{\partial \psi(\boldsymbol{\varepsilon}, \theta)}{\partial \boldsymbol{\varepsilon} \partial \theta} = \frac{\partial \boldsymbol{\sigma}}{\partial \theta} \Big|_{\boldsymbol{\varepsilon}} \quad (2.39)$$

is useful. Using these definitions the heat equation reads

$$\varrho \dot{\theta} c_{\varepsilon} = \varrho \omega - \operatorname{div}(\mathbf{q}) - \theta \beta \cdot \dot{\boldsymbol{\varepsilon}}. \quad (2.40)$$

Analogously to the thermal stress coefficient, describing the change of the stress due to a temperature change at constant strains, the thermal expansion coefficient can be defined as

$$\alpha = \frac{\partial \boldsymbol{\varepsilon}}{\partial \theta} \Big|_{\boldsymbol{\sigma}} \quad (2.41)$$

describing the change of the strain due to a temperature change at constant stress.

A further important coefficient is the stiffness tensor as in the sense of the classical Hooke's law

$$\mathbb{C} = \frac{\partial \boldsymbol{\sigma}}{\partial \boldsymbol{\varepsilon}} = \varrho \frac{\partial^2 \psi}{\partial \boldsymbol{\varepsilon}^2}. \quad (2.42)$$

The compliance tensor is defined as

$$\mathbb{S} = \mathbb{C}^{-1} = \frac{\partial \boldsymbol{\varepsilon}}{\partial \boldsymbol{\sigma}}. \quad (2.43)$$

The stiffness and the thermal stress coefficients can be used to describe material models in stress explicit form and the compliance and the thermal expansion coefficients to describe material models in strain explicit form.

**Material symmetries.** The stiffness tensor  $\mathbb{C}$  in the sense of classical Hooke's law,  $\boldsymbol{\sigma} = \mathbb{C}[\boldsymbol{\varepsilon}]$ , has the major symmetry ( $C_{ijkl} = C_{klij}$ ) and the

two minor symmetries ( $C_{ijkl} = C_{jikl} = C_{ijlk}$ ):

$$\mathbb{C} = \mathbb{C}^{\text{TH}} = \mathbb{C}^{\text{TL}} = \mathbb{C}^{\text{TR}}. \quad (2.44)$$

To represent anisotropic symmetry classes, the normalized Voigt notation is first introduced. Here, the stress and strain tensors are taken as first order tensors and the stiffness and compliance tensors as second order tensors in a six-dimensional space. Therefore, a orthonormal base  $\mathbf{B}(\alpha, \beta = 1..6)$  is introduced. It applies then

$$\mathbf{B}_\alpha \cdot \mathbf{B}_\beta = \delta_{\alpha\beta}. \quad (2.45)$$

With respect to any orthonormal basis system in  $\mathbb{R}^3$ , the basis tensors can be represented as follows

$$\mathbf{B}_1 = \mathbf{e}_1 \otimes \mathbf{e}_1 \quad \mathbf{B}_4 = \frac{\sqrt{2}}{2}(\mathbf{e}_2 \otimes \mathbf{e}_3 + \mathbf{e}_3 \otimes \mathbf{e}_2) \quad (2.46)$$

$$\mathbf{B}_2 = \mathbf{e}_2 \otimes \mathbf{e}_2 \quad \mathbf{B}_5 = \frac{\sqrt{2}}{2}(\mathbf{e}_1 \otimes \mathbf{e}_3 + \mathbf{e}_3 \otimes \mathbf{e}_1) \quad (2.47)$$

$$\mathbf{B}_3 = \mathbf{e}_3 \otimes \mathbf{e}_3 \quad \mathbf{B}_6 = \frac{\sqrt{2}}{2}(\mathbf{e}_1 \otimes \mathbf{e}_2 + \mathbf{e}_2 \otimes \mathbf{e}_1). \quad (2.48)$$

The components of the stress, strain, and stiffness tensor are determined by projection onto the basis vectors

$$\sigma_\alpha = \boldsymbol{\sigma} \cdot \mathbf{B}_\alpha \quad \varepsilon_\alpha = \boldsymbol{\varepsilon} \cdot \mathbf{B}_\alpha \quad C_{\alpha\beta} = \mathbf{B}_\alpha \cdot \mathbb{C}[\mathbf{B}_\beta]. \quad (2.49)$$

Hooke's law can then be represented by

$$\boldsymbol{\sigma} = \sum_{\alpha=1}^6 \sigma_\alpha \mathbf{B}_\alpha = \sum_{\alpha,\beta=1}^6 C_{\alpha\beta} \varepsilon_\beta \mathbf{B}_\alpha. \quad (2.50)$$

Written out, Hooke's law then reads

$$\begin{pmatrix} \sigma_{11} \\ \sigma_{22} \\ \sigma_{33} \\ \sigma_{23} \\ \sigma_{13} \\ \sigma_{12} \end{pmatrix} = \begin{pmatrix} C_{1111} & C_{1122} & C_{1133} & \sqrt{2}C_{1123} & \sqrt{2}C_{1113} & \sqrt{2}C_{1112} \\ & C_{2222} & C_{2233} & \sqrt{2}C_{2223} & \sqrt{2}C_{2213} & \sqrt{2}C_{2212} \\ & & C_{3333} & \sqrt{2}C_{3323} & \sqrt{2}C_{3313} & \sqrt{2}C_{3312} \\ & & & 2C_{2323} & 2C_{2313} & 2C_{2312} \\ & \text{sym.} & & & 2C_{1313} & 2C_{1312} \\ & & & & & 2C_{1212} \end{pmatrix} \begin{pmatrix} \varepsilon_{11} \\ \varepsilon_{22} \\ \varepsilon_{33} \\ \varepsilon_{23} \\ \varepsilon_{13} \\ \varepsilon_{12} \end{pmatrix}.$$

In the three-dimensional linear elastic case, eight symmetry classes can be distinguished. There can be at most 21, in the fully anisotropic (triclinic) case, and at least two, in the isotropic case, independent parameters. In the following, some examples are presented, that play a pronounced role in fiber reinforced composites, each with the number of independent constants  $N_c$  and the number of symmetry planes  $N_p$ .

**Triklinic symmetry** ( $N_c = 21, N_p = 0$ )

$$\mathbb{C} = \begin{pmatrix} C_{1111} & C_{1122} & C_{1133} & \sqrt{2}C_{1123} & \sqrt{2}C_{1113} & \sqrt{2}C_{1112} \\ & C_{2222} & C_{2233} & \sqrt{2}C_{2223} & \sqrt{2}C_{2213} & \sqrt{2}C_{2212} \\ & & C_{3333} & \sqrt{2}C_{3323} & \sqrt{2}C_{3313} & \sqrt{2}C_{3312} \\ & & & 2C_{2323} & 2C_{2313} & 2C_{2312} \\ & \text{sym.} & & & 2C_{1313} & 2C_{1312} \\ & & & & & 2C_{1212} \end{pmatrix} \mathbf{B}_\alpha \otimes \mathbf{B}_\beta \quad (2.51)$$

**Orthotropic symmetry** ( $N_c = 9, N_p = 3$ )

$$\mathbb{C} = \begin{pmatrix} C_{1111} & C_{1122} & C_{1133} & 0 & 0 & 0 \\ & C_{2222} & C_{2233} & 0 & 0 & 0 \\ & & C_{3333} & 0 & 0 & 0 \\ & & & 2C_{2323} & 0 & 0 \\ & \text{sym.} & & & 2C_{1313} & 0 \\ & & & & & 2C_{1212} \end{pmatrix} \mathbf{B}_\alpha \otimes \mathbf{B}_\beta \quad (2.52)$$

**Transverse isotropic symmetry** ( $N_c = 5, N_p = 1 + \infty$ )

$$\mathbb{C} = \begin{pmatrix} C_{1111} & C_{1122} & C_{1133} & 0 & 0 & 0 \\ & C_{1111} & C_{1133} & 0 & 0 & 0 \\ & & C_{3333} & 0 & 0 & 0 \\ & & & 2C_{2323} & 0 & 0 \\ & sym. & & & 2C_{2323} & 0 \\ & & & & & C_{1111} - C_{2222} \end{pmatrix} \mathbf{B}_\alpha \otimes \mathbf{B}_\beta \quad (2.53)$$

**Isotropy** ( $N_c = 2, N_p = \infty$ )

$$\mathbb{C} = \begin{pmatrix} C_{1111} & C_{1122} & C_{1122} & 0 & 0 & 0 \\ & C_{1111} & C_{1122} & 0 & 0 & 0 \\ & & C_{1111} & 0 & 0 & 0 \\ & & & C_{1111} - C_{1122} & 0 & 0 \\ & sym. & & & C_{1111} - C_{1122} & 0 \\ & & & & & C_{1111} - C_{1122} \end{pmatrix} \mathbf{B}_\alpha \otimes \mathbf{B}_\beta \quad (2.54)$$

## 2.3 Damage and Failure

### 2.3.1 Damage

The damage of materials is the process of structure change caused by external impacts as mechanical load, for example, leading to the development and the increase of micro defects. These micro defects change the macroscopic properties. At the final state damage leads to failure. Any kind of debonding is the initiation of damage. For different materials there are different mechanisms. For polymers, damage occurs by the breakage of bonds that exist between the long chains of molecules (Lemaitre, 1992). Damage of composite materials is governed by damage of the individual constituents and debonding be-

tween the constituents. Debonding between the fibers and the polymer matrix as dominating mechanism for SMC composites is investigated by Anagnostou et al. (2018).

**Mechanical representation of damage.** A simple approach to describe damage is using a one-dimensional surface damage variable. This idea is based on Kachanov (1958).

Figure 2.9a shows a cut through a damaged body and a plane  $dA$  defined by its normal  $\mathbf{n}$ . Here,  $dA_D$  is the damaged area, hence the area of the intersections of all microcracks or microcavities. The value

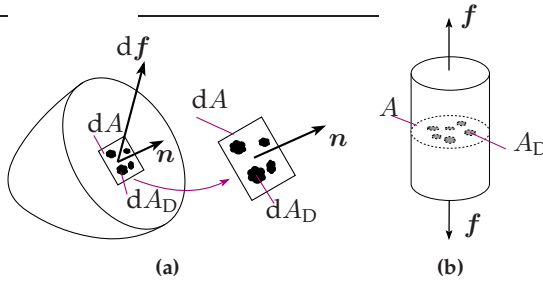


Figure 2.9: Definition of damage (according to Gross and Seelig (2007)).

of damage attached to this area  $dA$  is

$$D(\mathbf{n}) = \frac{dA_D}{dA}. \quad (2.55)$$

It follows from this definition that the value of  $D$  is bounded by 0 and 1, where  $D = 0$  corresponds to the undamaged material and  $D = 1$  corresponds to the completely damaged material. In real load case, failure, corresponding to complete damage, occurs at an earlier state than  $D = 1$ . If  $D$  is independent of  $\mathbf{n}$  the damage state is isotropic.

To describe the influence of damage on the load, Rabotnov (1969) introduced the effective stress concept. If the area  $dA$  is loaded by a

force  $d\mathbf{f}$  as shown in Figure 2.9a, the usual stress vector  $\mathbf{t}$  is

$$\mathbf{t} = \frac{d\mathbf{f}}{dA}. \quad (2.56)$$

The effective stress vector  $\tilde{\mathbf{t}}$  is the force related to the surface that effectively resists the load

$$\tilde{\mathbf{t}} = \frac{d\mathbf{f}}{(dA - dA_D)} = \frac{d\mathbf{f}}{dA(1 - \frac{dA_D}{dA})} = \frac{d\mathbf{f}}{dA(1 - D)} = \frac{\mathbf{t}}{1 - D}. \quad (2.57)$$

For isotropic damage the effective stress tensor is

$$\tilde{\boldsymbol{\sigma}} = \frac{\boldsymbol{\sigma}}{1 - D}. \quad (2.58)$$

A way to describe the stress-strain behavior is the strain equivalence principle proposed by Lemaitre (1971). It means that the constitutive equations for the strain are not modified by the damage or that the true stress that is loading on the material is the effective stress  $\tilde{\boldsymbol{\sigma}}$  and no longer  $\boldsymbol{\sigma}$  (Lemaitre, 1992).

For the example of uniaxial strain (see Figure 2.9b) the linear elastic law is

$$\varepsilon = \frac{\tilde{\sigma}}{E} = \frac{\sigma}{E(1 - D)}. \quad (2.59)$$

The elastic modulus for the damaged material is

$$E_D = E(1 - D). \quad (2.60)$$

For the three dimensional case the isotropically damaged elasticity tensor is

$$\mathbb{C}_D = \mathbb{C}(1 - D), \quad D \in [0, 1). \quad (2.61)$$

For anisotropic damage instead of the scalar damage variable some kind of damage tensor can be used.

**Damage evolution law.** For the damage parameter an evolution law is required. The parameter can depend on strain, energy, stress as well as on the initial anisotropy for example. It is possible to define the evolution law via phenomenological aspects as the observation of macroscopic stiffness degradation or motivated by microstructural aspects or by combination of these as for example performed in Anagnostou (2018).

### 2.3.2 Failure

Failure of materials describes critical states of materials such that they are losing their functionality in any way. This can be via brittle, sudden fracture, ductile fracture or onset of plastic yielding or remaining deformation. Failure can also be considered as the final state of damage. The way of failure depends on the material and also on the load case, i.e. the stress state. It is possible to predict failure by the break of the atomic or molecular bonds, but these stresses are many times greater than the macroscopic failure stresses. In fact, failure on the macroscale is determined by microscopic imperfections as wholes or microcracks, that are existing normally in materials (Lubliner and Papadopoulos, 2014). There are different approaches to describe failure. One way is to derive them via the microstructure and consider the genesis or the propagation of microcracks. This approach is covered by the typical field of fracture mechanics (Rosendahl, 2020). Another way is to simply use mathematical expressions combined with experimental data. These mathematical expressions, the so-called strength hypotheses can be expressed in form of a scalar failure function or criterion. This criterion is often referred to as failure surface, due to the interpretation as a surface in the three-dimensional principal stress space. The basic form of such a failure criterion can be written as follows

$$f(\boldsymbol{\sigma}) = 0, \tag{2.62}$$

with the failure function  $f(\boldsymbol{\sigma})$  dependent on the different stress components. Typical approaches are often of very simple nature. Examples are the principal stress hypothesis or the strain energy hypothesis (see for example Gross et al. (2007)). A more sophisticated approach is presented in Tsai and Wu (1971). This failure criterion is a suitable approach for fiber reinforced composite materials, taking the anisotropic failure behavior into account. For this reason, this criterion is considered in this thesis and presented in more detail in Section 3.3 of the material modeling chapter.

## 2.4 Note on Viscoelasticity

Viscoelasticity is not considered in the material models in this work, but basically considered for the conduction of the experiments. Thus, here are only a few basic remarks, that are relevant to understand the experimental procedure.

Viscoelastic materials combine elastic and viscous properties. Their behavior is time dependent. Viscoelastic materials can be characterized via creep and relaxation behavior in the time area or via the damping behavior in the frequency area.

To describe the creep and relaxation behavior, linear viscoelasticity by the example of uniaxial load is considered. The creep and relaxation function describe the material behavior for special experiments, the creep test and the relaxation test (Gross et al., 2007).

The loading for the creep test can be described by the Heaviside function

$$\sigma(t) = \sigma_0 H(t). \quad (2.63)$$

$H$  is the Heaviside function with

$$H = \begin{cases} 0 & \text{if } t < 0 \\ 1 & \text{if } t \geq 0. \end{cases} \quad (2.64)$$

The response in term of strain is

$$\varepsilon(t) = J(t)\sigma_0, \quad (2.65)$$

where  $J(t)$  is the creep function. Creep loading and a typical course of the creep curve are shown in Figure 2.10.

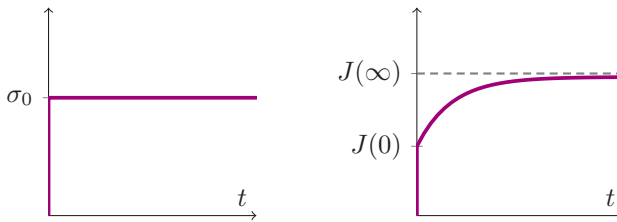


**Figure 2.10:** Stress jump and typical associated course of the creep function.

The loading for the relaxation test is

$$\varepsilon(t) = \varepsilon_0 H(t). \quad (2.66)$$

The response in term of stress is

$$\sigma(t) = G(t)\varepsilon_0 \quad (2.67)$$

with the relaxation function  $G(t)$ . Figure 2.11 shows the corresponding graphs.

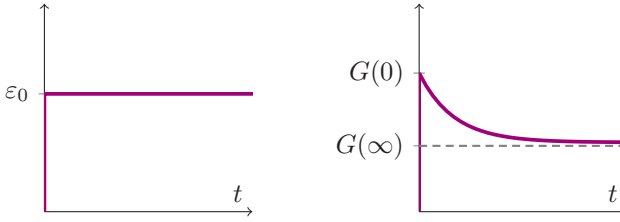


**Figure 2.11:** Strain jump and typical associated course of the relaxation function.

Based on these creep and relaxation functions the creep modulus  $E_C$  and the relaxation modulus  $E_R$  are defined as follows

$$E_C(t) = \frac{1}{J(t)} = \frac{\sigma_0}{\varepsilon(t)}, \quad (2.68)$$

$$E_R(t) = G(t) = \frac{\sigma(t)}{\varepsilon_0}. \quad (2.69)$$

The value of the relaxation function at  $t = 0$  is the instantaneous elasticity modulus which is valid for quasi instantaneous loads. The value of the relaxation function for  $t \rightarrow \infty$  is the equilibrium modulus, which is valid for quasi infinitely slow loads. In literature the instantaneous modulus is often designated as  $E_0$  and the equilibrium modulus as  $E_\infty$ . (Lemaitre and Chaboche, 1990; Gross et al., 2007)

For description in frequency, a sinusoidal load case is considered

$$\sigma(t) = \bar{\sigma}_0 + \tilde{\sigma}_0 \sin(\omega t + \delta) \quad (2.70)$$

$$\varepsilon(t) = \bar{\varepsilon}_0 + \tilde{\varepsilon}_0 \sin(\omega t), \quad (2.71)$$

with the static stress  $\bar{\sigma}_0$ , the amplitude of the dynamic stress  $\tilde{\sigma}_0$ , the static strain  $\bar{\varepsilon}_0$ , the amplitude of the dynamic strain  $\tilde{\varepsilon}_0$ , the phase shift  $\delta$  and the angular frequency  $\omega$ .

Due to the phase shift  $\delta = \omega t$  between stress and strain, the complex

elasticity modulus  $E^*$  is useful to describe the stress-strain relation

$$E^* = E' + iE'' \quad (2.72)$$

Here,  $E'$  is the real part and  $E''$  the imaginary part with

$$E' = E^* \cos(\delta) = \frac{\tilde{\sigma}_0}{\tilde{\varepsilon}_0} \cos(\delta) \quad (2.73)$$

and

$$E'' = E^* \sin(\delta) = \frac{\tilde{\sigma}_0}{\tilde{\varepsilon}_0} \sin(\delta). \quad (2.74)$$

The real part  $E'$  is referred to as the storage modulus. It is a measure of the energy that can be stored during the period of oscillation. In contrast, the imaginary part  $E''$  is related to the energy dissipated during the oscillation period. It is referred to as the loss modulus. The loss factor  $\tan(\delta)$  is calculated from the ratio of the loss modulus and the storage modulus

$$\tan(\delta) = \frac{E''}{E'}. \quad (2.75)$$

The loss factor is an important characteristic value of the viscoelastic material behavior. If the  $\tan(\delta)$  is very large, the material behavior is rather viscous; if it is rather small, the material behavior is predominantly elastic (Grellmann and Seidler, 2011).

**Model rheology.** A suitable method to describe the deformation behavior of viscoelastic materials, is the model rheology. It uses the following basic models: spring for elasticity and damper element for viscosity. Assuming linear viscoelasticity for the elastic and viscous elements there are the basic equations for the stress strain relation

$$\sigma = \mathbb{C}[\varepsilon] \quad (2.76)$$

and

$$\boldsymbol{\sigma} = \mathbb{V}[\dot{\boldsymbol{\varepsilon}}], \quad (2.77)$$

with the stiffness tensor  $\mathbb{C}$  and the viscosity tensor  $\mathbb{V}$ , or for the uniaxial case

$$\sigma = E\varepsilon \quad (2.78)$$

and

$$\sigma = V\dot{\varepsilon} \quad (2.79)$$

with the Young's modulus  $E$  and the viscosity modulus  $V$ . A general model is the Generalized Maxwell Model with one spring parallel to  $n$  Maxwell elements, each consisting of one spring and one damper element (see Figure 2.12).

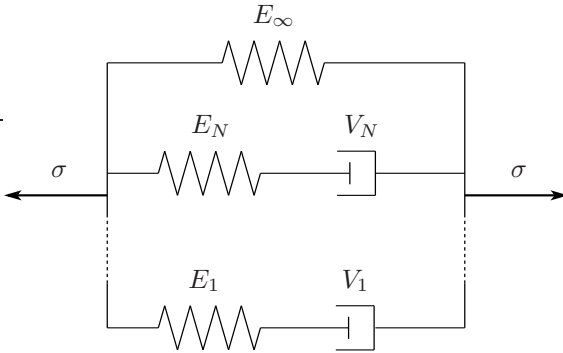


Figure 2.12: Generalized Maxwell model.

The parallel connection leads to

$$\sigma = \sum_{i=1}^N \sigma_i. \quad (2.80)$$

The connection in series in each Maxwell element leads to

$$\varepsilon = \varepsilon_{e,i} + \varepsilon_{v,i} \quad (2.81)$$

and

$$\sigma_i = \sigma_{v,i} = \sigma_{e,i}. \quad (2.82)$$

$\varepsilon$  and  $\sigma$  are the total strain and stress.  $\sigma_i$  is the stress in the  $i^{\text{th}}$  Maxwell element,  $\sigma_{v,i}$  and  $\sigma_{e,i}$  in the  $i^{\text{th}}$  viscous and elastic element.  $\varepsilon_{e,i}$  and  $\varepsilon_{v,i}$  are the strains of the  $i^{\text{th}}$  elastic and the  $i^{\text{th}}$  viscous element.

Equations (2.78) to (2.82) lead to the following two relations that describe the material behavior

$$\sigma = \sum_{i=1}^N E_i (\varepsilon - \varepsilon_{v,i}) \quad (2.83)$$

$$V_i \dot{\varepsilon}_{v,i} = E_i (\varepsilon - \varepsilon_{v,i}). \quad (2.84)$$

These relations can be used to describe the viscoelastic material behavior in terms of time and in terms of frequency.

The relaxation modulus reads then

$$E_R(t) = E_\infty + \sum_{i=1}^N E_i e^{-t/\tau_i}, \quad (2.85)$$

with the relaxation time constant  $\tau = v_i/E_i$ . Storage and loss modulus reads as follows

$$E'(\omega) = E_\infty + \sum_{i=1}^N E_i \frac{(\omega\tau_i)^2}{(1 + \omega\tau_i)^2}, \quad (2.86)$$

$$E''(\omega) = \sum_{i=1}^N E_i \frac{\omega\tau_i}{(1 + \omega\tau_i)^2}. \quad (2.87)$$

## 2.5 Micromechanics

### 2.5.1 Microstructure of Fiber Reinforced Composites

Fiber reinforced composites, especially as the discontinuous fiber reinforced glass SMC of this work, exhibit a particular micro structure. Figure 2.13a depicts a picture of a SMC specimen, photographed against the light so that the light shines through, and thus the microstructure can be seen well even with the naked eye (black markers and solid lines due to experiment). The darker regions and lines correspond to the fibers. It can be seen that the fiber concentration or volume content as well as the orientation of the fibers varies within this specimen. Figure 2.13b depicts a micro computer tomography scan of a specimen detail where the white lines and bars are the fibers. This illustrates the different fiber orientations in more detail.

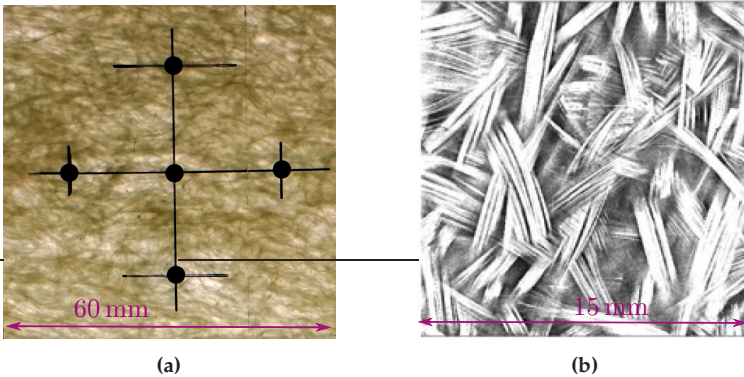


**Figure 2.13:** Microstructure of SMC. (a) Photograph (transillumination image) of SMC specimen (black marker due to experiment) thickness ca 1.5 mm, (b) Computer tomograph observation of SMC specimen, at one plane (taken from Böhlke et al. (2019)).

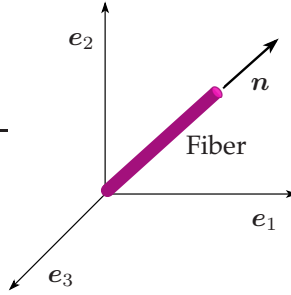


Figure 2.14: Fiber with orientation  $\mathbf{n}$ .

To describe the microstructure, information about fiber volume content, fiber orientation, and the distribution of these as well as the fiber shape, for instance, must be considered. There are different ways to describe these microstructural properties.

## 2.5.2 Fiber Orientation Distribution

In the following the fibers are assumed to be straight and the normalized vector  $\mathbf{n}$  denotes the orientation of a fiber (see Figure 2.14). The fiber orientation can be described by a fiber orientation distribution function (FODF). The FODF represents the probability to find a fiber aligned in direction  $\mathbf{n}$ . An alternative way to interpret or describe the FODF is that it specifies the volume fraction of fibers oriented in direction  $\mathbf{n}$  in relation to the volume of all fibers. The FODF is defined by

$$f : S \rightarrow \mathbb{R}, \quad S := \{\mathbf{n} \in \mathbb{R}^3 \mid \|\mathbf{n}\| = 1\}. \quad (2.88)$$

and has the following properties:

- $f(\mathbf{n})$  is non-negative:  $f(\mathbf{n}) \geq 0, \forall \mathbf{n} \in S$
- $f(\mathbf{n})$  is symmetric:  $f(\mathbf{n}) = f(-\mathbf{n}), \forall \mathbf{n} \in S$ ,
- $f(\mathbf{n})$  is normalized (as being a probability function):  $\int_S f(\mathbf{n}) \, dS = 1$ .

Here,  $S := \{\mathbf{n} \in \mathbb{R}^3 \mid \|\mathbf{n}\| = 1\}$  can be interpreted as the unit sphere with the the surface element  $dS = \sin(\vartheta) d\vartheta d\phi / (4\pi)$ .

For empirical fiber orientations, i.e. for a set of  $m$  discrete fibers, that are equally weighted, the FODF is defined by

$$f(\mathbf{n}) = \frac{1}{m} \sum_{i=1}^m \delta_{\mathbf{n}_i}, \quad (2.89)$$

with the Dirac delta function  $\delta_{\mathbf{n}_i} = \delta(\mathbf{n} - \mathbf{n}_i)$  (Müller and Böhlke (2016), Böhlke et al. (2010), Advani and Tucker (1987)).

### 2.5.3 Fiber Orientation Tensors

A way to describe the fiber orientation distribution in a compacter and often better applicable way, is to use fiber orientation tensors. The fiber orientation tensor  $\mathbb{N}^{(k)}$  of  $k^{\text{th}}$  order can be derived by the FODF by the following equation

$$\mathbb{N}^{(k)} = \int_S f(\mathbf{n}) \mathbf{n}^{\otimes k} dS, \quad (2.90)$$

with

$$\mathbf{n}^{\otimes k} = \underbrace{\mathbf{n} \otimes \mathbf{n} \otimes \dots \otimes \mathbf{n}}_{k \text{ times}}. \quad (2.91)$$

This delivers for the second and fourth order fiber orientation tensors the following expressions

$$\mathbb{N} = \int_S f(\mathbf{n}) \mathbf{n} \otimes \mathbf{n} dS, \quad (2.92)$$

$$\mathbb{N} = \int_S f(\mathbf{n}) \mathbf{n} \otimes \mathbf{n} \otimes \mathbf{n} \otimes \mathbf{n} dS. \quad (2.93)$$

For empirical fiber orientations, i.e. for a set of  $m$  discrete fibers, the fiber orientation tensors can be written the following

$$\mathbb{N}^{(k)} = \frac{1}{m} \sum_{i=1}^m \mathbf{n}_i^{\otimes k}. \quad (2.94)$$

This leads to

$$\mathbf{N} = \frac{1}{m} \sum_{i=1}^m \mathbf{n}_i \otimes \mathbf{n}_i \quad (2.95)$$

and

$$\mathbb{N} = \frac{1}{m} \sum_{i=1}^m \mathbf{n}_i \otimes \mathbf{n}_i \otimes \mathbf{n}_i \otimes \mathbf{n}_i \quad (2.96)$$

for the empirical second and fourth order fiber orientation tensor. The fiber orientation tensors are fully symmetric

$$\mathbf{N} = \mathbf{N}^T, \quad \mathbb{N} = \text{symF}(\mathbb{N}). \quad (2.97)$$

Here,  $\text{symF}(\cdot)$  is the fully symmetrization, that means

$$\mathbb{N} = \mathbb{N}^{\text{TM}} = \mathbb{N}^{\text{TL}} = \mathbb{N}^{\text{TR}} = \mathbb{N}^{\text{TM}}, \quad (2.98)$$

or in index notation

$$N_{ijkl} = N_{klij} = N_{jikl} = N_{ijlk} = N_{kjil}. \quad (2.99)$$

They exhibit the following trace conditions

$$\text{tr}(\mathbf{N}) = 1, \quad \mathbb{N} \cdot (\mathbf{I} \otimes \mathbf{I}) = 1. \quad (2.100)$$

This means that the fiber orientation tensor of second order can be calculated via the fiber orientation tensor of fourth order by

$$\mathbf{N} = \mathbb{N}[\mathbf{I}]. \quad (2.101)$$

The above mentioned formulation for fiber orientation tensors is the generally used formulation introduced for example in Advani and Tucker (1987). Kanatani (1984) designates these tensors as orientation tensors of the first kind. He defines also orientation tensors of the second and third kind, which can be derived from the orientation tensors of the first kind. As the orientation tensors of the second kind don't play a role in this theses, only the orientation tensors of the third kind are presented in addition to the orientation tensors of the first kind. Orientation tensors of the third kind are fully symmetric and traceless and can be calculated from the orientation tensors of the first kind by

$$\mathbb{D}^{\langle k \rangle} = \frac{2k+1}{2^k} \binom{2k}{k} \mathbb{N}^{\langle k \rangle}. \quad (2.102)$$

This leads for the second order to

$$\mathbf{D} = \frac{15}{2}(\mathbf{N} - \frac{1}{3}\mathbf{I}), \quad (2.103)$$

and for the fourth order orientation tensor to

$$\mathbf{D} = \frac{315}{8}(\mathbb{N} - \frac{6}{7}\text{symF}(\mathbf{I} \otimes \mathbf{N}) + \frac{3}{35}\text{symF}(\mathbf{I} \otimes \mathbf{I})). \quad (2.104)$$

For the second and fourth order orientation tensor of the third kind, the symmetry and trace conditions read

$$\mathbf{D} = \mathbf{D}^T, \quad \mathbb{D} = \text{symF}(\mathbb{D}), \quad (2.105)$$

$$\text{tr}(\mathbf{D}) = 0, \quad \mathbb{D} \cdot (\mathbf{I} \otimes \mathbf{I}) = 0. \quad (2.106)$$

The second order orientation tensor of the third kind can not be calculated from the fourth order orientation tensor of the third kind, thus they are independent from each other.

## Chapter 3

# Material Model

## 3.1 Thermoelastic Modeling

### 3.1.1 Thermoelasticity with Constant Coefficients

For the first material model considered in this thesis, it is assumed that all material coefficients are constants. This means in particular that they are independent of temperature. Starting with the assumption that the heat capacity at constant strains is constant

$$c_\varepsilon(\varepsilon, \theta) \stackrel{!}{=} c_0. \quad (3.1)$$

leads with Equation (2.38)

$$c_\varepsilon = -\theta \frac{\partial^2 \psi(\varepsilon, \theta)}{\partial \theta^2} \quad (3.2)$$

by twofold integration to the following form of the free energy

$$\psi(\varepsilon, \theta) = \psi_\theta(\theta) + \Delta\theta k_1(\varepsilon) + k_2(\varepsilon) + k_0. \quad (3.3)$$

Here,

$$\Delta\theta = \theta - \theta_0 \quad (3.4)$$

is a temperature difference referred to a reference temperature  $\theta_0$  and  $k_1(\varepsilon)$  and  $k_2(\varepsilon)$  are unknown functions.  $\psi_\theta(\theta)$  is the purely temperature-dependent part of the free energy

$$\psi_\theta(\theta) = c_0 \left( \Delta\theta - \theta \ln \left( \frac{\theta}{\theta_0} \right) \right). \quad (3.5)$$

The assumption of constant temperature stress coefficients

$$\beta \stackrel{!}{=} \beta_0 \quad (3.6)$$

leads with Equation (2.39)

$$\beta = -\varrho_0 \frac{\partial^2 \psi(\varepsilon, \theta)}{\partial \varepsilon \partial \theta}, \quad (3.7)$$

where  $\varrho_0$  is the constant mass density, to

$$-\varrho_0 \frac{\partial k_1(\varepsilon)}{\partial \varepsilon} = \beta_0. \quad (3.8)$$

This defines the unknown function  $k_1(\varepsilon)$

$$k_1(\varepsilon) = -\frac{1}{\varrho_0} \beta_0 \cdot \varepsilon. \quad (3.9)$$

The next assumption is that the stress has the form of the classical linear thermoelastic Hooke's law

$$\boldsymbol{\sigma} \stackrel{!}{=} \mathbb{C}_0[\boldsymbol{\varepsilon}] - \beta_0 \Delta\theta \quad (3.10)$$

with the constant stiffness tensor  $\mathbb{C}_0$  (note:  $\boldsymbol{\sigma} = \boldsymbol{\sigma}^{eq}$ , see Equation (2.26)). Equation (2.31)

$$\boldsymbol{\sigma} = \varrho_0 \frac{\partial \psi(\varepsilon, \theta)}{\partial \varepsilon} \quad (3.11)$$

leads by differentiating the free energy to

$$\boldsymbol{\sigma} = -\beta_0 \Delta\theta + \varrho_0 \frac{\partial k_2(\boldsymbol{\varepsilon})}{\partial \boldsymbol{\varepsilon}}. \quad (3.12)$$

This defines with Equation (3.10) the unknown function  $k_2(\boldsymbol{\varepsilon})$

$$k_2(\boldsymbol{\varepsilon}) = \frac{1}{2\varrho_0} \boldsymbol{\varepsilon} \cdot \mathbb{C}_0[\boldsymbol{\varepsilon}]. \quad (3.13)$$

For the stiffness tensor yields according to Equation (2.42)

$$\mathbb{C}_0 = \frac{\partial \boldsymbol{\sigma}}{\partial \boldsymbol{\varepsilon}} = \varrho_0 \frac{\partial^2 \psi(\boldsymbol{\varepsilon}, \theta)}{\partial \boldsymbol{\varepsilon}^2}. \quad (3.14)$$

Thus, the stiffness tensor  $\mathbb{C}_0$  has the major symmetry ( $C_{ijkl} = C_{klij}$ ) and the two minor symmetries ( $C_{ijkl} = C_{jikl} = C_{ijlk}$ ).

The three assumptions for the heat capacity (Equation (3.1)), for the thermal stress coefficients (Equation (3.6)) and the stress strain relation (Equation (3.10)) define the free energy totally. It holds

$$\psi(\boldsymbol{\varepsilon}, \theta) = \psi_\theta(\theta) - \frac{1}{\varrho_0} \Delta\theta \beta_0 \cdot \boldsymbol{\varepsilon} + \frac{1}{2\varrho_0} \boldsymbol{\varepsilon} \cdot \mathbb{C}_0[\boldsymbol{\varepsilon}] + k_0. \quad (3.15)$$

The constant  $k_0$  has no relevance for the thermoelastic properties because only the derivatives are in the balance equations. For the entropy, Equation (2.32)

$$\eta = -\frac{\partial \psi(\boldsymbol{\varepsilon}, \theta)}{\partial \theta} \quad (3.16)$$

and the form of the free energy in Equation (3.15) lead to the following form

$$\eta(\boldsymbol{\varepsilon}, \theta) = c_0 \ln\left(\frac{\theta}{\theta_0}\right) + \frac{1}{\varrho_0} \boldsymbol{\beta} \cdot \boldsymbol{\varepsilon}. \quad (3.17)$$

Alternatively, the material function of Equation (3.10) (Hooke's law) can also be expressed as a function of compliance and coefficient of

thermal expansion by transforming Hooke's law into strain-explicit form. Rearranging Equation (3.10) leads to

$$\varepsilon = \mathbb{C}_0^{-1}[\boldsymbol{\sigma}] + \mathbb{C}_0^{-1}[\boldsymbol{\beta}_0 \Delta \theta]. \quad (3.18)$$

Plugging Equation (3.18) into Equation (2.41) results in

$$\boldsymbol{\alpha} = \left. \frac{\partial \varepsilon}{\partial \theta} \right|_{\boldsymbol{\sigma}} = \mathbb{C}_0^{-1}[\boldsymbol{\beta}_0] = \boldsymbol{\alpha}_0 \quad (3.19)$$

for the thermal expansion coefficient. The compliance which is defined as in Equation (2.43) results in

$$\mathbb{S} = \frac{\partial \varepsilon}{\partial \boldsymbol{\sigma}} = \mathbb{C}_0^{-1} = \mathbb{S}_0. \quad (3.20)$$

Hooke's law in strain-explicit form can thus be written as

$$\varepsilon = \mathbb{S}_0[\boldsymbol{\sigma}] + \boldsymbol{\alpha}_0 \Delta \theta. \quad (3.21)$$

For the heat conduction two assumptions are made. The first one is that the heat conduction tensor is linear in temperature gradient and the second one is that the thermal conductivity coefficient  $\kappa_0$  is constant. This gives the following equation

$$\mathbf{q} = -\kappa_0 \mathbf{g}. \quad (3.22)$$

This is known as the classical Fourier's law of heat conduction. With this Ansatz, the reduced dissipation inequality (see Equation (2.34)) has the following form

$$\mathbf{g} \cdot \kappa_0 \mathbf{g} \geq 0. \quad (3.23)$$

In summary, for the material model with constant coefficients, there are the following coefficients with the corresponding material parameters for the fully anisotropic case:

- Mass density  $\varrho_0$  (unit:  $\text{kg}/\text{m}^3$ ): scalar, 1 parameter
- Reference temperature  $\theta_0$  (unit: K): scalar, 1 parameter
- Heat capacity  $c_0$  (unit:  $\text{J}/(\text{kgK})$ ): scalar, 1 parameter
- Stiffness tensor  $\mathbb{C}_0$  (unit: Pa) or compliance tensor  $\mathbb{S}_0$  ( $1/\text{Pa}$ ): symmetric (major and minor) fourth order tensor, 21 parameters
- Thermal stress coefficient  $\beta_0$  (unit:  $\text{Pa}/\text{K}$ ) or thermal expansion coefficient  $\alpha_0$  (unit:  $1/\text{K}$ ): symmetric second order tensor, 6 parameters
- Thermal conductivity coefficient  $\kappa_0$  (unit:  $\text{W}/(\text{mK})$ ): symmetric second order tensor, 6 parameters

In total there are 36 material parameters, which are summarized in Table 3.1.

Coefficient	Var.	Type	NP	Unit
Mass density $\varrho_0$	$\varrho_0$	scalar	1	$\text{kg}/\text{m}^3$
Reference temp. $\theta_0$	$\theta_0$	scalar	1	K
Heat capacity $c$	$c_0$	scalar	1	$\text{J}/(\text{kgK})$
Stiffness tensor $\mathbb{C}$ or Compl. tensor $\mathbb{S}$	$\mathbb{C}_0$	sym. $4^{\text{th}}$ order tensor	21	Pa  $1/\text{Pa}$
Th. stress coeff. $\beta$ or Th. exp. coeff. $\alpha$	$\beta_0$	sym. $2^{\text{nd}}$ order tensor	6	$\text{Pa}/\text{K}$  $1/\text{K}$
Th. Cond. Coeff. $\kappa$	$\kappa_0$	sym. $2^{\text{nd}}$ o. ten.	6	$\text{W}/(\text{mK})$

**Table 3.1:** Coefficients for the material model with constant coefficients with corresponding variables (var.), type, number of parameters (NP) and unit.

Considering special symmetry cases the number of parameters reduces. For the isotropic case the number of parameters reduces to 7 in total.

The stiffness tensor has 2 parameters as written in Equation (2.54). For the thermal stress coefficient or the thermal expansion coefficient yields then

$$\beta_0 = \beta_0 \mathbf{I}, \quad \alpha_0 = \alpha_0 \mathbf{I}. \quad (3.24)$$

For the orthotropic case the number of parameters reduces to 18 in total. The stiffness tensor has 9 parameters as written in Equation (2.52). For the thermal stress coefficient or the thermal expansion coefficient yields then

$$\beta_0 = \begin{pmatrix} \beta_{11} & 0 & 0 \\ 0 & \beta_{22} & 0 \\ 0 & 0 & \beta_{33} \end{pmatrix}, \quad \alpha_0 = \begin{pmatrix} \alpha_{11} & 0 & 0 \\ 0 & \alpha_{22} & 0 \\ 0 & 0 & \alpha_{33} \end{pmatrix}. \quad (3.25)$$

For the transverse isotropic case the number of parameters reduces to 12 in total. The stiffness tensor has 5 parameters as written in Equation (2.53). For the thermal stress coefficient or the thermal expansion coefficient yields then for the symmetric plane in  $e_1$ -  $e_2$  direction.

$$\beta_0 = \begin{pmatrix} \beta_{11} & 0 & 0 \\ 0 & \beta_{11} & 0 \\ 0 & 0 & \beta_{33} \end{pmatrix}, \quad \alpha_0 = \begin{pmatrix} \alpha_{11} & 0 & 0 \\ 0 & \alpha_{11} & 0 \\ 0 & 0 & \alpha_{33} \end{pmatrix}. \quad (3.26)$$

In this thesis the fully anisotropic case is considered.

### 3.1.2 Thermoelasticity with Temperature-Dependent Coefficients

The mass density is still assumed to be constant  $\varrho \approx \varrho_0$ . For the material model with temperature-dependent coefficients, starting point is the assumption that the heat capacity is linear in temperature

$$c_\varepsilon \stackrel{!}{=} c_0 + c'_0 \Delta\theta, \quad (3.27)$$

where  $\Delta\theta$  is a temperature difference defined as in Equation (3.4), and  $c_0$  and  $c'_0$  are constants. This leads with Equation (2.38) to the following form of the free energy

$$\psi(\boldsymbol{\varepsilon}, \theta) = \psi_\theta(\theta) + \Delta\theta k_1(\boldsymbol{\varepsilon}) + k_2(\boldsymbol{\varepsilon}) + k_0, \quad (3.28)$$

where  $k_1(\boldsymbol{\varepsilon})$  and  $k_2(\boldsymbol{\varepsilon})$  are unknown functions.  $\psi_\theta(\theta)$  is the purely temperature-dependent part of the free energy

$$\psi_\theta(\theta) = (c_0 - c'_0\theta_0) \left( \Delta\theta - \theta \ln\left(\frac{\theta}{\theta_0}\right) \right) - \frac{1}{2}c'_0\Delta\theta^2. \quad (3.29)$$

The temperature stress coefficients have with Equation (2.39) and Equation (3.28) the following form

$$\boldsymbol{\beta} = -\varrho_0 \frac{\partial^2 \psi(\boldsymbol{\varepsilon}, \theta)}{\partial \boldsymbol{\varepsilon} \partial \theta} = -\varrho_0 \frac{\partial k_1(\boldsymbol{\varepsilon})}{\partial \boldsymbol{\varepsilon}}. \quad (3.30)$$

Thus, they can only depend on strain and not on temperature. The assumption for the temperature stress coefficients is that they depend linearly on strain

$$\boldsymbol{\beta}(\boldsymbol{\varepsilon}) \stackrel{!}{=} \boldsymbol{\beta}_0 - \mathbb{C}'_0[\boldsymbol{\varepsilon}]. \quad (3.31)$$

(The symbol  $\mathbb{C}'_0$  is chosen due to later appearance in the stiffness tensor.) With this Ansatz and Equation (3.30) follows for the function  $k_1(\boldsymbol{\varepsilon})$

$$k_1(\boldsymbol{\varepsilon}) = \frac{1}{2\varrho_0} \boldsymbol{\varepsilon} \cdot \mathbb{C}'_0[\boldsymbol{\varepsilon}] - \frac{1}{\varrho_0} \boldsymbol{\beta}_0 \cdot \boldsymbol{\varepsilon}. \quad (3.32)$$

For the stress the following assumption is made

$$\boldsymbol{\sigma}(\boldsymbol{\varepsilon}, \theta) \stackrel{!}{=} (\mathbb{C}_0 + \mathbb{C}'_0\Delta\theta)[\boldsymbol{\varepsilon}] - \boldsymbol{\beta}_0\Delta\theta. \quad (3.33)$$

For the stress yields with Equations (2.31), (3.28) and the known function  $k_1(\varepsilon)$  (see Equation (3.32))

$$\begin{aligned}
 \boldsymbol{\sigma}(\varepsilon, \theta) &= \varrho_0 \frac{\partial \psi(\varepsilon, \theta)}{\partial \varepsilon} \\
 &= \varrho_0 \left( \Delta \theta \frac{\partial k_1(\varepsilon)}{\partial \varepsilon} + \frac{\partial k_2(\varepsilon)}{\partial \varepsilon} \right) \\
 &= \mathbb{C}'_0[\varepsilon] \Delta \theta - \frac{1}{\varrho_0} \beta_0 \Delta \theta + \varrho_0 \frac{\partial k_2(\varepsilon)}{\partial \varepsilon}.
 \end{aligned} \tag{3.34}$$

Herewith and with the assumption for the stress (Equation (3.33)) the function  $k_2(\varepsilon)$  is defined

$$k_2(\varepsilon) = \frac{1}{2\varrho_0} \varepsilon \cdot \mathbb{C}_0[\varepsilon]. \tag{3.35}$$

With Equations (2.42) and (3.33) the stiffness tensor is given by

$$\mathbb{C} = \frac{\partial \boldsymbol{\sigma}}{\partial \varepsilon} = \mathbb{C}_0 + \mathbb{C}'_0 \Delta \theta. \tag{3.36}$$

For the free energy this finally results in

$$\begin{aligned}
 \psi(\varepsilon, \theta) &= \psi_\theta(\theta) + k_0 \\
 &\quad - \frac{1}{\varrho_0} \beta_0 \Delta \theta \cdot \varepsilon \\
 &\quad + \frac{1}{2\varrho_0} \varepsilon \cdot (\mathbb{C}_0 + \mathbb{C}'_0 \Delta \theta)[\varepsilon].
 \end{aligned} \tag{3.37}$$

For the entropy follows

$$\begin{aligned}
 \eta(\varepsilon, \theta) &= -\frac{\partial \psi(\varepsilon, \theta)}{\partial \theta} \\
 &= \eta_\theta(\theta) - k_1(\varepsilon)
 \end{aligned} \tag{3.38}$$

with  $k_1(\varepsilon)$  as in Equation (3.32) and the purely temperature-dependent part of the entropy  $\eta_\theta(\theta)$

$$\eta_\theta(\theta) = (c_0 - c'_0\theta_0) \ln\left(\frac{\theta}{\theta_0}\right) + c'_0\Delta\theta. \quad (3.39)$$

Alternatively, as for the material model with constant coefficients, the material function of Equation (3.33) can also be expressed as a function of compliance and thermal expansion coefficient by transforming the stress strain relation into strain-explicit form. Rearranging Equation (3.33) leads to

$$\varepsilon = (\mathbb{C}_0 + \mathbb{C}'_0\Delta\theta)^{-1}[(\boldsymbol{\sigma} + \boldsymbol{\beta}_0\Delta\theta)]. \quad (3.40)$$

Using Equation (2.41) the thermal expansion coefficient is obtained by differentiating Equation (3.40) with respect to the temperature. This leads to the following expression

$$\begin{aligned} \alpha &= \left. \frac{\partial \varepsilon}{\partial \theta} \right|_{\boldsymbol{\sigma}} \\ &= -(\mathbb{C}_0 + \mathbb{C}'_0\Delta\theta)^{-1} \mathbb{C}'_0 (\mathbb{C}_0 + \mathbb{C}'_0\Delta\theta)^{-1} [\boldsymbol{\sigma} + \boldsymbol{\beta}_0\Delta\theta] \\ &\quad + (\mathbb{C}_0 + \mathbb{C}'_0\Delta\theta)^{-1} [\boldsymbol{\beta}_0]. \end{aligned} \quad (3.41)$$

The compliance is obtained by differentiating Equation (3.40) with respect to the stress

$$\mathbb{S} = \frac{\partial \varepsilon}{\partial \boldsymbol{\sigma}} = (\mathbb{C}_0 + \mathbb{C}'_0\Delta\theta)^{-1}. \quad (3.42)$$

For the heat conduction the same assumptions as for the material model with constant coefficients are made. So, here also applies the Fourier's law of heat conduction (see also Equation (3.22))

$$\mathbf{q} = -\kappa_0 \mathbf{g} \quad (3.43)$$

with the constant thermal conductivity coefficient  $\kappa_0$ . In summary, for the material model with temperature-dependent coefficients, there are the following coefficients with the corresponding material parameters for the fully anisotropic case:

- Mass density  $\rho_0$  (unit:  $\text{kg}/\text{m}^3$ ): scalar, 1 parameter
- Reference temperature  $\theta_0$  (unit: K): scalar, 1 parameter
- Heat capacity  $c$  (unit:  $\text{J}/(\text{kgK})$ )
  - $c_0$  (unit:  $\text{J}/(\text{kgK})$ ): scalar, 1 parameter
  - $c'_0$  (unit:  $\text{J}/(\text{kgK}^2)$ ): scalar, 1 parameter
- Stiffness tensor  $\mathbb{C}$  (unit: Pa) or compliance tensor  $\mathbb{S}$  ( $1/(\text{Pa})$ )
  - $\mathbb{C}_0$  (unit: Pa): symmetric (major and minor) fourth order tensor, 21 parameters
  - $\mathbb{C}'_0$  (unit: Pa/K): symmetric (major and minor) fourth order tensor, 21 parameters
- Thermal stress coefficient  $\beta$  (unit: Pa/K) or thermal expansion coefficient  $\alpha$  (unit:  $1/\text{K}$ )
  - $\beta_0$  (unit: Pa/K) : symmetric second order tensor, 6 parameters
- Thermal conductivity coefficient  $\kappa_0$  (unit:  $\text{W}/(\text{mK})$ ): symmetric second order tensor, 6 parameters

In total there are 58 material parameters, which are summarized in Table 3.2.

Coefficient	var.	type	NP	unit
Mass density $\varrho_0$	$\varrho_0$	scalar	1	kg/m <sup>3</sup>
Reference temp. $\theta_0$	$\theta_0$	scalar	1	K
Heat capacity $c$	$c_0, c'_0$	scalar	1 + 1	J/(kgK)
Stiffness tensor $\mathbb{C}$		sym.		Pa
or	$\mathbb{C}_0, \mathbb{C}'_0$	4 <sup>th</sup> order	21 + 21	
Compl. tensor $\mathbb{S}$		tensor		1/Pa
Th. stress coeff. $\beta$		sym.		Pa/K
or	$\beta_0$	2 <sup>nd</sup> order	6	
Th. exp. coeff. $\alpha$		tensor		1/K
Th. cond. coeff. $\kappa$	$\kappa_0$	sym. 2 <sup>nd</sup> o. ten.	6	W/(mK)

**Table 3.2:** Coefficients for the material model with temperature-dependent coefficients with corresponding variables (var.), type, number of parameters (NP) and unit.

To reduce the number of parameters an additional assumption for the temperature-dependent stiffness can be made. For  $\mathbb{C}'_0$  the following Ansatz is chosen

$$\mathbb{C}'_0 = \mathbb{C}_0 C'_0 \quad (3.44)$$

with  $C'_0$  being a constant scalar parameter (unit: 1/K). This reduces the number of parameters for the stiffness tensor from 42 to 22, and for the total number of parameters from 58 to 38, which are only two additional parameters in comparison to the material model with constant coefficients. These are the parameter for the temperature dependence of the heat capacity  $c'_0$ , and the parameter of the temperature dependence of the stiffness tensor  $C'_0$ . The dependence on temperature of the thermal stress coefficient and the thermal expansion coefficient result also in terms of this parameter  $C'_0$ .

Considering the same special symmetry cases as for the material model with constant coefficients, the following numbers of parameters yields.

The total number of parameters of the isotropic case is then 9, for the orthotropic case 20 and for the transverse isotropic case 14, which are for each case 2 additional parameters.

The assumption in Equation (3.44) leads to the following formulation for the stiffness tensor:

$$\mathbb{C} = \mathbb{C}_0 + \mathbb{C}'_0 \Delta\theta = \mathbb{C}_0(1 + \mathbb{C}'_0 \Delta\theta), \quad (3.45)$$

The thermal stress coefficient reads then

$$\boldsymbol{\beta}(\boldsymbol{\varepsilon}) = \boldsymbol{\beta}_0 - \mathbb{C}_0 \mathbb{C}'_0 [\boldsymbol{\varepsilon}]. \quad (3.46)$$

and the thermal expansion coefficient simplifies to

$$\boldsymbol{\alpha} = (1 + \mathbb{C}'_0 \Delta\theta)^{-2} (-\mathbb{C}'_0 \mathbb{C}_0^{-1} [\boldsymbol{\sigma}] + \mathbb{C}_0^{-1} [\boldsymbol{\beta}_0]). \quad (3.47)$$

For  $\Delta\theta = 0$  and  $\boldsymbol{\sigma} = \mathbf{0}$ , this expression reduces to  $\boldsymbol{\alpha} = \mathbb{C}_0^{-1} [\boldsymbol{\beta}_0]$ , which can be denoted as  $\boldsymbol{\alpha}_0$  and for  $\Delta\theta = 0$  and  $\boldsymbol{\sigma} \neq \mathbf{0}$  to  $-\mathbb{C}'_0 \mathbb{C}_0^{-1} [\boldsymbol{\sigma}] + \mathbb{C}_0^{-1} [\boldsymbol{\beta}_0]$  which can be denoted as  $\boldsymbol{\alpha}_{\sigma 0}$

$$\boldsymbol{\alpha}_0 = \mathbb{C}_0^{-1} [\boldsymbol{\beta}_0] \quad (3.48)$$

$$\boldsymbol{\alpha}_{\sigma 0} = \mathbb{C}_0^{-1} [-\mathbb{C}'_0 \boldsymbol{\sigma} + \boldsymbol{\beta}_0]. \quad (3.49)$$

Also for the model with temperature-dependent coefficients the fully anisotropic case is considered in this thesis.

## 3.2 Micromechanical Modeling of Thermoelasticity

### 3.2.1 Constant Coefficients

The general Ansatz is the assumption of linearity of the directional (tensorial) material coefficients in fiber orientation tensor. These are the stiffness tensor  $\mathbb{C}$  (or compliance tensor  $\mathbb{S}$ ), the thermal expansion coefficient  $\alpha$  (or the thermal stress coefficient  $\beta$ ) and the thermal conductivity coefficient  $\kappa$ . Therefore, in the following, decompositions of second and fourth order tensors in general are considered, that can be applied to the material coefficient tensors.

Second order tensors can be decomposed into a spherical and a deviatoric part

$$\mathbf{A} = \mathbf{A}^\circ + \mathbf{A}' \quad (3.50)$$

with

$$\mathbf{A}^\circ = \frac{1}{3}\text{tr}(\mathbf{A})\mathbf{I}, \quad \mathbf{A}' = \mathbf{A} - \frac{1}{3}\text{tr}(\mathbf{A})\mathbf{I}. \quad (3.51)$$

For fourth order tensors the harmonic decomposition (Böhlke and Brüggemann (2001), Cowin (1989)) can be applied

$$\mathbb{A} = h_1\mathbb{P}_1 + h_2\mathbb{P}_2 + \mathbf{H}'_1 \otimes \mathbf{I} + \mathbf{I} \otimes \mathbf{H}'_1 + 4\mathbb{J}[\mathbf{H}'_2] + \mathbb{H}' \quad (3.52)$$

with the two projectors

$$\mathbb{P}_1 = \frac{1}{3}\mathbf{I} \otimes \mathbf{I}, \quad \mathbb{P}_2 = \mathbb{I}^{\mathbb{S}} - \mathbb{P}_1 \quad (3.53)$$

where  $\mathbb{I}^{\mathbb{S}}$  is the fourth order identity tensor on symmetric second order tensors. The operator  $\mathbb{J}$  is defined as

$$\mathbb{J}[\mathbf{A}] = \frac{1}{4}(A_{im}\delta_{jn} + A_{in}\delta_{jm} + \delta_{im}A_{jn} + \delta_{in}A_{jm})\mathbf{e}_i \otimes \mathbf{e}_j \otimes \mathbf{e}_m \otimes \mathbf{e}_n. \quad (3.54)$$

The first two terms describe the isotropic part.  $\mathbf{H}'_1$  and  $\mathbf{H}'_2$  are deviatoric tensors and  $\mathbb{H}$  is the harmonic part. The deviatoric and harmonic tensors are completely symmetric and traceless. (For the exact calculation of the parts see Böhlke and Brüggemann (2001)).

The fiber orientation tensors of the third kind according to Kanatani (1984) (see Section 2.5.3) of second  $\mathbf{D}$  and fourth order  $\mathbb{D}$  satisfy the properties of  $\mathbf{A}'$  or  $\mathbf{H}'$  and  $\mathbb{H}'$ , respectively.

Thus, the Ansatz for directional (tensorial) material parameters of second and fourth order is to replace the deviatoric and harmonic tensors in the decompositions by the second and fourth order kanatani third kind orientation tensors and to add a constant at each. These constants are then the remaining parameters.

The Ansatz is applied on the stiffness tensor  $\mathbb{C}$ , the thermal expansion coefficient  $\alpha$  and the thermal conductivity coefficient  $\kappa$ .

The Ansatz for the stiffness tensor reads then

$$\mathbb{C}_0 = k_1 \mathbb{P}_1 + k_2 \mathbb{P}_2 + k_3 (\mathbf{D} \otimes \mathbf{I} + \mathbf{I} \otimes \mathbf{D}) + k_4 \mathbb{J}[\mathbf{D}] + k_5 \mathbb{D}, \quad (3.55)$$

the Ansatz for the coefficient of thermal expansion

$$\alpha_0 = k_{\alpha 1} \mathbf{I} + k_{\alpha 2} \mathbf{D}, \quad (3.56)$$

and the Ansatz for the coefficient of thermal conductivity

$$\kappa_0 = k_{\kappa 1} \mathbf{I} + k_{\kappa 2} \mathbf{D}. \quad (3.57)$$

Thus the number of independent parameters reduces from 21 to 5 for the stiffness tensor, and from 6 to 2 for the thermal expansion coefficient and the thermal conductivity coefficient, when  $\mathbf{D}$  and  $\mathbb{D}$  are known. These parameters are independent on the fiber orientation, because the fiber orientation is taken into account via  $\mathbf{D}$  and  $\mathbb{D}$ . They can depend on the properties of the individual materials, the fiber volume fraction, for instance. Assuming these as constant, the parameter can

be assumed as constant and the differences in the material coefficients comes only from the fiber orientation tensors.

### 3.2.2 Temperature-Dependent Coefficients

For the micromechanical material model with temperature-dependent coefficients, it is assumed that the coefficients at reference temperature have the same form in dependence of the microstructure as the constant coefficients in Section 3.2.1. This leads for the stiffness tensor to

$$\mathbb{C} = \mathbb{C}_0(1 + C'_0 \Delta\theta) \quad (3.58)$$

with

$$\mathbb{C}_0 = \mathbb{C}_0(\mathbf{D}, \mathbb{D}) \quad (3.59)$$

as defined in Equation (3.55).

For the thermal expansion coefficient yields then

$$\boldsymbol{\alpha} = (1 + C'_0 \Delta\theta)^{-2} (-C'_0 \mathbb{C}_0^{-1}[\boldsymbol{\sigma}] + \mathbb{C}_0^{-1}[\boldsymbol{\beta}_0]), \quad (3.60)$$

with

$$\mathbb{C}_0^{-1}[\boldsymbol{\beta}_0] = \boldsymbol{\alpha}_0 = \boldsymbol{\alpha}_0(\mathbf{D}), \quad (3.61)$$

where  $\boldsymbol{\alpha}_0(\mathbf{D})$  is defined as in Equation (3.57). Here,  $\boldsymbol{\alpha}_0$  is the thermal expansion coefficient at reference temperature ( $\Delta\theta = 0$ ) and without stress application ( $\boldsymbol{\sigma} = \mathbf{0}$ ) as defined in Equation (3.48).  $C'_0$  and  $c'_0$  are assumed to be non-dependent on fiber orientation.

For the coefficient of thermal conductivity still yields Equation (3.57), as it is assumed to be constant in temperature.

### 3.3 Modeling of Failure

**General Formulation.** The basic form of the Tsai-Wu failure criterion (Tsai and Wu, 1971) is a scalar failure function as a function of strength tensors and stress components

$$f = \mathbf{F} \cdot \boldsymbol{\sigma} + \boldsymbol{\sigma} \cdot \mathbb{F}[\boldsymbol{\sigma}] - 1, \quad (3.62)$$

where failure is expected when  $f = 0$ .  $\mathbf{F}$  and  $\mathbb{F}$  (or  $F_{ij}$  and  $F_{ijkl}$  in index notation) are strength tensors of second and fourth order.  $\mathbf{F}$  and  $\mathbb{F}$  satisfy symmetry conditions to be sensible with the symmetry properties of the stress tensor.  $\mathbf{F}$  is symmetric ( $F_{ij} = F_{ji}$ ) and  $\mathbb{F}$  has the major ( $F_{ijkl} = F_{klij}$ ) and the two minor ( $F_{ijkl} = F_{jikl} = F_{ijlk}$ ) symmetries. The number of components is thus 6 for  $\mathbf{F}$  and 21 for  $\mathbb{F}$ , which makes in total 27 parameters for the general anisotropic three dimensional case.  $\mathbb{F}$  is positive definite, to be physically meaningful. This ensures that its geometrical representation has a convex shape, what physically means that there is a finite failure for each stress state. In the three dimensional principal stress space the geometrical interpretation of Equation (3.62) is an ellipsoid. The remaining stresses are then  $\sigma_{11} = \sigma_1, \sigma_{22} = \sigma_2, \sigma_{33} = \sigma_3$ . Here, the components  $F_{1111}, F_{2222}, F_{3333}$  describe the dimension of the ellipsoid in the three directions, physically meaning the anisotropic strength. The components  $F_{11}, F_{22}, F_{33}$  describe the shift of the ellipsoid, meaning the tension-compression difference of the strength. The parameter  $F_{1122}$  describes the inclination of the ellipsoid, meaning that a combined/multiaxial stress state can increase or decrease the strength compared to a uniaxial stress state.

**Special cases.** Considering the general anisotropic case in a planar stress state, all components in Equation (3.62) that contain a stress component in the third direction vanish (for a planar stress state in  $e_1$ - $e_2$ -direction only  $\sigma_{11}, \sigma_{22}$  and  $\sigma_{12}$  are remaining). The number of

components in  $\mathbf{F}$  remaining in Equation (3.62) reduces then to 3 and in  $\mathbb{F}$  to 6, which are in total 9 parameters.

Considering material symmetries in the coordinate system of the principal directions of the material symmetry, the number of parameters reduces.

For orthotropic material symmetry the shear normal stress coupling terms in  $\mathbb{F}$  (e.g.  $F_{1123}$ ) and the coupling terms between shear stresses (e.g.  $F_{2312}$ ) vanish. The off-diagonal terms of  $\mathbf{F}$  vanish ( $F_{23} = F_{13} = F_{12} = 0$ ), this means that the positive and negative shear strength are equal. This reduces the number of parameters to 3 for  $\mathbf{F}$  and 9 for  $\mathbb{F}$ , which makes in total 12 parameters.

For transverse isotropic material symmetry the number of parameters reduces to 2 and 5 for  $\mathbf{F}$  and  $\mathbb{F}$  respectively, being a special case of orthotropic material behavior with  $F_{1111} = F_{2222}$ ,  $F_{1133} = F_{2233}$ ,  $F_{2323} = F_{1313}$  and  $F_{1212} = \frac{1}{2}(F_{1111} - F_{1122})$ .

Considering an isotropic material behavior only 2 parameters for  $\mathbb{F}$  and 1 parameter for  $\mathbf{F}$  are remaining.

Assuming additionally that the tensile and compression strengths are equal, only the 2 parameters in  $\mathbb{F}$ ,  $F_{1111}$  and  $F_{1122}$  are remaining. In the principal stress space, the geometrical representation is then a sphere around the coordinate origin with the radius corresponding to the failure stress for uniaxial tension or compression in an arbitrary direction.

**Experimental determination of the parameters.** All the parameters of  $F_{ij}$  and  $F_{ijkl}$  in Equation (3.62) can be determined via experiments in which special stress cases are applied. In the following the special case of orthotropic material symmetry in planar stress state is considered for the experimental determination of the parameters. For details on the the identification of all parameters the reader is referred to Tsai and Wu (1971).

**Orthotropic symmetry in planar stress state - experimental identification of parameters.** As material model for the parameter identification (without considering the microstructure) orthotropic material symmetry is assumed. Additionally, a planar stress state is considered. For the orthotropic case in a planar stress state, there are 2 and 4 components for  $F_{ij}$  and  $F_{ijkl}$ , respectively. There are the following 6 parameters for planar stress in the  $e_1$ - $e_2$ -direction:  $F_{11}$ ,  $F_{22}$ ,  $F_{1111}$ ,  $F_{2222}$ ,  $F_{1122}$  and  $F_{1212}$ . The failure condition then reads

$$F_{11}\sigma_{11} + F_{22}\sigma_{22} + F_{1111}\sigma_{11}^2 + F_{2222}\sigma_{22}^2 + 2F_{1122}\sigma_{11}\sigma_{22} + 4F_{1212}\sigma_{12}^2 - 1 = 0. \quad (3.63)$$

From uniaxial tension and compression experiments in the principal directions of the material symmetry (orthotropy),  $e_1$ -direction and  $e_2$ -direction, the following failure stresses can be measured (absolute values)

- $\sigma_{f1}^+$ : failure stress for uniaxial tension in  $e_1$ -direction
- $\sigma_{f1}^-$ : failure stress for uniaxial compression in  $e_1$ -direction
- $\sigma_{f2}^+$ : failure stress for uniaxial tension in  $e_2$ -direction
- $\sigma_{f2}^-$ : failure stress for uniaxial compression in  $e_2$ -direction

From these failure stresses, the parameters  $F_{11}$ ,  $F_{22}$ ,  $F_{1111}$ ,  $F_{2222}$  can be calculated via

$$F_{11} = \frac{1}{\sigma_{f1}^+} - \frac{1}{\sigma_{f1}^-}, \quad (3.64)$$

$$F_{22} = \frac{1}{\sigma_{f2}^+} - \frac{1}{\sigma_{f2}^-}, \quad (3.65)$$

$$F_{1111} = \frac{1}{\sigma_{f1}^+ \sigma_{f1}^-}, \quad (3.66)$$

$$F_{2222} = \frac{1}{\sigma_{f2}^+ \sigma_{f2}^-}. \quad (3.67)$$

From an equibiaxial experiment with  $\sigma_{11} = \sigma_{22}$  leading to failure at  $\sigma_{11} = \sigma_{22} = \sigma_{fb}$ , the parameter  $F_{1122}$  can be calculated via

$$F_{1122} = \frac{1}{2\sigma_{fb}^2}(1 - \sigma_{fb}(F_{11} + F_{22}) - \sigma_{fb}^2(F_{1111} + F_{2222})) \quad (3.68)$$

with the already known parameters  $F_{11}$ ,  $F_{22}$ ,  $F_{1111}$  and  $F_{2222}$ . Tsai and Hahn (1980) give an empirical estimation of  $F_{1122}$

$$F_{1122} = -\frac{1}{2}\sqrt{F_{1111}F_{2222}}. \quad (3.69)$$

From a pure shear experiment with failure at  $\sigma_{f12}$  the parameter  $F_{1212}$  can be derived

$$F_{1212} = \frac{1}{4\sigma_{f12}^2}. \quad (3.70)$$

Another possibility to derive the parameter  $F_{1212}$  is a uniaxial tension experiment in  $45^\circ$ -direction to the principal material symmetry axes with failure at  $\sigma_{f45}$ . Transforming the stress state into the principal coordinate system, leads to the following stress components at failure

$$\sigma_{11} = \sigma_{22} = \frac{1}{2}\sigma_{f45}, \quad \sigma_{12} = -\frac{1}{2}\sigma_{f45}. \quad (3.71)$$

Using this stress state and Equation (3.63),  $F_{1212}$  can be calculated

$$F_{1212} = \frac{1}{\sigma_{f45}^2}\left(1 - \frac{1}{2}\sigma_{f45}(F_{11} + F_{22}) - \frac{1}{4}\sigma_{f45}^2(F_{1111} + F_{2222} + 2F_{1122})\right). \quad (3.72)$$

## 3.4 Micromechanical Modeling of Failure

For micromechanical failure modeling, the general anisotropic case is considered again (without orthotropy assumption as for the macroscopic Tsai-Wu failure model). The Ansatz is chosen, that the Tsai-Wu strength tensors are linear in fiber orientation tensor. Thus, they have

the following form

$$\mathbb{F} = k_{f1}\mathbb{P}_1 + k_{f2}\mathbb{P}_2 + k_{f3}(\mathbf{D} \otimes \mathbf{I} + \mathbf{I} \otimes \mathbf{D}) + k_{f4}\mathbb{J}[\mathbf{D}] + k_{f5}\mathbb{D}, \quad (3.73)$$

$$\mathbf{F} = k_{f6}\mathbf{I} + k_{f7}\mathbf{D}, \quad (3.74)$$

with the two projectors as defined in Equation (3.53) and the operator  $\mathbb{J}$  as defined in Equation (3.54). This reduces the number of parameters from  $21+6=27$  to  $5+2=7$  for the fully anisotropic 3D case.

## Chapter 4

# Experimental Investigations

## 4.1 Experimental Facilities

### 4.1.1 Biaxial Testing Device

The electromechanical biaxial testing device is depicted in Fig. 4.1. It consists of four horizontally arranged independently controllable actuators. The force is measured by load cells with a maximum force of 150 kN. The strain/displacement of each of the four axes is measured by the displacement of the traverses and by an optical extensometer (Zwick VideoXtens). This system measures the displacement of five markers glued on the specimen and can calculate the strain for each axis. It is possible to control the experiments by the force or by the strain/displacement of the traverses or the strain measured by the VideoXtens system. The VideoXtens system can also be used for a midpoint control, which avoids undesirable transversal forces and bending loads. Uniaxial experiments can be performed using only two opposite axes.

Additionally, the strain field can be measured by digital image correlation system by GOM (ARAMIS 3D 4M). The system consists of two cameras which take high definition pictures of the specimen and a digital image correlation software.

DIC works by comparing digital photographs of a test piece at different

stages of deformation. The system can measure the surface displacement and build up full field 2D and 3D deformation vector fields and strain maps (McCormick and Lord, 2010). A match point is searched on each picture. As it is almost impossible to find a match point by one single pixel an area with multiple pixels, called facet, is used to perform the matching process. The strain is calculated via the displacement of these facets. For DIC to work effectively, the pixel blocks need to be random and unique with a range of contrast and different intensity levels (Yoneyama and Murasawa, 2000). Accordingly, a grey scale patterns is applied by spraying paint onto the specimen as shown in Figure 4.2.

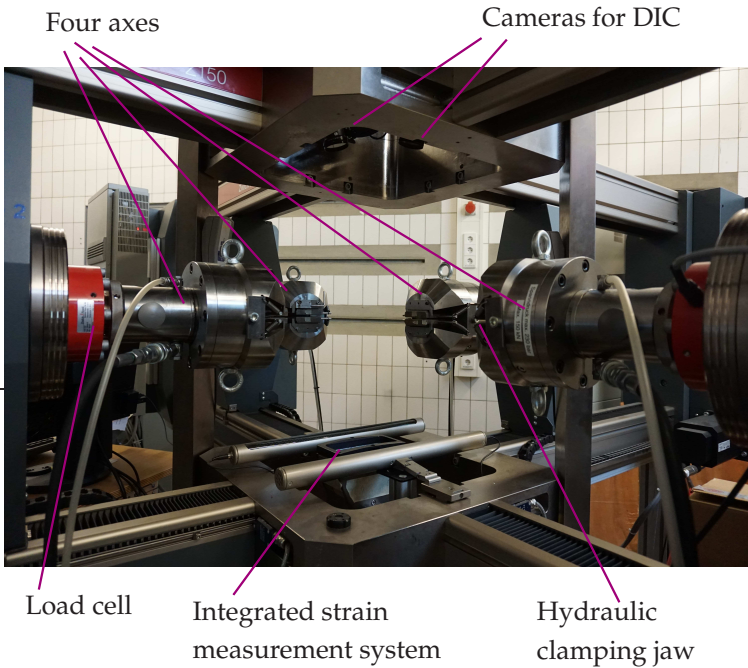


Figure 4.1: Biaxial testing device.



Figure 4.2: Grey scale pattern.

### 4.1.2 Dynamical Mechanical Analysis

The DMA (Dynamical Mechanical Analysis) or Dynamical Mechanical Thermo Analysis (DMTA) method can be used to determine thermo-viscoelastic properties of a material (Grellmann and Seidler, 2011). The specimen is subjected to a periodically (mostly sinusoidal) changing load of constant frequency and amplitude. The temporal change of stress and strain have the same frequency but different phase angles as described in Section 2.4. Via the measuring of force or path (with given specimen dimensions) and phase shift, storage modulus, loss modulus and loss factor can be evaluated using the equations in Section 2.4.

The testing device GABO Eplexor<sup>®</sup> 500N as shown in Figure 4.3a is used for the experiments in this thesis. The experiments can be performed in a temperature range from  $-150^{\circ}\text{C}$  to  $500^{\circ}\text{C}$  and a frequency range from 0.01 Hz to 100 Hz. The maximum static load is 1500 N, the maximum dynamic load is 500 N (depending on the load cell), the maximum static displacement is 35 mm, and the maximum dynamic displacement is

1.5 mm. The measurements can be either stress or strain controlled. Depending on the testing procedure, the following parameters can be set and controlled: static load, dynamic load, static strain, dynamic strain, frequency and temperature, and the so-called contact force, which is used to measure the initial length and to tighten the specimen in tensile tests and to ensure that the specimen rests in the holder in compression tests.

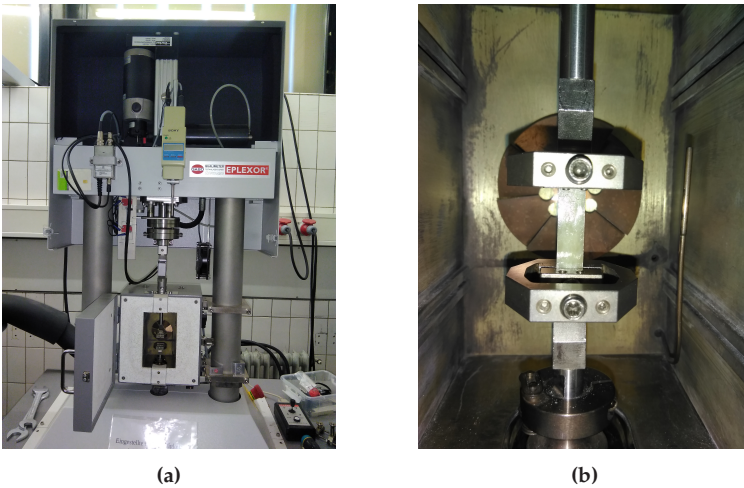


**Figure 4.3:** DMA testing device. (a) Photograph DMA, (b) Detail of (a).

The principle functioning is as follows. After the contact force is applied, the static load is adjusted by varying (lengthening or shortening) the static load unit. The lower force axis via a leaf spring forms the counterforce. The electrodynamic drive (shaker) generates a dynamically oscillating force on the specimen. The dynamic counterforce is also recorded directly by the force transducer. The analog signals recorded by the force transducer and dynamic displacement measuring system

further processed and evaluated in the process computer. The desired measurement results are then calculated using the amplitudes of the force and displacement signals and the phase shift. With the help of the software, various testing procedures can be set, e.g. timesweep, temperature sweep and frequency sweep. In timesweep all parameters are kept constant and several measurements are performed under the same conditions, in temperature and frequency sweep the temperature and the frequency are varied respectively (Gabo, 2010).

### 4.1.3 Dilatometer

Dilatometry (DIL) is a technique that measures a dimensional change (the length or volume) of a material under negligible stress as a function of temperature. The Dilatometer used in this work is a pushrod dilatometer DIL 402 *Expedis Classic*<sup>®</sup> from NETZSCH Gerätebau GmbH. The specimen length is measured under temperature control in an oven by a sensitive sensor system under a very small clamping force of 0.2 N. The thermal expansion coefficient can then be computed as  $\Delta l(\theta)/\Delta \theta$  (with the length  $l$  of the specimen and the temperature  $\theta$ ) between each measuring point. High measuring rates allow for an almost continuous measurement of the thermal expansion. Due to the very sensitive measuring sensors, small fluctuations due to vibrations of environmental influences lead to measurement noise. Therefore a mean filter is applied to the direct experimental data. To determine the magnitude of the mean filter, a Fourier analysis was applied to the experimental data. The temperature range of the dilatometer is from  $-100^{\circ}\text{C}$  to  $1000^{\circ}\text{C}$ , enabled by nitrogen cooling and a heating oven. Suitable specimens have a length of best 30 mm to 50 mm. Accuracies of up to 0.003 % in strain (absolute value) and 1 K in temperature are possible. Figure 4.4 show photographs of the dilatometer, with the whole testing device in Figure 4.4a and a detailed view of the specimen holder, pushrod and specimen in Figure 4.4b.

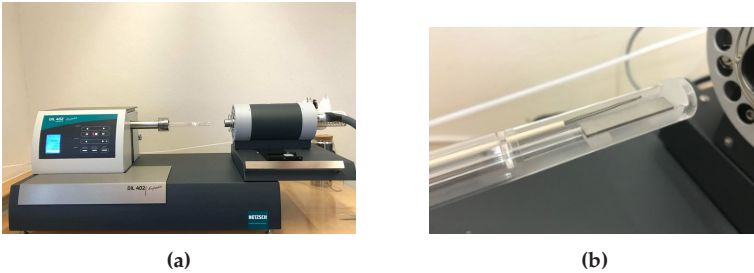


**Figure 4.4:** Dilatometer. (a) Photograph dilatometer, (b) Detail of (a).

### 4.1.4 Laser Flash Analysis

With laser flash method (LFA) thermal diffusivity, heat capacity and thermal conductivity can be determined. The quantity that is directly measured is the thermal diffusivity. Figure 4.5 shows the principle functioning. A flat specimen is placed in a chamber with temperature control. One side of this specimen is subjected a short energy pulse. On the other side temperature over time is detected. From this temperature course, thermal diffusivity can be determined. Using a reference specimen with known heat capacity, also the heat capacity of the measured specimen can be determined. Combining these two material parameters with the mass density, also thermal conductivity can be calculated (NETZSCH, 2021). Details on the basics of LFA method can be found in Parker et al. (1961), who described first this measuring method. Information on nowadays standard laser flash methods can be found in Johra (2019), Cape and Lehman (1963) and Cowan (1963).

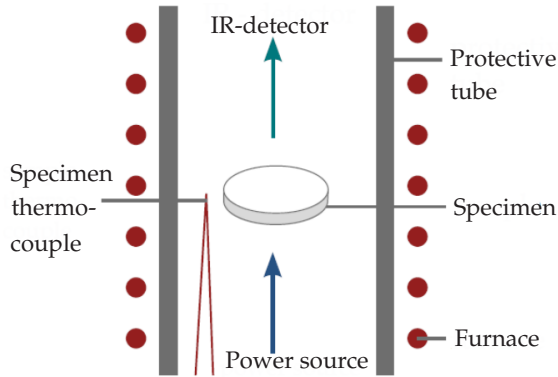


Figure 4.5: LFA technique (according to NETZSCH (2021)).

The laser flash apparatus used in this theses is a NETZSCH LFA *Hyperflash* 467<sup>®</sup>. A photograph of the testing device is shown in Figure 4.6. The temperature range of the measurements is from  $-100^{\circ}\text{C}$  to  $500^{\circ}\text{C}$  using a furnace and liquid nitrogen cooling. The measuring range for thermal diffusivity is  $0.01\text{ mm}^2/\text{s}$  to  $2000\text{ mm}^2/\text{s}$  and for thermal conductivity  $0.1\text{ W}/(\text{mK})$  to  $4000\text{ W}/(\text{mK})$



Figure 4.6: Photograph LFA ( NETZSCH (2021)).

## 4.2 Specimens

Specimens considered in this thesis were extracted from the plates mainly using water-jet cutting for the SMC specimens, partly combined with a milling or sawing treatment. The pure resin specimens were cut by gentle milling. Figures 4.7 to 4.12 show the different specimen geometries. Figure 4.7 shows a bone specimen. This specimen can be used in the biaxial testing device (in uniaxial use). In this work it is used for damage experiments and failure experiments. The rectangular area marked in violet, the area of interest ( $A^I$ ) is used for the calculation of the area-averaged strains by the DIC

$$\bar{\varepsilon}_{ij}^I = \frac{1}{A^I} \int_{A^I} \varepsilon_{ij} dA^I. \quad (4.1)$$

Figure 4.8 shows a biaxial cruciform specimen. The special design of this specimen is presented in Section 4.5.1. This specimen is used in the biaxial testing device for damage and failure experiments. The violet marked square is the area of interest. The area-averaged strain over this area is defined as in Equation (4.1).

The rectangular specimen in Figure 4.9 can be used in the DMA, and as small specimen in the biaxial testing device. Stiffness and failure experiments are conducted with this specimen geometry. The specimen of Figure 4.10a fits into the DMA, the dilatometer, and also the biaxial testing device. Figure 4.10b show a specimen that is suitable for dilatometer and DMA. The small square shaped specimen of Figure 4.11 is used for the LFA experiments. Figure 4.12 shows a specimen that is used for a shear experiment in the biaxial testing device. Reference is made to the specimen geometries shown here at the appropriate places in the text.

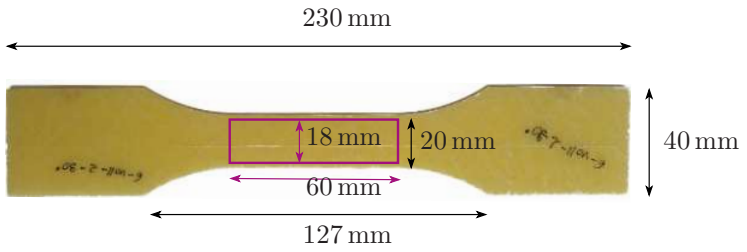
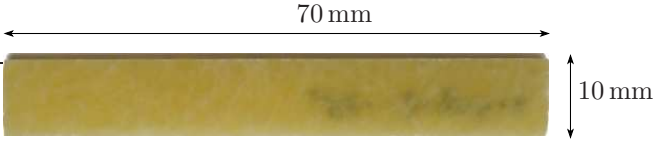


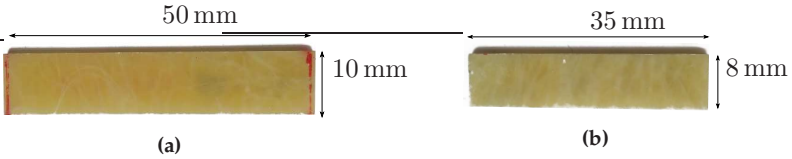
Figure 4.7: Bone specimen; use in: biaxial testing device.



Figure 4.8: Biaxial specimen; use in: biaxial testing device, for details see Section 4.5.1.



**Figure 4.9:** Rectangular specimen; use in: DMA and as "small" specimen in biaxial testing device.



**Figure 4.10:** Rectangular specimens, use in: dilatometer, DMA, biaxial testing device.

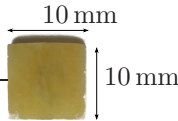


**Figure 4.11:** Quadratic specimen; use in: LFA.

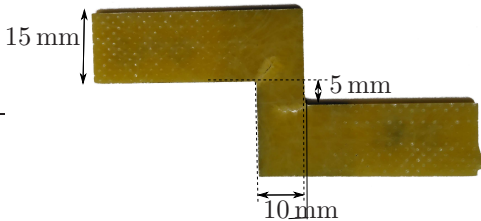


**Figure 4.12:** Shear specimen; use in: biaxial testing device.

## 4.3 Thermoelastic Material Parameters

### 4.3.1 Introducing Remarks and Data Evaluation

In the following sections, the results of the experimental investigations of the thermoelastic material behavior is presented. The considered material parameters are Young's modulus, Poisson's ratio, thermal expansion coefficient, thermal diffusivity, thermal conductivity, and heat capacity. Those which belong to the tensorial material coefficients (see Section 3.1) are evaluated in special directions (the exact relation between the measured material parameters and the material coefficients of the material model is explained in the parameter identification chapter (see Section 5.1)). All of them, except Poisson's ratio (because only measurable with the biaxial testing device without temperature control), are measured in dependence of temperature. The temperature range considered for this purpose is  $-10^{\circ}\text{C}$  to  $80^{\circ}\text{C}$ .

For each individual material parameter  $\xi(\theta)$  ( $\xi$  denotes an any material parameter in the following) a value for the room temperature (RT) range is calculated. It is an average of all values taken between  $10^{\circ}\text{C}$  and  $30^{\circ}\text{C}$  and referred to as  $\xi_{\text{RT}}$ . This introduces a kind of mean filter avoiding that variations exactly around  $20^{\circ}\text{C}$  influence the value significantly. Which values exactly are taken for this is explained at the corresponding point. Regarding the biaxial testing device, the values are taken here at the current temperature in the laboratory (which can vary between  $15^{\circ}\text{C}$  and  $25^{\circ}\text{C}$ ), as it has no temperature control.

For each temperature and each parameter, measurements with several specimens are taken. Statistical values (mean, standard deviation (std), coefficient of variation (CV)) are calculated for the above mentioned RT value  $\xi_{\text{RT}}$  according to Appendix A.3. Also the used boxplot representation is elucidated in this appendix Section (Appendix A.3.2). To evaluate the pronouncedness of the temperature dependence, the relative difference between the value of a material parameter at  $-10^{\circ}\text{C}$

and 80°C is introduced as

$$\Delta\xi_{\text{rel,RT}} = \frac{\xi(\theta = 80^\circ\text{C}) - \xi(\theta = -10^\circ\text{C})}{\xi_{\text{RT}}}. \quad (4.2)$$

Here,  $\xi(\theta = -10^\circ\text{C})$  and  $\xi(\theta = 80^\circ\text{C})$  are the values of the material parameter  $\xi(\theta)$  at  $-10^\circ\text{C}$  and  $80^\circ\text{C}$ . The difference is normalized to the above mentioned RT value  $\xi_{\text{RT}}$  for comparability.

For all thermoelastic material parameters, specimens from SMC flow plates (see Figure 2.4) and from pure resin were considered. Depending on the parameter and the experimental method requiring a certain specimen geometry, the measuring direction differs. Thus, stiffness and thermal expansion coefficient are measured in different directions in the  $0^\circ$ - $90^\circ$ -plane (see Figure 2.4) and thermal diffusivity and thermal conductivity in the direction perpendicular to this  $0^\circ$ - $90^\circ$ -plane. The latter can be described as the plate thickness direction. For the parameters measured in the  $0^\circ$ - $90^\circ$ -plane, the anisotropy ratio  $\Gamma_{0/90}$  is defined as

$$\Gamma_{0/90} = \frac{\xi_{0^\circ}}{\xi_{90^\circ}}, \quad (4.3)$$

with the value of the parameter  $\xi_{0^\circ}$  measured in  $0^\circ$ -direction and  $\xi_{90^\circ}$  measured in  $90^\circ$ -direction at RT. Furthermore, the ratio of the values of the parameters of the reinforced material to these of the unreinforced material is introduced as

$$\Gamma_{\text{SMC/PR}} = \frac{\xi_{\text{SMC}}}{\xi_{\text{PR}}}, \quad (4.4)$$

with the value of the parameter for SMC  $\xi_{\text{SMC}}$  (in different then indicated measuring directions) and for pure resin  $\xi_{\text{PR}}$  at RT.

Preliminary studies were performed to investigate the reproducibility of the experimental results and possible influences of specimen conditioning. As a result, all specimens are conditioned at  $100^\circ\text{C}$  for 1 h to enhance the reproducibility. As an example, the results of a preliminary

study with the dilatometer, in which one specimen was tested several times under different conditions, can be found in Appendix A.2.

### 4.3.2 Stiffness

As stiffness parameters Young's modulus and Poisson's ratio are considered. The biaxial testing device is used for values at room temperature for Young's modulus and Poisson's ratio. Here, stiffness is determined using the displacement of the axes and the force. Poisson's ratio is determined within the scope of measurement accuracy (see Section 4.5.2) by DIC. Additionally, for some specimens DMA experiments for temperature-dependent Young's modulus are performed with assuming that storage modulus is equal to Young's modulus here (see Kehrler (2019)). For selected specimens Young's modulus was determined by DMA and biaxial testing device. The relative difference was below 3%. As specimen shapes the small rectangular ones of Figure 4.9 and Figure 4.10a are used. These specimens fit into both testing device.

Figure 4.13 shows the Young's modulus over temperature for several specimens. The markers of the measuring points are connected by straight lines to indicate the course. The trend is significantly decreasing for the pure resin material and both SMC directions for all specimens. The curves of the two pure resin samples are almost identical. In 0°- and 90°-directions the curves of the individual specimens differ significantly, respectively. Tables 4.1 and 4.2 depict mean value, standard deviation (std), and coefficient of variation (CV) as measure for the scattering for Young's modulus and Poisson's ratio at room temperature for the different SMC specimen directions and the pure resin material. For Young's modulus and Poisson's ratio, the CV for SMC is approximately 10% in all directions, whereas the CV of Young's modulus of pure resin is approximately 2%. Figure 4.14 illustrates the statistical considerations via a boxplot representation for Young's

modulus of the SMC material in  $0^\circ$ - and  $90^\circ$ -direction. Details on statistical analysis can be found in Appendix A.3.

The comparison of the values of the pure resin and SMC in  $0^\circ$ - and  $90^\circ$ -direction leads to an anisotropy ratio of  $\Gamma_{0/90} = 1.36$  and a ratio of reinforcement of  $\Gamma_{\text{SMC-0/PR}} = 4.06$  (see Equations (4.3) and (4.4)). Table 4.3 shows the Young's modulus at the edges of the considered temperature range and the relative difference  $\Delta E_{\text{rel,RT}}$  (see Equation (4.2)).  $E(\theta = -10^\circ\text{C})$  and  $E(\theta = 80^\circ\text{C})$  are the mean values over all specimens, respectively. The scattering measures are similar to those for the RT values. For the pure resin material the difference is approximately 27 %, for the SMC specimens it is less half of this value with approximately 10 % with slightly more in  $90^\circ$ -direction and slightly less in  $0^\circ$ -direction.

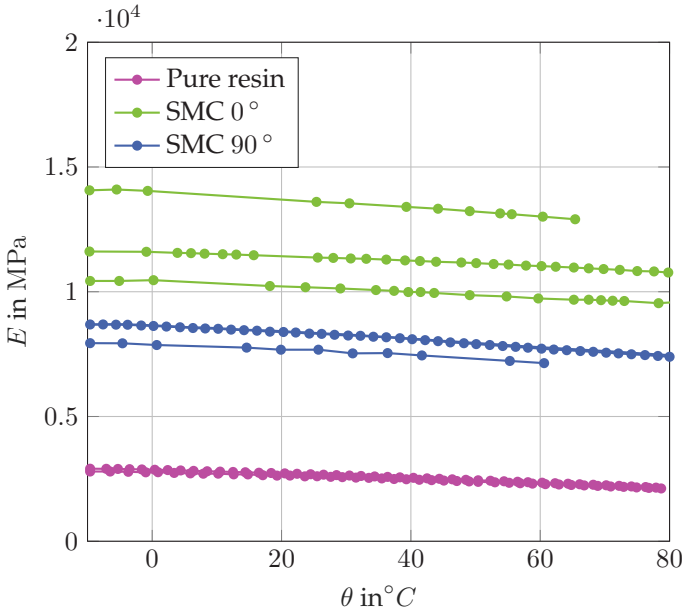


**Figure 4.13:** Young's modulus  $E(\theta)$  of pure resin (2 specimens) and SMC in  $0^\circ$ -direction (3 specimens), and  $90^\circ$ -direction (3 specimens) over temperature  $\theta$ .

	no of spec.	Mean in MPa	Std in MPa	CV in %
Pure resin	2	2660	56	2.13
SMC 0°	8	10801	1079	9.99
SMC 90°	7	7967	711	8.92
SMC 45°	6	9050	927	10.24

**Table 4.1:** Young's modulus at room temperature  $E_{RT}$  for pure resin and SMC in 0°, 90° - and 45°-direction; mean, standard deviation (std) and coefficient of variation (CV) for indicated number of specimens (no of spec.)(Calculation as per Appendix A.3).

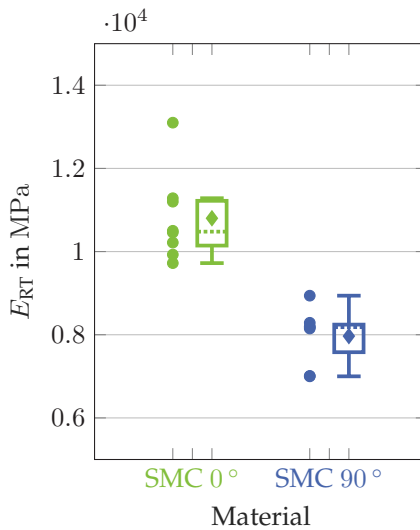


**Figure 4.14:** Young's modulus at RT  $E_{RT}$  of SMC in 0°-direction (8 specimens) and 90°-direction (7 specimens) determined by experiments with biaxial testing device and DMA: boxplot representation (for explanation see Appedix A.3.2).

	no of spec.	Mean in -	Std in -	CV in %
SMC 0°	5	0.367	0.0213	5.8
SMC 90°	4	0.272	0.0258	9.4
SMC 45°	3	0.301	0.0340	11.3

**Table 4.2:** Poisson's ratio at room temperature  $\nu_{RT}$  for SMC in 0°, 90°, and 45°-direction ; mean, standard deviation (std) and coefficient of variation (CV) for indicated number of specimens (no of spec.) (Calculation as per Appendix A.3).

	$E(\theta = -10^\circ\text{C})$ in MPa	$E(\theta = 80^\circ\text{C})$ in MPa	$\Delta E_{rel,RT}$ in %
Pure resin	2851	2132	-27.0
SMC 0°	11022	10170	-7.9
SMC 90°	8687	7422	-15.0

**Table 4.3:** Young's modulus  $E$  at  $\theta = -10^\circ\text{C}$  and  $\theta = 80^\circ\text{C}$  (mean values over all (in the full temperature range) tested specimens respectively) and normalized difference  $\Delta\alpha_{rel,RT}$  (see Equation (4.2)) for pure resin and SMC in 0°- and 90°- direction.

### 4.3.3 Thermal Expansion

Using the dilatometer presented in Section 4.1.3, the thermal expansion in dependence on temperature was experimentally determined. The considered temperature range was tested with a heating rate of 2 K/min and a small measuring step width of 0.1 K.

The experiments were performed with several specimens in 0°-direction (5 specimens), 90°-direction (5 specimens), 45°-direction (1 specimen) and pure resin (2 specimens) of the specimen shapes shown in Figures 4.10a and 4.10b.

Figure 4.15 shows the thermal expansion coefficient over temperature

for several specimens. The trend is significantly increasing for the pure resin material, with an increasing slope. For the  $90^\circ$  specimens the trend is only slightly increasing and for  $0^\circ$  it is almost constant. The curves of the two pure resin samples are almost identical. In  $0^\circ$ - and  $90^\circ$ -directions the trend is the same respectively but scattering is visible. Table 4.4 depicts mean value, standard deviation (std), and coefficient of variation (CV) as measure for the scattering for the thermal expansion coefficient at room temperature for the different SMC specimen directions and the pure resin material (there are more specimens than in the diagram (Figure 4.15) because not all specimens were tested in the full temperature range). The room temperature values  $\alpha_{RT}$  for the individual specimens are here calculated as the mean of all values between  $10^\circ\text{C}$  and  $30^\circ\text{C}$ . The higher scattering of the SMC specimens is here shown by the CV of approximately 10 % in both directions, whereas the CV of pure resin is below 1 %. Figure 4.16 illustrates the statistical considerations via a boxplot representation for the SMC material in  $0^\circ$ - and  $90^\circ$ -direction. Details on statistical analysis can be found in Appendix A.3.

The comparison of the values of the pure resin and SMC in  $0^\circ$ - and  $90^\circ$ -direction leads to an anisotropy ratio of  $\Gamma_{0/90} = 0.70$  and a ratio of reinforcement of  $\Gamma_{SMC-0/PR} = 0.23$  (see Equations (4.3) and (4.4)). Table 4.5 shows the thermal expansion coefficient at the edges of the considered temperature range and the relative difference  $\Delta a_{rel,RT}$  (see Equation (4.2)). Here,  $a(\theta = -10^\circ\text{C})$  and  $a(\theta = 80^\circ\text{C})$  are the mean values over all specimens, respectively, with scattering measures similar to those for RT. For the pure resin material the difference is pronounced with approximately 35 %, for SMC in  $90^\circ$ -direction the difference is approximately 10 % and for SMC in  $0^\circ$ -direction the very small value implies a almost constant behavior.

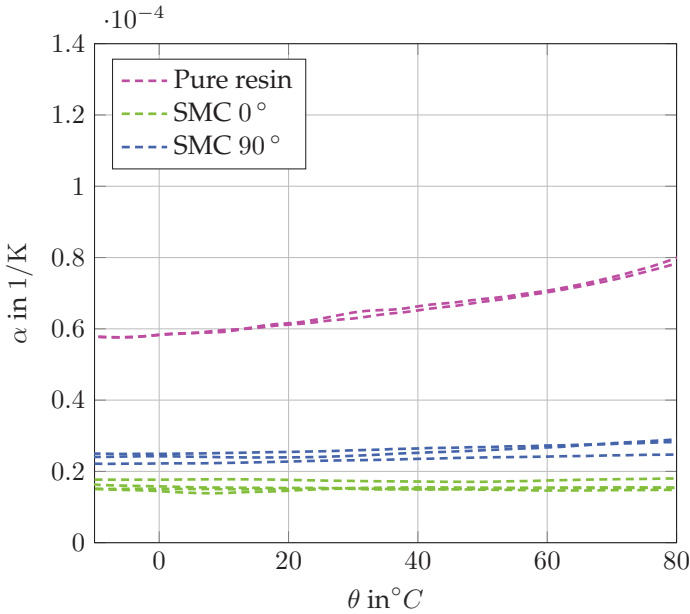


**Figure 4.15:** Thermal expansion coefficient  $\alpha(\theta)$  of pure resin (2 specimens) and SMC in  $0^{\circ}$ -direction (3 specimens), and  $90^{\circ}$ -direction (3 specimens) over temperature  $\theta$ .

	no of spec.	Mean in $1/K \cdot 10^{-5}$	Std in $1/K \cdot 10^{-5}$	CV in %
Pure resin	2	6.13	0.247	0.40
SMC $0^{\circ}$	5	1.61	0.154	9.61
SMC $90^{\circ}$	5	2.30	0.208	9.04
SMC $45^{\circ}$	1	2.00	/	/

**Table 4.4:** Thermal expansion coefficient at RT  $\alpha_{RT}$  for pure resin and SMC in  $0^{\circ}$ -,  $90^{\circ}$ -, and  $45^{\circ}$ -direction; mean, standard deviation (std) and coefficient of variation (CV) (Calculation as per Appendix A.3).

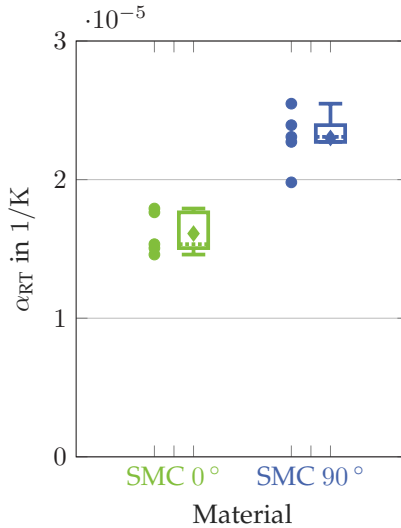


**Figure 4.16:** Thermal expansion coefficient at RT  $\alpha_{RT}$  of SMC in  $0^\circ$ -direction (5 specimens) and  $90^\circ$ -direction (5 specimens) determined by DIL experiments: boxplot representation (for explanation see Appendix A.3.2).

	$\alpha(\theta = -10^\circ\text{C})$ in $1/\text{K} \cdot 10^{-5}$	$\alpha(\theta = 80^\circ\text{C})$ in $1/\text{K} \cdot 10^{-5}$	$\Delta\alpha_{\text{rel,RT}}$ in %
Pure resin	5.77	7.87	34.20
SMC $0^\circ$	1.62	1.60	-0.55
SMC $90^\circ$	2.34	2.57	9.95

**Table 4.5:** Thermal expansion coefficient  $\alpha$  at  $\theta = -10^\circ\text{C}$  and  $\theta = 80^\circ\text{C}$  (mean values over all tested specimens respectively) and normalized difference  $\Delta\alpha_{\text{rel,RT}}$  (see Equation (4.2)) for pure resin and SMC in  $0^\circ$ - and  $90^\circ$ - direction.

### 4.3.4 Thermal Diffusivity

The thermal diffusivity is introduced as an additional material coefficient to the coefficients discussed in Section 3.1, since thermal

diffusivity is directly determined via the LFA method (see Section 4.1.4). The thermal diffusivity  $a$  is defined via the heat capacity  $c_p$ , the thermal conductivity  $\kappa$ , and the mass density  $\rho$  (Salazar (2003), Johra (2019))

$$a(\theta) = \frac{\kappa(\theta)}{\rho c_p(\theta)}. \quad (4.5)$$

The LFA experiments for determining thermal diffusivity described in the following are also used for the determination of the heat capacity and the thermal conductivity (Sections 4.3.5 and 4.3.6). In total, 3 pure resin and 8 SMC specimens were tested in the considered temperature range of  $-10^\circ\text{C}$  to  $80^\circ\text{C}$  with a step width of  $10^\circ\text{C}$ . Due to the for the testing device required specimen shape (see Section 4.2 and Section 4.1.4), the measurements can only be performed in the plate thickness direction, i.e. perpendicular to the  $0^\circ$ - $90^\circ$ -plane (see Figure 2.4). The experimental data is partly taken from Wehrle (2020). Figure 4.17 depicts the results for all tested pure resin and SMC specimens. Every specimen was tested four times, and the averages of these four measurements are taken for the diagram. The diagram (Figure 4.17) shows the thermal diffusivity over temperature. The markers are located at the measurement points. They are connected by straight lines to indicate the course. Both curves have a decreasing trend. The thermal diffusivity of SMC is higher than that of the pure resin for all temperatures, whereas SMC curves scatter more than the pure resin curves. Table 4.6 depicts the mean values, standard deviations (std) and coefficient of variation (CV) at room temperature for pure resin (calculated over the 3 measured specimens) and SMC (calculated over the 8 measured specimens). The room temperature values for the individual specimens are here calculated as the mean of the three values (at  $10^\circ\text{C}$ ,  $20^\circ\text{C}$ ,  $30^\circ\text{C}$ ). It can be noticed that the mean value for the thermal diffusivity at room temperature for SMC is about 1.2 times greater than the one for the pure resin ( $\Gamma_{\text{SMC/PR}} = 1.2$ ,

see Equation (4.4)). Figure 4.18 illustrates the statistical considerations via a boxplot representation. Table 4.6 and Figure 4.18 elucidate the higher scattering for SMC and the low scattering for the pure resin. Here must be taken into account that the number of specimens is very small for the pure resin. Details on statistical analysis can be found in Appendix A.3. With Table 4.7 the temperature dependence can be analysed and compared. It shows the values of the thermal diffusivity at the edges of the considered temperature range ( $a(\theta = -10^\circ\text{C})$  and  $a(\theta = 80^\circ\text{C})$ , mean values over all specimens, respectively, with standard deviation and CV similar to the values at RT) and the relative difference  $\Delta a_{\text{rel,RT}}$  (see Equation (4.2)). For both materials the normalized difference of the thermal diffusivity is around 20%, whereas for the pure resin the value is slightly greater than for SMC.

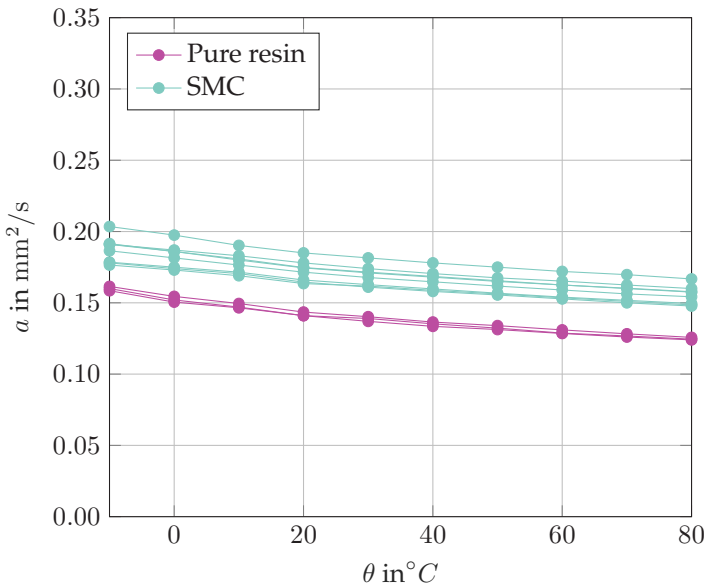


**Figure 4.17:** Thermal diffusivity  $a(\theta)$  of pure resin (3 specimens) and SMC (8 specimens) over temperature  $\theta$  (measured in plate thickness direction by LFA experiments).

	no of spec.	Mean in $\text{mm}^2/\text{s}$	Std in $\text{mm}^2/\text{s}$	CV in %
Pure resin	3	0.143	0.00146	1.02
SMC	8	0.172	0.00714	4.79

**Table 4.6:** Thermal diffusivity  $a_{RT}$  at RT for pure resin and SMC (measured in plate thickness direction by LFA experiments); mean, standard deviation (std) and coefficient of variation (CV) of the indicated number of specimens (no of spec.) (Calculation as per Appendix A.3).

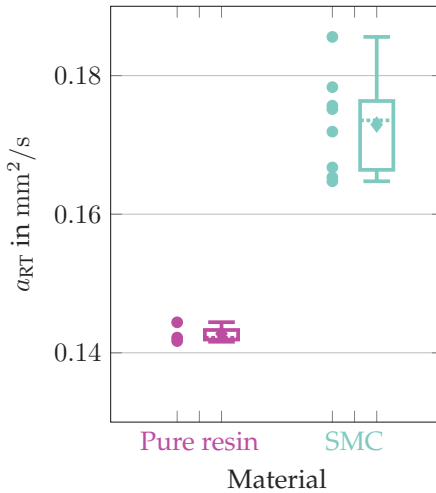


**Figure 4.18:** Thermal diffusivity  $a_{RT}$  at RT of pure resin (3 specimens) and SMC (8 specimens) determined by LFA experiments (in plate thickness direction): boxplot representation (for explanation see Appendix A.3.2).

	$a(\theta = -10^\circ\text{C})$ in $\text{mm}^2/\text{s}$	$a(\theta = 80^\circ\text{C})$ in $\text{mm}^2/\text{s}$	$\Delta a_{\text{rel,RT}}$ in %
Pure resin	0.160	0.125	-24.5
SMC	0.187	0.155	-18.5

**Table 4.7:** Thermal diffusivity  $a$  at  $\theta = -10^\circ\text{C}$  and  $\theta = 80^\circ\text{C}$  and normalized difference  $\Delta a_{\text{rel,RT}}$  (see Equation (4.2)) for pure resin and SMC (mean values over all tested specimens resp.; measured in plate thickness direction by LFA experiments).

### 4.3.5 Heat Capacity

The heat capacity was determined via the LFA experiments for the thermal diffusivity described in Section 4.3.4. The test procedure, number of specimens and experiments, and data evaluation are therefore the same as for the thermal diffusivity measurements in Section 4.3.4. The measurement accuracy and reproducibility of the LFA method is less for heat capacity than for diffusivity. Therefore, it is even more important that several measurements of a specimen are performed. Statistical evaluation has shown that the scatter between different measurements of one specimen is of a similar order of magnitude as the scatter between different specimens. However, the value averaged from several measurements approximates the actual value with sufficient accuracy. Studies on this can be found in Wehrle (2020).

The diagram of Figure 4.19 shows the heat capacity over temperature for all of the 3 pure resin and 8 SMC specimens. As for the diffusivity temperature diagram the markers of the measuring points are connected by straight lines to indicate the course. The pure resin curve is above the SMC curve. Both curves have increasing trend, with the slope being larger for pure resin. Slight scattering is visible for both materials. Table 4.8 shows the mean values, standard deviations (std) and coefficients of variation (CV) at room temperature for pure resin (calculated over the 3 measured specimens) and SMC (calculated

over the 8 measured specimens). The room temperature values for the individual specimens are here the mean of the values at 10°C and 30°C (faulty measuring value at 20°C). The mean value for the heat capacity at room temperature for SMC is about 0.75 of the one for the pure resin ( $\Gamma_{\text{SMC/PR}} = 0.75$ , see Equation (4.4)). Figure 4.20 visualizes the statistical considerations with a boxplot. The relatively small scatter of maximum 3% for pure resin and for SMC can be seen in Table 4.8 and Figure 4.20. Here, the scatter of the pure resin values is greater than that of the SMC values. It should be noted here that the measurement inaccuracy for heat capacity of the testing device can also be the cause of the scatter. Details on statistical analysis can be found in Appendix A.3. With Table 4.9 the temperature dependence can be analysed and compared. It shows the values of the thermal diffusivity at the edges of the considered temperature range ( $c_p(\theta = -10^\circ\text{C})$  and  $c_p(\theta = 80^\circ\text{C})$ , mean values over all specimens respectively, with std and CV similar to the values at RT) and the relative difference  $\Delta c_{p,\text{rel,RT}}$  (see Equation (4.2)). The temperature dependence of the heat capacity is clearly present for both materials, whereby it is more pronounced for the pure resin.

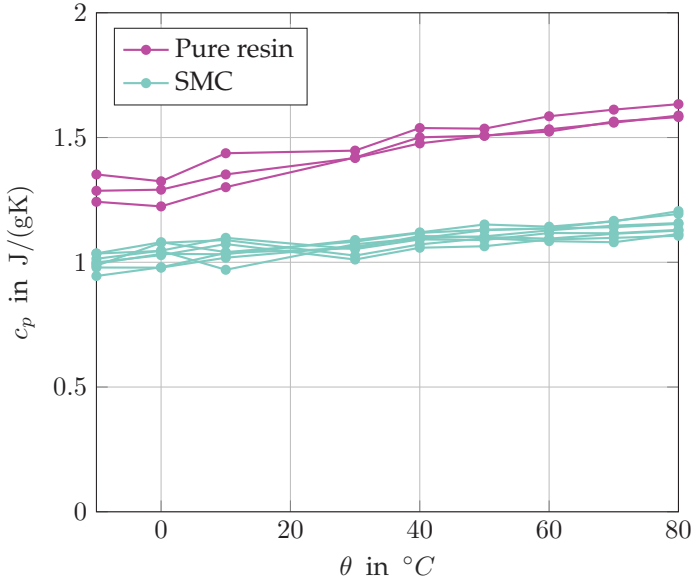


**Figure 4.19:** Heat capacity  $c_p(\theta)$  of pure resin (3 specimens) and SMC (8 specimens) over temperature  $\theta$  (determined by LFA experiments).

	no of spec.	Mean in $\text{J}/\text{gK}$	Std in $\text{J}/\text{gK}$	CV in %
Pure resin	3	1.40	0.0420	3.01
SMC	8	1.06	0.0135	1.28

**Table 4.8:** Heat capacity  $c_{p,RT}$  at RT for pure resin and SMC (determined by LFA experiments); mean, standard deviation (std) and coefficient of variation (CV) of the indicated number of specimens (no of spec.) (calculation as per Appendix A.3).

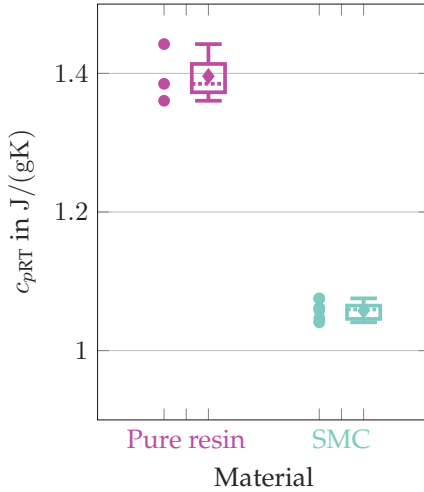


**Figure 4.20:** Heat capacity  $c_{pRT}$  at RT of pure resin (3 specimens) and SMC (8 specimens) determined by LFA experiments: boxplot representation (for explanation see Appendix A.3.2).

	$c_p(\theta = -10^\circ\text{C})$ in J/(gK)	$c_p(\theta = 80^\circ\text{C})$ in J/(gK)	$\Delta c_{p,rel,RT}$ in %
Pure resin	1.29	1.60	22.0
SMC	1.00	1.16	14.8

**Table 4.9:** Heat capacity  $c_p$  at  $\theta = -10^\circ\text{C}$  and  $\theta = 80^\circ\text{C}$  and normalized difference  $\Delta c_{p,rel,RT}$  (see Equation (4.2)) for pure resin and SMC (mean values over all tested specimens; measured by LFA experiments).

### 4.3.6 Thermal Conductivity

The LFA experiments for the thermal diffusivity described in Section 4.3.4 serve also to determine the thermal conductivity. There-

fore the relation of Equation (5.26) is used with the values for thermal diffusivity and heat capacity of the two previous sections and the mass density taken from Trauth (2018) ( $\rho_{\text{SMC}} = 1.53 \text{ g/cm}^3$  and  $\rho_{\text{PR}} = 1.14 \text{ g/cm}^3$ ). The same remarks regarding measurement accuracy and reproducibility apply to thermal conductivity as to heat capacity. Figure 4.21 shows the thermal conductivity over temperature for all of the three pure resin and eight SMC specimens. Again, the markers of the measuring points are connected by straight lines to indicate the course. The pure resin curve is below the SMC curve. Both curves indicate a nearly constant behavior of the thermal conductivity. Scattering for SMC is more pronounced than for pure resin. In Table 4.10 the statistical quantities (mean value, standard deviation (std) and coefficient of variation (CV)) at room temperature (RT) can be found for pure resin (calculated over the 3 measured specimens) and SMC (calculated over the 8 measured specimens). The RT values for the individual specimens are here the mean of the values at  $10^\circ\text{C}$  and  $30^\circ\text{C}$ , corresponding to the available values for heat capacity. The ratio of thermal conductivity at room temperature for SMC and pure resin is about  $\Gamma_{\text{SMC/PR}} = 1.2$  (see Equation (4.4)). A visualization of the statistical considerations is given in Figure 4.20 with a boxplot. The CV for both materials is below 5% and for pure resin slightly below SMC. Details on statistical analysis can be found in Appendix A.3. The temperature dependence is analysed in Table 4.11. It depicts the values of the thermal diffusivity at the edges of the considered temperature range ( $\kappa(\theta = -10^\circ\text{C})$  and  $\kappa(\theta = 80^\circ\text{C})$ , mean values over all specimens respectively, with std and CV similar to the values at RT) and the relative difference  $\Delta\kappa_{\text{rel,RT}}$  (see Equation (4.2)). The relative difference is below 5% for both materials, which confirms the nearly constant behavior. From Figure 4.21 can be seen that there are more pronounced fluctuations at low temperatures which influence that value; measuring inaccuracies may here influence the values.

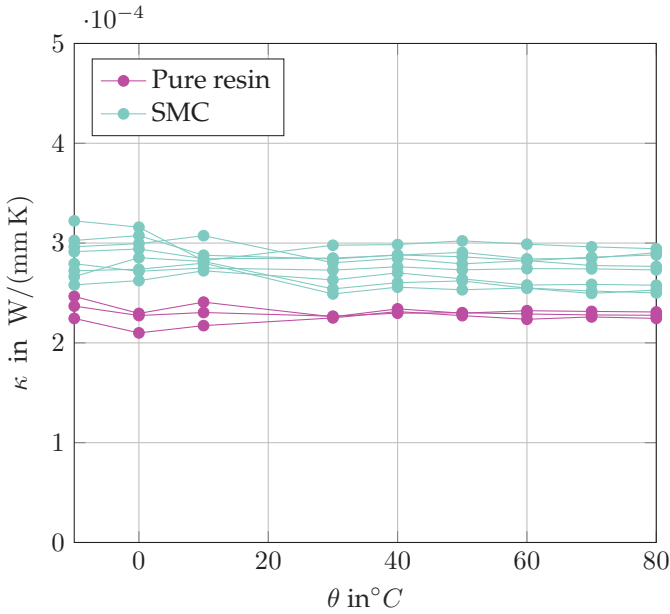


**Figure 4.21:** Thermal conductivity  $\kappa(\theta)$  of pure resin (3 specimens) and SMC (8 specimens) over temperature  $\theta$  (determined in plate thickness direction by LFA experiments).

	no of spec.	Mean in $W/(mm K)$	Std in $W/(mm K)$	CV in %
Pure resin	3	$2.27 \cdot 10^{-4}$	$0.062 \cdot 10^{-4}$	2.72
SMC	8	$2.79 \cdot 10^{-4}$	$0.114 \cdot 10^{-4}$	4.10

**Table 4.10:** Thermal conductivity  $\kappa_{RT}$  at RT for pure resin and SMC (determined in plate thickness direction by LFA experiments); mean, standard deviation (std) and coefficient of variation (CV) of the indicated number of specimens (no of spec.) (calculation as per Appendix A.3).

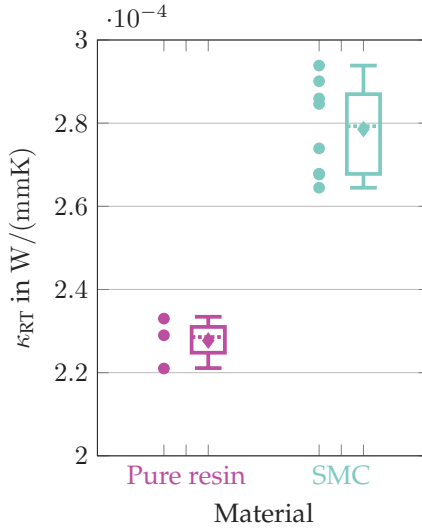


**Figure 4.22:** Thermal conductivity  $\kappa_{RT}$  at RT of pure resin (3 specimens) and SMC (8 specimens) determined by LFA experiments (in plate thickness direction): boxplot representation (for explanation see Appendix A.3.2).

	$\kappa(\theta = -10^\circ\text{C})$ in $W/(mm\text{ K})$	$\kappa(\theta = 80^\circ\text{C})$ in $W/(mm\text{ K})$	$\Delta \kappa_{rel,RT}$ in %
Pure resin	$2.36 \cdot 10^{-4}$	$2.28 \cdot 10^{-4}$	-3.52
SMC	$2.86 \cdot 10^{-4}$	$2.73 \cdot 10^{-4}$	-4.66

**Table 4.11:** Thermal conductivity  $\kappa$  at  $\theta = -10^\circ\text{C}$  and  $\theta = 80^\circ\text{C}$  and normalized difference  $\Delta \kappa_{rel,RT}$  (see Equation (4.2)) for pure resin and SMC (mean values over all tested specimens; measured in plate thickness direction by LFA experiments).

## 4.4 Damage and Failure

### 4.4.1 Damage

**Introducing remarks.** As introduced in Section 2.3.1, stiffness degradation is one important phenomenon of damage. Here, the anisotropic stiffness degradation due to uniaxial and biaxial tensile load and the influence of initial anisotropy is investigated. Therefore, in a first step uniaxial tensile experiments with bone specimens are performed and in a second step biaxial tensile experiments with cruciform specimens. The results of the two experimental series are compared and merged. All of the damage experiments are performed with the biaxial testing device. Strain is measured by DIC. The considered strain values are always the over the center area of the specimen averaged strains  $\bar{\varepsilon}_{ij}^I$  as defined in Equation (4.1). For a shorter and clearer notation, especially in the diagrams, in this section only  $\varepsilon_{11}$  and  $\varepsilon_{22}$  are written for  $\bar{\varepsilon}_{11}^I$  and  $\bar{\varepsilon}_{22}^I$ , respectively. The experimental data is partly taken from Schmidt (2019).

**Uniaxial testing with bone specimens.** For the uniaxial damage experiments, the bone specimens as introduced in Section 4.2 were used (Figure 4.7). The testing procedure is based on cyclic uniaxial tension with a stepwise load increase. Figure 4.23 shows the schematic strain path. The load is applied path-controlled by the displacement of one of the traverses. The strain rate is small (below 1%/min) such that it can be considered as quasistatic. Between the loading steps there are long waiting times (75 s) in order to have as similar conditions as possible with regard to viscoelastic effects at the beginning of each cycle. This ensures that the stiffness evaluated at the beginning of each cycle is comparable and changes are only/mainly due to damage. Remarks on investigations concerning the viscoelastic effects and the distinction of the different mechanical phenomena are given in

Section 4.5.3. During these waiting times the force is controlled to a low contact force (of negligible order of magnitude compared to load forces) to avoid compressive stress and buckling. Before starting the testing procedure itself, a pre-cycle is carried out to ensure that the specimen settles in the clamping jaws. The strain of the pre-cycles is of about  $\varepsilon_{11} = 0.2\%$ . Preliminary studies have shown that there occurs no significant damage up to a normal strain of about  $0.2\%$ .

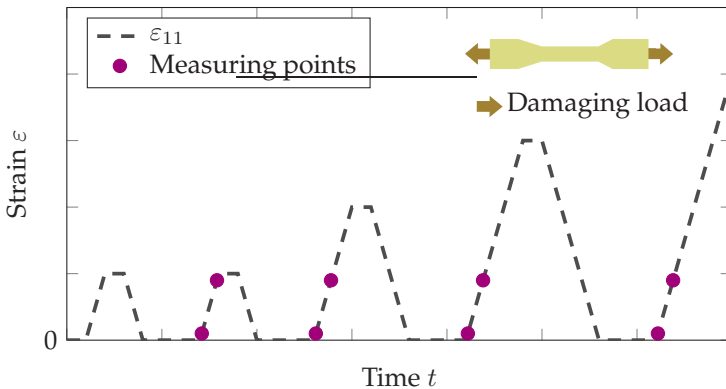


**Figure 4.23:** Schematic strain path for the experimental procedure of uniaxial stiffness degradation experiments.

The stiffness is evaluated using the values of force and strain at the measuring points marked in violet in Figure 4.23. These are at the beginning of each cycle after the waiting times to have similar conditions for each stiffness measurement. The lower measuring point is at a strain of approximately  $0.025\%$  and the upper is at a strain of approximately  $0.2\%$ . Thus Young's modulus is calculated via

$$E = \frac{\Delta F_1}{\Delta \varepsilon_{11}^I A} \quad (4.6)$$

with the force difference  $\Delta F_1$  and the strain difference  $\Delta \bar{\varepsilon}_{11}^I$  in the measuring direction (where  $\bar{\varepsilon}_{ij}^I$  is defined as in Section 4.2) and the cross sectional area  $A$  of the specimen.

Considering the two different plate variants (see Figures 2.4 and 2.5) and the different directions in the plates, three cases can be distinguished:

- Case a): Flow specimen, uniaxial damaging load in initially stiffer direction ( $0^\circ$ )
- Case b): Flow specimen, uniaxial damaging load in initially less stiff direction ( $90^\circ$ )
- Case c): Full specimen, uniaxial damaging load in an arbitrary direction ( $0^\circ$  and  $90^\circ$  are equal)

Figure 4.24 depicts the stiffness over the maximum reached strain  $\varepsilon_{\max} = \bar{\varepsilon}_{11,\max}^I$  for several specimens of all cases. The maximum reached strain  $\bar{\varepsilon}_{11,\max}^I$  is the maximum strain in the cycle before the measurement cycle which is the maximum strain ever reached in loading history until the instant of measurement. For comparability, the stiffness is normalized to its initial value  $E_0$  for each specimen. The markers of the individual stiffness measurements are connected by straight lines to indicate the course.

The stiffness degradation is clearly visible for all cases. For the flow specimens in  $0^\circ$ -direction (green dashed thick lines), it is the less pronounced, for the flow specimens in  $90^\circ$ -direction (blue thin dashed lines), it is the most pronounced and for the full specimens (red dotted lines) it lies in between. At a maximum strain of 1.0 %, the stiffness values ( $E/E_0$ ) lie at about 0.98 for the  $0^\circ$  flow specimens, at 0.89 for the  $90^\circ$  flow specimens, and at 0.95 for the full specimens. Due to scattering and fluctuations the exact quantitative evaluation must be considered with caution, but the tendency of the differences is significantly visible.

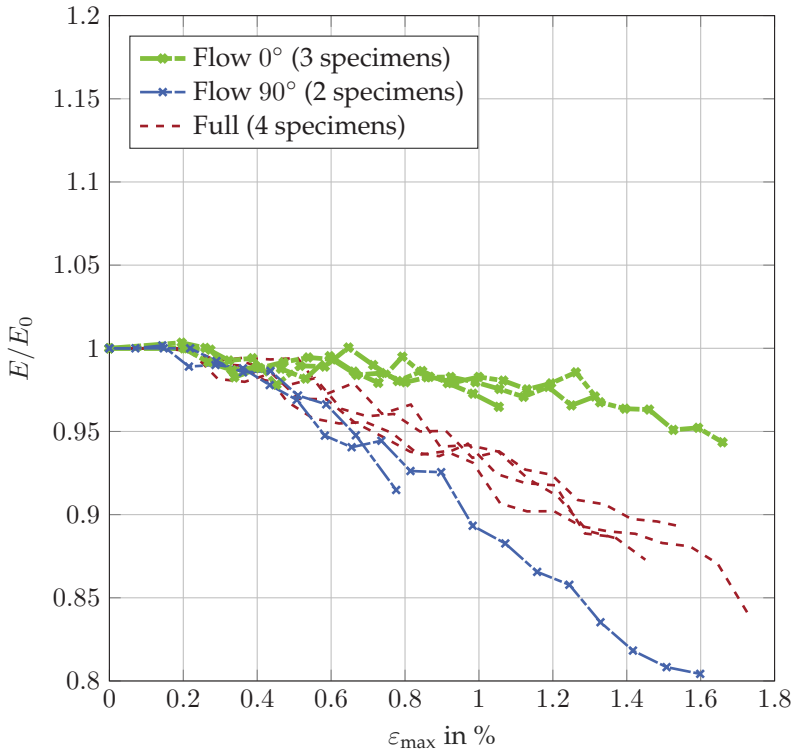


**Figure 4.24:** Normalized stiffness  $E/E_0$  over maximum reached strain ( $\varepsilon_{\max} = \bar{\varepsilon}_{11,\max}^I$ ) in load history for bone specimens loaded with uniaxial tension.

**Biaxial experiments.** The biaxial experiments are performed with the reinforced cruciform specimens introduced in Section 4.2 and exploited in detail in Section 4.5.1. Two testing procedures are performed with two different loading ratios as damaging load, which corresponds in principle to the testing procedure of the uniaxial damage experiments with bone specimens.

In the first testing procedure the damaging load corresponds to uniaxial tension. Figures 4.25 and 4.26 show a schematic strain and force path for this loading procedure. The damaging load is applied in one direction ( $e_1$ -direction) in a stepwise increasing way until failure (corresponds to the dashed black line in Figure 4.25 and Figure 4.26). Between these loading steps, a constant small (non-damaging) uniaxial tension (approx. 0.2%) in the perpendicular direction is applied (solid grey line). This allows for an observation of stiffness degradation in and perpendicular to the main loading direction. Between every loading step there are long waiting times (75 s) to have as similar as possible conditions regarding viscoelastic effects. The tensile load is applied path-controlled. Perpendicular to the respective loading direction, a force control ensures a low contact force to avoid any compressive load and buckling. This contact force can be considered as about zero (small compared to forces during loading and stiffness evaluation cycles). Thus the lateral contraction is allowed and the load states correspond always to planar stress states. As for the uniaxial load, pre-cycle is carried out before the testing procedure itself begins to ensure that the specimen settles in the clamping.

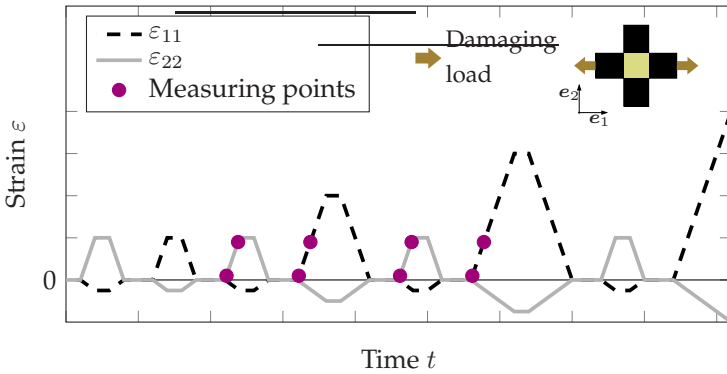


**Figure 4.25:** Schematic strain path for the experimental procedure with uniaxial tension as damaging load for cruciform specimens.

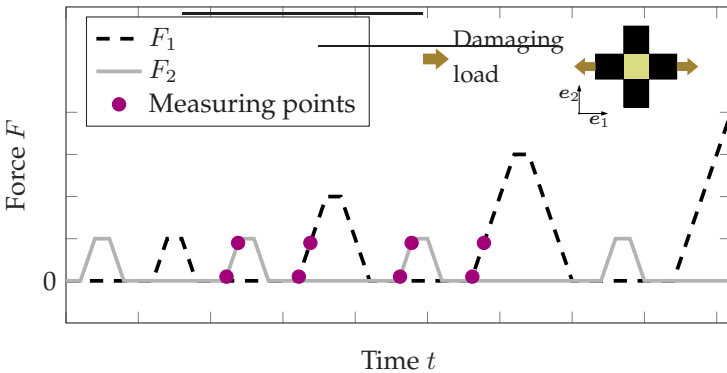


**Figure 4.26:** Schematic force path for the experimental procedure with uniaxial tension as damaging load for cruciform specimens.

In the second procedure, the damaging load corresponds to equibiaxial tension. Figures 4.27 and 4.28 show a schematic strain and force path. In principle, the testing procedure corresponds to the first testing

procedure. The difference is that the damaging load is equibiaxial tension (equi path-controlled, can lead to slightly different strains and different forces). In between the loading steps, now in both directions, a small constant load (approx. 0.2 %) is applied to evaluate the stiffness.

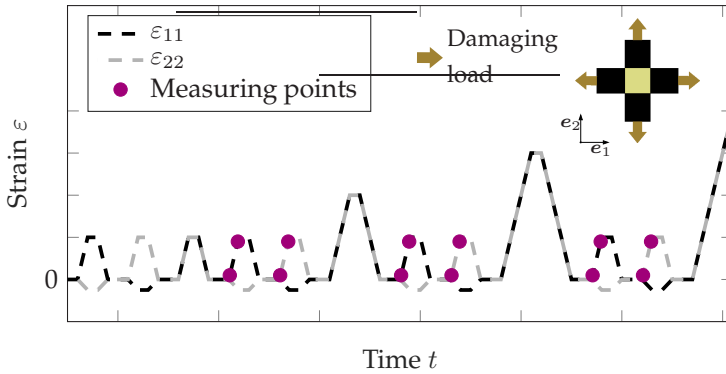


Figure 4.27: Schematic force path for the experimental procedure with equibiaxial tension as damaging load for cruciform specimens.

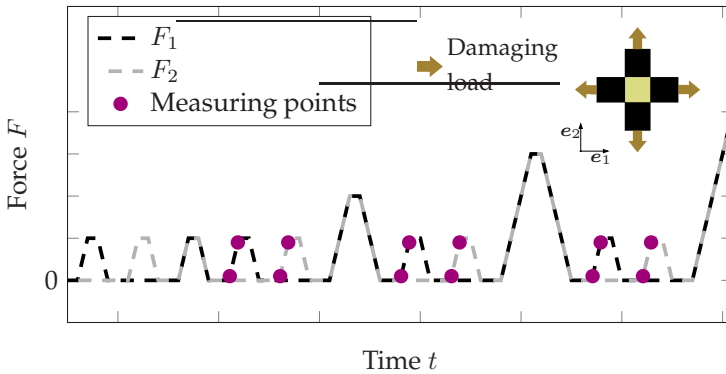


Figure 4.28: Schematic force path for the experimental procedure with equibiaxial tension as damaging load for cruciform specimens.

The stiffness is evaluated using the values of force and strain at the measuring points marked in violet in Figures 4.25 - 4.28. The lower measuring point is at a strain of approximately 0.025 %, the upper at a strain of approximately 0.2 %. For the uniaxial testing procedure in main loading direction this is at the beginning of each cycle, for the small measuring cycles it is at maximum and minimum of the load. As the stress and thus Young's modules can not be calculated directly, a equivalent stiffness  $\tilde{E}_i$  is introduced for load in direction  $e_i$

$$\tilde{E}_i = \frac{\Delta F_i}{\Delta \bar{\varepsilon}_{(i)(i)}^I}, \quad (4.7)$$

with  $\Delta F_i$  being the force difference in the  $e_i$ -direction and  $\Delta \bar{\varepsilon}_{(i)(i)}^I$  difference of the normal strain (averaged of the  $A^I$  as introduced in Section 4.2, parenthesis mean no summation over indices) in  $e_i$ -direction between the marked measuring points.

Both procedures are applied to specimens from flow plates (high anisotropy, see Figure 2.4) and from full plates (almost planar isotrop, see Figure 2.5). The cruciform specimens are cut from the plates such oriented that the direction of the arms corresponds to the  $0^\circ$ - and  $90^\circ$ -direction of the plates. For the uniaxial load and the flow specimens the damaging load is applied in the flow direction ( $0^\circ$ ) and in the non-flow direction ( $90^\circ$ ). This leads to 5 cases, where cases a), b), c) correspond to the cases of the uniaxial bone specimens.

- Case a): Flow specimen, uniaxial damaging load in initially stiffer direction ( $0^\circ$ )
- Case b): Flow specimen, uniaxial damaging load in initially less stiff direction ( $90^\circ$ )
- Case c): Full specimen, uniaxial damaging load in an arbitrary direction ( $0^\circ$  or  $90^\circ$ )
- Case d): Flow specimen, equibiaxial damaging load
- Case e): Full specimen, equibiaxial damaging load

In the following, the color- and line-scheme presented in Figure 4.29 is used. Cold colors (bluish, greenish) correspond to flow specimens and warm colors (reddish, yellow, orange) to full specimens. Thicker lines correspond to the initially stiffer direction ( $0^\circ$ , parallel to the flow direction) and thinner lines to the initially less stiff direction ( $90^\circ$ , perpendicular to flow direction). Dashed lines refer to the main (damaging) loading direction, solid lines to the not damagingly loaded direction, as already used in Figures 4.25 to 4.28.

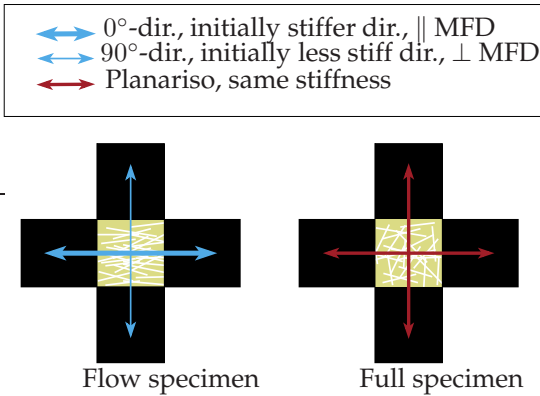
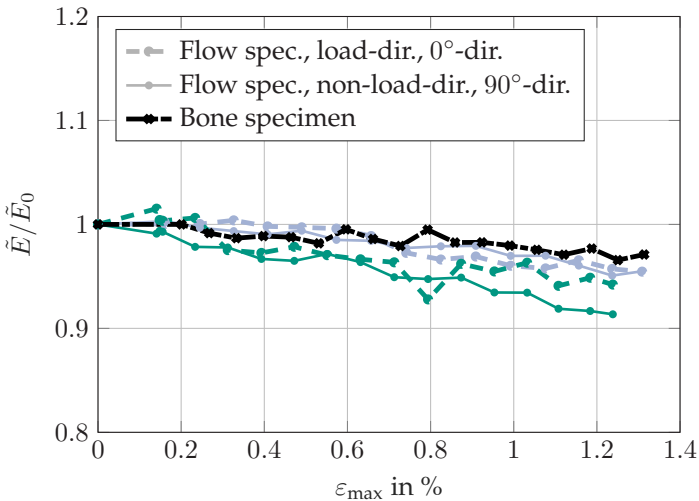


Figure 4.29: Color and line scheme.

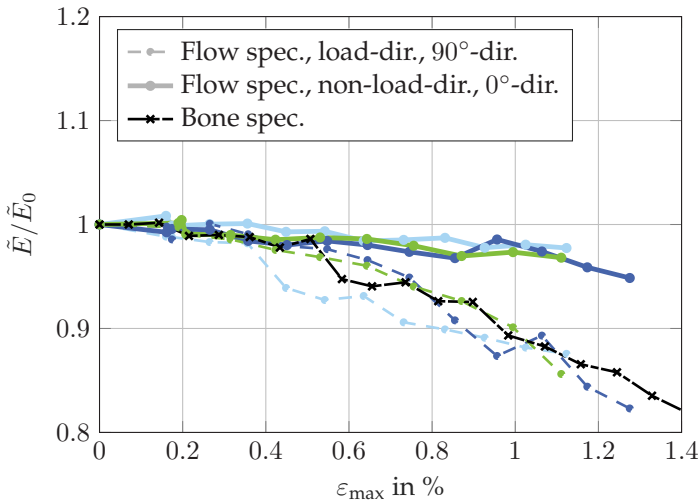
Figure 4.30 shows the result for case a), where uniaxial damaging load is applied in the initially stiffer direction (flow,  $0^\circ$ ). The equivalent stiffness as defined in Equation (4.7) over the maximum reached strain ( $\epsilon_{\max} = \bar{\epsilon}_{11, \max}^I$ ) in the loading direction is here depicted for several biaxial specimens and a corresponding uniaxial bone specimen for comparison. The maximum reached strain is the maximum strain in the cycle before the measurement cycle which is the maximum strain ever reached in loading history until the instant of measurement. For comparability, the stiffness is normalized to its initial value for each

specimen. Thus, also the stiffness evolution of the biaxial specimens can be compared to the Young's modulus evolution of the bone specimens. The stiffness degradation is only slightly pronounced, almost equivalent in the loading and the perpendicular direction, and slightly more pronounced in the non-loading direction which is the initially less stiff direction. So the damaging load in one direction leads also to a stiffness degradation in the perpendicular direction. The bone specimen's and biaxial specimen's curves are similar, whereas the bone specimen's curve lies slightly upper than the biaxial. The value of the normalized (equivalent) stiffness at a maximum strain of 1.0% lies at about 0.98 in loading direction and at varies between 0.94 and 0.97 in the perpendicular direction.



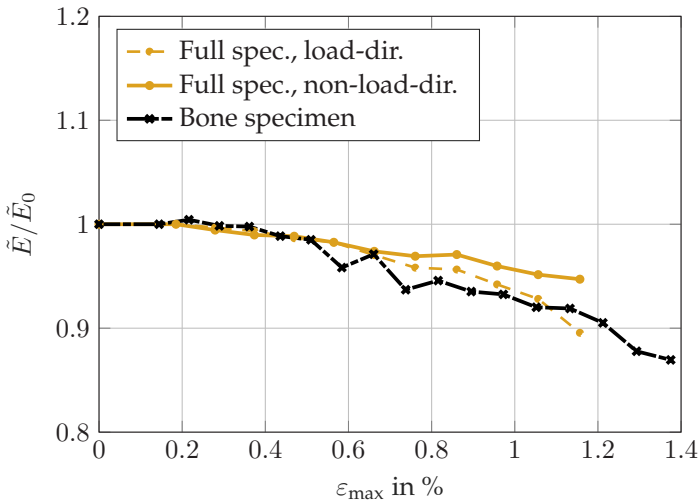
**Figure 4.30:** Normalized stiffness over maximum reached strain ( $\varepsilon_{\max} = \varepsilon_{11,\max}^I$ ) in load history; case a): flow specimens, uniaxial load in  $0^\circ$ -dir. One color corresponds to one specimen (2 tested specimens in total). Black line: corresponding bone specimen for comparison.

Figure 4.31 depicts the results for loading case b), where uniaxial damaging load is applied in the initially less stiff direction (non-flow,  $90^\circ$ ). The representation corresponds to that in Figure 4.30. The stiffness degradation is visible in both directions, but only slightly pronounced in non-loading direction, and significantly more pronounced in loading direction. The curve of the corresponding bone specimen fits good the results of the biaxial specimen. The value of the normalized (equivalent) stiffness at a maximum strain of 1% lies at about 0.89 in loading direction and at 0.98 in the perpendicular direction.



**Figure 4.31:** Normalized stiffness over maximum reached strain ( $\varepsilon_{\max} = \bar{\varepsilon}_{11,\max}^I$ ) in load history; case b): flow specimens, uniaxial load in  $90^\circ$ -dir. One color corresponds to one specimen (3 tested specimens in total). Black line: corresponding bone specimen for comparison.

In Figure 4.32 the results for loading case c) are depicted, where uniaxial damaging load is applied to a full specimen. The representation corresponds again to that in Figure 4.30. The stiffness degradation is visible in both directions, and slightly more pronounced in loading direction. The curve of the corresponding bone specimen fits good the results of the biaxial specimen. The value of the normalized (equivalent) stiffness at a maximum strain of 1% lies at about 0.96 in loading direction and at 0.97 in the perpendicular direction.



**Figure 4.32:** Normalized stiffness over maximum reached strain in load history; case c): full specimens, uniaxial load. (1 tested specimen in total) Black line: corresponding bone specimen for comparison.

Figure 4.33 shows the results for loading case d), where equibiaxial damaging load is applied to a flow specimen. The representation corresponds again to that in Figure 4.30, except that there is no corresponding bone specimen here. The stiffness degradation is visible in

both directions, and significantly more pronounced in the initially less stiff direction ( $90^\circ$ ). The value of the normalized (equivalent) stiffness at a maximum strain of  $0.5\%$  lies at about  $0.95$  in the initially stiffer direction and at  $0.83$  in the less stiff direction.

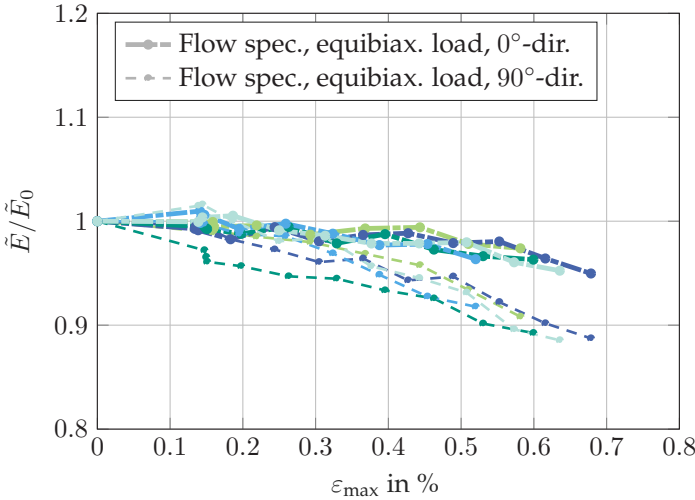


**Figure 4.33:** Normalized stiffness over maximum reached strain in load history ( $\epsilon_{\max} = \bar{\epsilon}_{11,\max}^I \approx \bar{\epsilon}_{22,\max}^I$ ); case d): flow specimens, equibiaxial load. One color corresponds to one specimen (5 tested specimens in total), different dash pattern indicates  $0^\circ$  and  $90^\circ$  direction.

Figure 4.34 shows the results for loading case e), where equibiaxial damaging load is applied to a flow specimen. The representation corresponds to that in Figure 4.33. The stiffness degradation is, as to expect, equal in both directions. This can be also considered as a validation. The value of the normalized (equivalent) stiffness at a maximum strain of  $0.5\%$  lies at about  $0.95$  in both directions.

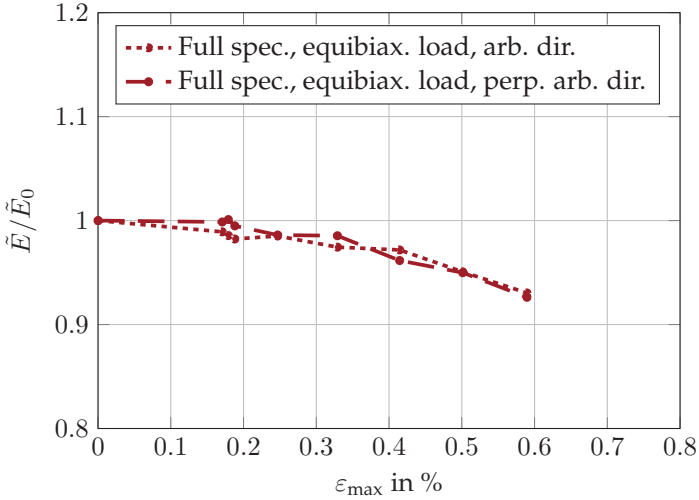


**Figure 4.34:** Normalized stiffness over maximum reached strain in load history ( $\epsilon_{\max} = \bar{\epsilon}_{11,\max}^I \approx \bar{\epsilon}_{22,\max}^I$ ); case e): full specimen (1 tested specimen in total), equibiaxial load.

**Conclusion damage experiments.** The experiments with the bone and biaxial specimens have shown that the stiffness degradation depends on the loading case as well as on the initial anisotropy. For comparable cases, the uniaxial and biaxial experiments match well.

To compare the stiffness degradation of the different cases, a linear fit to the normalized stiffness data of all specimens of one case and one direction is performed for each case and each direction. The linear fit starts at a strain of 0.2%. The relation can be expressed by the following equations

$$E/E_0 = 1 - d(\epsilon_{\max} - 0.2), \quad \tilde{E}/\tilde{E}_0 = 1 - d(\epsilon_{\max} - 0.2), \quad (4.8)$$

with  $\epsilon_{\max}$  in %. Figure 4.35 shows exemplarily the experimental data points for all specimens (uniaxial and biaxial) of case c) (full plate) in

loading direction and the fitted curve (straight line). This visualizes that a linear fit matches the principle course of the stiffness degradation curves well. Figure 4.36 shows the linear fits for the different cases. Table 4.12 depicts the values of the slope ( $d$  in Equation (4.8)) of the linear fits for all cases. Both highlight the dependence of stiffness degradation on both the loading case and the initial anisotropy. For uniaxial load, the difference in slope of main loading direction to non-load direction for full specimens (influence of loading case) is 0.038, and between load in  $0^\circ$ -direction and load in  $90^\circ$ -direction (influence of initial anisotropy) it is 0.10. This implies, that the influence of initial anisotropy is even higher than of load case. Overall, it can be stated that the stiffness reduction is not very pronounced. For all loading and anisotropy cases, the stiffness before failure still has a value above 80 % and most above 90 % of its initial value.

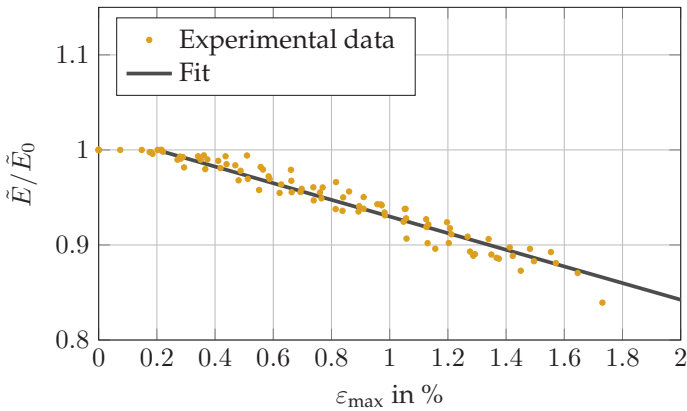


**Figure 4.35:** Normalized stiffness over maximum reached strain for case d); experimental data of all specimens and linear fit.

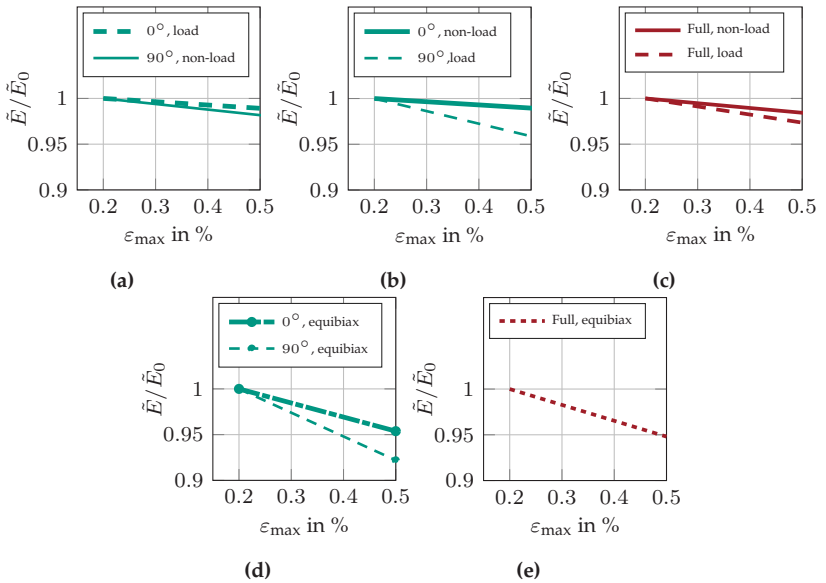


**Figure 4.36:** Stiffness degradation of the different cases: (a) case a): flow spec., load in  $0^\circ$ -dir.; (b) case b): flow spec., load in  $90^\circ$ -dir.; (c) case c): full spec., load in one dir.; (d) case d): flow spec. equibiax. load; (e) case e): full spec. equibiax. load. Linear fit to the experimental data. Color and line scheme according to Figure 4.29.

Spec.	Direction	Direction	Slope $d$
flow or full	load, non-load	$0^\circ, 90^\circ, \text{arb.}$	in Eq. (4.8)
a) flow	load	$0^\circ$	0.033
	non-load	$90^\circ$	0.053
b) flow	load	$90^\circ$	0.135
	non-load	$0^\circ$	0.032
c) full	load	arb.	0.087
	non-load	arb.	0.049
d) flow	equibiax. load	$0^\circ$	0.148
	equibiax. load	$90^\circ$	0.191
e) full	equibiax. load	arb.	0.177

**Table 4.12:** Slope ( $d$  in Equation (4.8)) of stiffness degradation for the different cases and directions. arb. means an arbitrary direction of a (approximately) planar isotropic full specimen.

## 4.4.2 Failure

Failure is investigated using partly the experiments that were conducted for the stiffness degradation investigation in Section 4.5.1 and some additional experiments with same testing procedure considering here the moment of failure (see Figures 4.23, 4.25 to 4.28). From these experiments, the failure stress is evaluated for small rectangular specimens (see Figure 4.9), bone specimens (see Figure 4.7), and for biaxial specimens (see Figure 4.8) from flow plates (see Figure 2.4). Additionally one shear experiment was performed with the specimen geometry in Figure 4.12. For bone specimens and small specimens the uniaxial failure stress is calculated directly by

$$\sigma_f = \frac{F_f}{A}, \quad (4.9)$$

where  $F_f$  is the maximum force before failure and  $A$  the cross sectional area of the specimen. Shear stress was calculated accordingly. For the biaxial cruciform specimens, stress can not be computed straight forward. For the stiffness degradation evaluation in Section 4.4.1 only the normalized values were considered using the equivalent stiffness depicted in Equation (4.7). To compare the actual failure stress, an experimental evaluation of the stresses and strains in uniaxial bone specimens and uniaxial loaded biaxial cruciform specimens was performed. This leads to a relation between the failure force of a biaxial specimen and its stress state. The stress in a biaxial cruciform specimen can thus be calculated via

$$\tilde{\sigma} = \frac{F}{d} f(\varepsilon) \quad (4.10)$$

where  $\tilde{\sigma}$  is the equivalent stress (corresponding to the actual stress),  $F$  is the force,  $d$  is the thickness of the specimen and  $f$  is a scalar numeric factor that can depend on the strain  $\varepsilon$ . For higher strains (greater than 0.5 %) the value of  $f$  remains constant ( $f \approx 0.00106 \text{ 1/mm}$ ). Thus, the failure stress of biaxial cruciform specimens can be calculated via

$$\sigma_{f, \text{biax}} = \frac{F_f}{d} f. \quad (4.11)$$

The procedure to find these relations is described in Section 4.5.1. It must be noted that this relation is only valid for this special biaxial specimen geometry.

Table 4.13 depicts the mean values, standard deviation (std) and coefficient of variation (CV) of the failure stresses for small specimens, bone specimens and uniaxial loaded biaxial specimens in  $0^\circ$ ,  $90^\circ$  and  $45^\circ$  (only small specimens). The mean values agree well, especially for bone specimens and biaxial specimens. The mean values of the small specimens are only slightly smaller. Thus in a second step, all specimen geometries are evaluated together. The results are depicted in Table 4.14.

Figure 4.37 shows the statistical evaluation of the failure stress for all specimens in a boxplot representation (for details on statistic evaluation and illustration see Appendix A.3). The mean value in  $0^\circ$ -direction is about 1.8 times greater than in  $90^\circ$ -direction and in  $45^\circ$ -direction the value lies in between. The CV is between 14 % and 27 %. This indicates a pronounced scattering of the failure stress. Considering the  $0^\circ$ -direction, the scattering is smaller than in the other directions. Figure 4.37 illustrates that there are two outliers. Without these outliers the relative standard deviation reduces to 9 %. The standard deviation in  $45^\circ$ -direction is at a high value of approximately 27 %, where here must be taken in to account that there is only a small number of tested specimens.

Table 4.15 depicts the statistical values for the failure stress for the cruciform specimens exposed to equibiaxial load. As the equibiaxial load is applied path controlled, the stresses in the two perpendicular directions are not equal. Thus, failure stress is evaluated in both directions separately. The failure stress values are, as to expect, smaller than for the uniaxial load, but especially in  $90^\circ$ -direction only very slightly. With a CV of 8 % and 16 % the scatter is in a similar range as for the uniaxially tested specimens.

The failure stress measured in the shear experiment is 55.6 MPa. Here must be mentioned that only two experiments were performed, the stress state corresponds not to a pure shear stress state and early failure in the edges occurred.

Dir.	Spec. geom.	no of spec.	Mean in MPa	Std in MPa	CV in %
0°	small	5	158.1	24.3	15.3
0°	bone	4	172.6	32.4	18.8
0°	biax	3	164.9	5.6	3.4
90°	small	4	89.3	25.2	28.2
90°	bone	2	98.8	27.5	27.8
90°	biax	3	96.1	12.3	12.8
45°	small	4	109.7	30.5	27.8

**Table 4.13:** Failure stress  $\sigma_f$  of SMC in different directions under tensile load (separate consideration of different specimen geometries); mean, standard deviation (std) and coefficient of variation (CV) (Calculation as per Appendix A.3).

	no of spec.	Mean in MPa	Std in MPa	CV in %
0°	12	164.6	23.4	14.2
90°	9	93.7	19.7	21.1
45°	4	109.7	30.5	27.8

**Table 4.14:** Failure stress  $\sigma_f$  of SMC in different directions under tensile load (all specimen geometries); mean, standard deviation (std) and coefficient of variation (CV) (Calculation as per Appendix A.3).

Dir.	no of spec.	Mean in MPa	Std in MPa	CV in %
0°	7	111.5	18.6	16.7
90°		88.0	7.6	8.7

**Table 4.15:** Failure stress  $\sigma_f$  of SMC under equibiaxial (equi path controlled) tensile load; mean, standard deviation (std) and coefficient of variation (CV) (Calculation as per Appendix A.3).

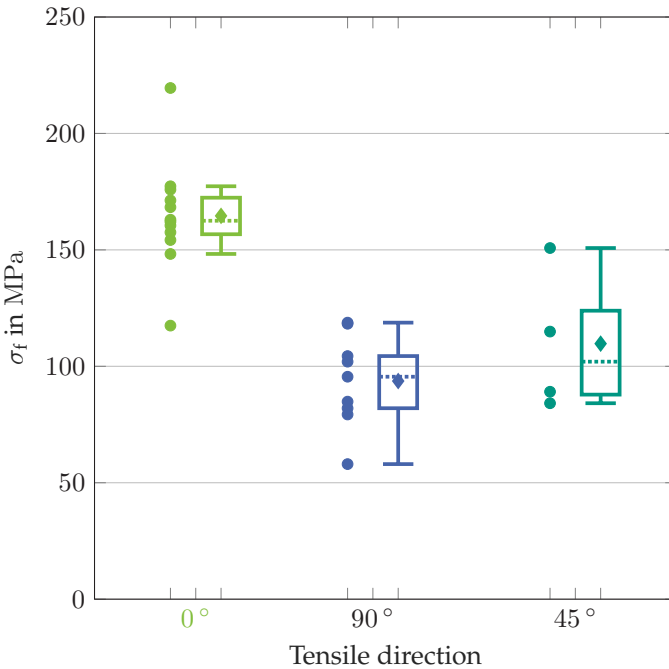


**Figure 4.37:** Failure stress  $\sigma_f$  of SMC (flow plate) for uniaxial tensile load in 0°, 90°, 45°-direction: boxplot representation (for explanation see Appendix A.3.2).

## 4.5 Additional Investigations

### 4.5.1 Biaxial Specimen Design Investigations

The considered special biaxial specimen design was introduced by Schemmann et al. (2018c) and further investigated in this thesis. The advantage of this specimen design is that the specimen arms are reinforced by unidirectional carbon fiber tapes which avoids early failure in the specimen's arms. This feature is essential for biaxial damage and failure investigations. Figure 4.38 show a photograph of the specimen and Figure 4.39 a schematical cross sectional view. For the manufacturing, the cruciform shaped specimens are cut by water jet cutting from fully continuous carbon fiber reinforced plates which are manufactured as described in Section 2.1.2. In a second step the center area is milled out with a gentle milling process in order to expose the pure discontinuous glass fiber reinforced SMC material.

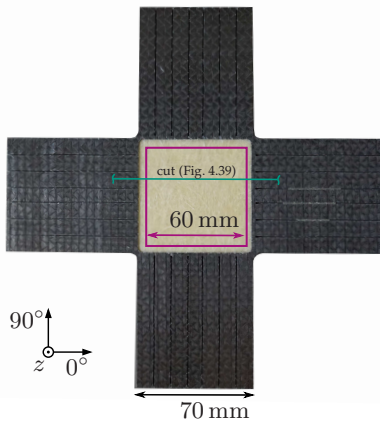


**Figure 4.38:** Biaxial discontinuous glass fiber SMC specimen with continuous carbon fiber reinforced arms, with milled pockets, area of interest  $A^I$  in violet. Cut for cross section in Figure 4.39 in turquoise.

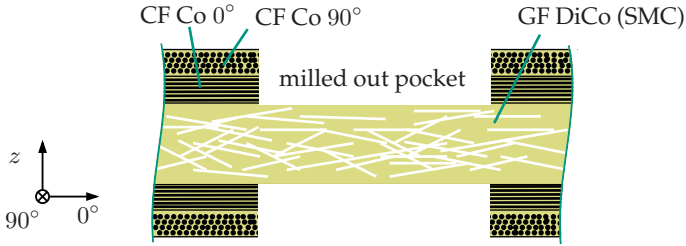


**Figure 4.39:** Cross section (cut) of biaxial specimen of Figure 4.38.

In the following, some aspects of investigations on this specimen design are presented.

- Investigation on the homogeneity of the strain field in the center area of this specimen design are discussed in Lang et al. (2018).
- In Lang et al. (2019) first results are presented that state the comparability of the stiffness degradation with uniaxial tested bone specimen. In this theses detailed investigations of the stiffness degradation behavior of bone specimens and these biaxial specimens are conducted. One result concerning the suitability of the presented specimen design is that the stiffness degradation of the biaxial specimens is similar to the stiffness degradation of bone specimens for a comparable load case.
- Furthermore it was investigated whether the anisotropy ratio determined by measurements with the biaxial specimen correspond to the real anisotropy ratio of the SMC material and not to geometry or other effects. Therefore, small specimens were cut from a preliminary non-damaging tested biaxial specimen as shown in Figure 4.40. The anisotropy ratio of the biaxial specimen and the anisotropy calculated from the small specimens matched well ( $\Gamma_{0/90, \text{biax}} = 1.32$  and  $\Gamma_{0/90, \text{small}} = 1.28$ ).

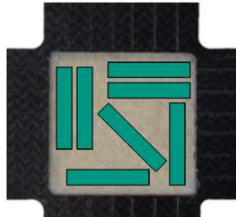


Figure 4.40: Small specimens cut from biaxial specimen.

- Simulations with slight variation of geometry at slits end were performed to investigate if these changes influence the stress in the center area. The simulations showed that variations of about 1mm lead to changes in stress of maximum 1 %.
- The stress state in the center area of the biaxial specimen cannot be calculated straight forward. In order to assess the averaged stress, an experimental evaluation of the stresses and strains in uniaxial bone specimens and uniaxial loaded biaxial cruciform specimens was performed. Specimens with comparable anisotropy ratios were chosen (anisotropy on biaxial specimen within one specimen, anisotropy of bone specimen between two specimens of same plate close to each other). It is assumed that stiffness of these specimens is similar and thus stress is comparable for similar measured strain states. This procedure leads to a relation between force (which is measured directly) of a biaxial specimen and its stress state. The stress in a biaxial cruciform specimen can thus be calculated via

$$\tilde{\sigma} = \frac{F}{d} f(\varepsilon) \quad (4.12)$$

where  $\tilde{\sigma}$  is the equivalent stress (corresponding to the actual stress),  $F$  is the force,  $d$  is the thickness of the specimen and  $f$  is a scalar numeric factor that can depend on the (normal) strain  $\varepsilon$ . Figure 4.41 shows the factor over strain. The factor  $f$  decreases and

converges for higher strains (greater than 0.5 %) to a constant value ( $f \approx 0.00106$  1/mm).

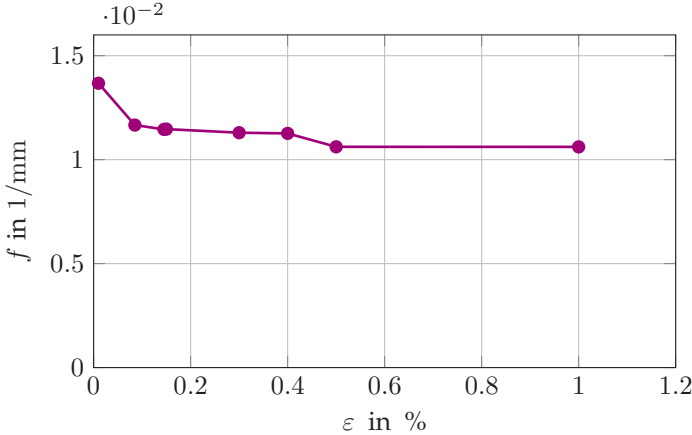


**Figure 4.41:** Factor  $f(\varepsilon)$  for the relation of equivalent stress in cruciform specimen and measured Force in dependence of normal strain (see Equation (4.12))

## 4.5.2 DIC Investigations

In order to examine the suitability of the DIC strain measurement for the experiments of this work, several investigations and considerations were carried out.

The given accuracy is according to manufacturer a strain of  $\varepsilon \approx 0.03$  %. Non-damaging strains for SMC that should be used for stiffness determination are below 0.2 %. Thus, measuring errors above 10 % could occur.

Experiments were performed in which a rigid body movement was applied to a specimen to check if the strain field measured by DIC is equal to zero or if erroneously deformations are detected. The result is, that strain fluctuations were detected up to 0.15 %. Using spacial mean

filter and changing parameters of the DIC evaluation (facette size e.g.) reduces these errors to a strain of 0.025 %. But the local resolution is thus reduced, too.

To investigate the reproducibility of the strain field and to investigate whether strain field on the different sides of a specimen coincide, one specimen was measured several times with a non-damaging uniaxial tensile load:

- Measurement 1: front side (m1)
- Measurement 2: back side (m2)
- Measurement 3: front side (m3)

The geometry of the specimen is given in Figure 4.9. The strain field at comparable load situations was compared. The forces at the observation moment differ of about maximum 1.3 %. Thus, the assumption of a comparable load situation can be made. The averaged strain matches for all three considered measurements with a difference of maximum 3 %. Thus, the averaged strain values are reproducible and similar for front and back side. Figure 4.42 shows the strain fields ( $\varepsilon_{11}$ ) for the three measurements. It is visible that the strain fields differ. Measurement 1 and Measurement 3 (same specimen side) show a similar strain field, but still small differences are visible. The strain field of Measurement 2 show a significantly different strain field. It can be concluded that the strain field on one specimen side is reproducible including certain differences and the strain field on the other specimen side is different. Probably surface effects are measured due to microstructure variations over the thickness of the specimen. Additionally, the specimens are relatively small compared to standard specimens for the DIC measuring area. Thus, edge effects may play a role, too.

These investigations show that DIC is suitable for determining the locally resolved strain field at the surface. However, the measured strain field cannot be transferred to the entire specimen thickness (in

the case of the approximately 2mm to 3mm thick SMC specimens). For both the local strain field and the averaged strain the measurement inaccuracies must be taken into account, especially for small strains and small specimens.

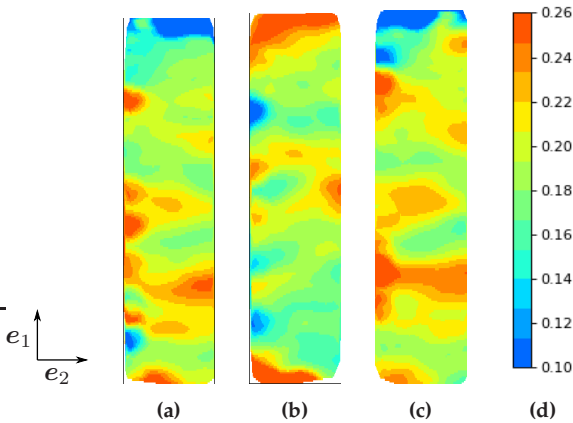


**Figure 4.42:** Strain fields ( $\varepsilon_{11}$ ) measured by DIC of one specimen measured several times on front and back side. (specimen dimensions: 10mm x 50mm). (a) m1: front side, (b) m2: back side, (c) m3: front side, (d) legend:  $\varepsilon_{11}$  in %.

### 4.5.3 Comparison of Viscoelastic and Damage Effect on Stiffness of SMC

Investigations on bone specimens were performed that enable to assess the effect of viscoelasticity and damage, respectively, on stiffness. The diagram of Figure 4.43a shows the schematic strain curve of the testing procedure, with long waiting times between the loading cycles in order to have the same conditions regarding viscoelastic effects at the beginning of each cycle. The colored sections in the load paths are the sections in which the stiffness was calculated, which is plotted in the

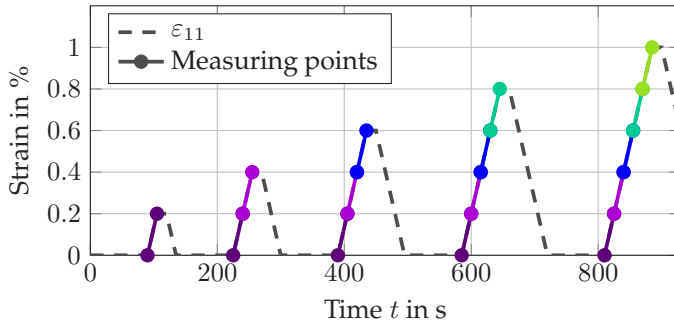
diagram of Figure 4.43b. In this diagram, stiffness values are plotted over cycles, which means over a maximum achieved strain, where per cycle the strain was increased by 0.2%. So, dark purple is the stiffness at the beginning of each cycle (approximately between 0% and 0.2% strain, ), light purple is the stiffness calculated between 0.2% and 0.4% strain, blue between 0.4% and 0.6%, etc (in rainbow colors).

Thus, the dark purple points (connected with dark purple line) in Figure 4.43b show the stiffness at the beginning of each cycle and illustrate a stiffness reduction caused by the damaging strain in the previous load cycles. Thus, in each curve by itself, one can see a stiffness reduction due to damage.

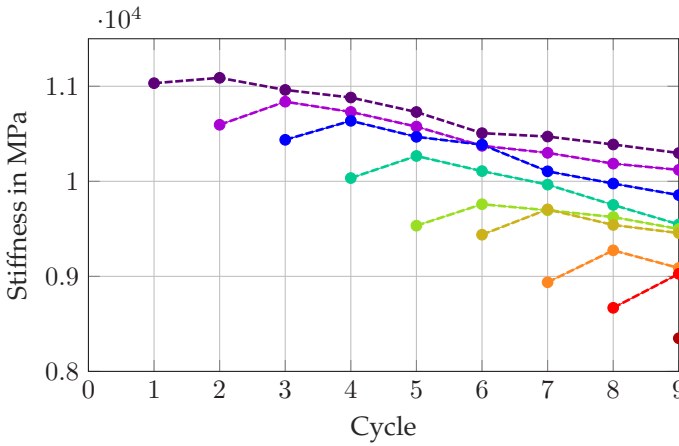
If we now compare different color points in the same cycle (i.e. the same damage state), we can see the stiffness differences at different strain levels. For example, let us consider the values at cycle 6: the stiffness at the beginning of the cycle (dark-purple) is significantly greater than the stiffness at greater strains towards the upper end of the cycle (e.g. green). This difference in stiffness could be due to nonlinear elasticity or viscoelasticity. Moreover, the stiffness at the beginning of unloading, i.e. at large strain, is rather as large as at the beginning of loading ( this cannot be seen in these diagrams). This implies that viscoelastic effects, rather than nonlinear elasticity, are likely involved.

Comparing the stiffness differences within one color after different cycles (damage) with the stiffness differences of different colors in the same cycle (viscoelasticity), it is visible that the stiffness differences are in similar orders of magnitude or the viscoelastic caused differences are even greater.

However, Kehrer (2019) has shown that the viscoelastic effects in DMA measurements are very small for SMC at room temperature.



(a)



(b)

**Figure 4.43:** Viscoelastic versus damage effects. (a) Testing procedure, (b) Stiffness over cycle, e.g. max. strain.

## 4.6 Summary and Discussion of Experimental Results

In this section all experimental results are summarized, discussed, and related to each other.

Table 4.16 shows the coefficient of variation (CV) for all identified parameters for pure resin and the different SMC directions. This allows to compare the scattering of all material parameters. The CV for pure resin is below 3% for almost all determined parameters. Assuming a homogeneous material behavior of the resin, this is an indication of high measuring accuracy. For heat capacity, the error is slightly above 3%. The reason for the slightly larger scatter here probably lies in the measurement inaccuracy of the LFA method for the heat capacity.

The thermoelastic material parameters of SMC measured in the different directions in the  $0^\circ$ - $90^\circ$ -plane (Young's modulus, Poisson's ratio, thermal expansion coefficient) show CVs of around 10%. The parameters measured in plate thickness direction (thermal diffusivity, thermal conductivity) show CVs below 5%. A probable reason for the different heights of scattering is that the microstructure in terms of fiber orientation varies more in the  $0^\circ$ - $90^\circ$ -plane. In the plate thickness direction only very slight orientation variations are possible because the thickness of the plate is much smaller than the fiber length.

CV of failure stress reaches values of up to 20%. Additionally to the varying fiber orientation, micro defects that can lead to early failure play a more pronounced role.

Scattering of all SMC parameters is also caused by other microstructure differences than fiber orientation, as for example fiber volume content distribution.

	$E$	$\nu$	$\alpha$	$\kappa$	$c_p$	$a$	$\sigma_f$
Pure resin	2.13	/	0.40	2.72	3.01	1.02	/
SMC 0°	9.99	5.82	9.61	/	/	/	14.2
SMC 90°	8.92	9.47	9.04	/	/	/	21.1
SMC perp.	/	/	/	4.10	/	4.79	/
SMC non-dir.	/	/	/	/	1.28	/	/

**Table 4.16:** Coefficient of variation (CV) in % for all experimentally determined material parameters for pure resin and different SMC directions (perp.: perpendicular to 0°-90°-plane, non-dir.: non-directional).

With Table 4.17, the influence of the different factors on the material parameter can be analysed. The relative change of the individual parameter due to the different causal factors are given and defined as

$$\Delta_{\xi_{\text{rel,RT}}}^{\xi^{\text{cause}}} = \frac{\xi_{\text{max}}^{\text{cause}} - \xi_{\text{min}}^{\text{cause}}}{\xi_{\text{RT}}}. \quad (4.13)$$

Here,  $\xi_{\text{RT}}$  is the averaged RT value as introduced in Section 4.3.1, and  $\xi_{\text{max}}^{\text{cause}}$  and  $\xi_{\text{min}}^{\text{cause}}$  are the maximum and minimum values, where only the indicated factor (cause) is changed and the other causes remain unchanged. In particular, this means the following:

- $\Delta_{\xi_{\text{rel,RT}}}^{\xi^{\text{micr}}}$ : relative difference between maximum and minimum value occurred in measurements (at room temperature, in one direction) related to the mean value; probably mainly caused by microstructure variations
- $\Delta_{\xi_{\text{rel,RT}}}^{\xi^{\text{temp}}}$ : relative difference between the values of the edges of the considered temperature range (as already defined in Equation (4.2))
- $\Delta_{\xi_{\text{rel,RT}}}^{\xi^{\text{dam}}}$ : difference between the value of the parameter in a fully undamaged state and the value at maximum damaged state before failure related to the undamaged value, only applicable for Young's modulus

- $\Delta \zeta_{rel,RT}^{visco}$ : only applicable for Young's modulus, relative difference between maximum and minimum value due to visco effects for Young's modulus occurred in the considered load procedure in the investigations presented in Section 4.5.3

Not all of the above factors can be applied to all parameters. However, these considerations allow to assess which factors should be considered under given conditions when modeling the material behavior. Relative differences in the range of 20 % occur due to microstructure variations for Young's modulus and thermal expansion. For the other parameters the relative difference is smaller, in a range up to about 10 %. As mentioned above the reason lies here in the smaller fiber orientation variation. Thus, measuring of these parameters in the 0°-90°-plane would probably lead to variations in the same order of magnitude as for Young's modulus and thermal expansion. In each case this shows that microstructure is important to account for.

Changes due to temperature dependence of the parameters occur between approximately 0 % and 20 % depending on the individual parameters and directions.

Changes of Young's modulus due to damage are small in 0°-direction but up to almost 20 % in 90°-direction. But when a certain damage state is reached the material is no longer applicable. The effect of viscoelastic effects (see Section 4.5.3) is in the same order of magnitude. Thus, even when not modeling, it is important to be aware of these effects, to, for example, adjust testing procedures for damage experiments to exclude these effects.

	$\Delta \xi_{\text{rel,RT}}^{\text{micr}}$ in %	$\Delta \xi_{\text{rel,RT}}^{\text{temp}}$ in %	$\Delta \xi_{\text{rel,RT}}^{\text{dam}}$ in %	$\Delta \xi_{\text{rel,RT}}^{\text{visco}}$ in %
$E_{0^\circ}$	14.9	9.5	$\sim 5$	$\sim 20$
$E_{90^\circ}$	24.3	13.0	$\sim 18$	/
$\alpha_{0^\circ}$	17.3	0.6	/	/
$\alpha_{90^\circ}$	22.7	9.95	/	/
$\kappa$	10.7	4.66	/	/
$c_p$	3.3	14.8	/	/
$a$	8.1	18.5	/	/

**Table 4.17:** Comparison of the influence of microstructure (or undefined scattering), temperature, damage and visco effects on material parameters. Absolute values of relative difference  $\Delta \xi_{\text{rel,RT}}^{\text{cause}}$  (Equation (4.13)) of the individual parameters for pure resin and SMC in different directions.

## Chapter 5

# Parameter Identification - Merging Modeling and Experiments

## 5.1 Thermoelastic Model

### 5.1.1 Introducing Remarks

In the following two sections the two thermoelastic material models (with constant and with temperature-dependent coefficients) introduced in Section 3.1 are considered. The parameters are identified using the experimental results presented in Section 4.3. The parameter identification was performed so that model and experiment match at room temperature. Thus, a comparability of the two models is given.

SMC from flow plates (see Figure 2.4) and pure resin material is considered. For the parameters measured in the plate thickness direction (thermal diffusivity, thermal conductivity), and non directional parameters (heat capacity), values averaged over all specimens are used. However, for those measured in the  $0^\circ$ - $90^\circ$ -plane (stiffness and the coefficient of thermal expansion), selected specimens are considered, since the scatter of the SMC parameters is too high for meaningful results.

All of the material coefficients introduced in Section 3.1 are considered. For the tensorial coefficients, particular parameters/components corre-

sponding to the experimentally measurable parameters are considered. These are specified for each coefficient. Here, the  $0^\circ$ - and  $90^\circ$ -direction of Figure 2.4 correspond to the  $e_1$ - and  $e_2$ -direction, respectively, and the plate thickness direction, perpendicular to the  $0^\circ$ - $90^\circ$ -plane, corresponds to the  $e_3$ -direction.

In order to assess the quality of the models, the relative error is introduced as

$$\epsilon_{\text{rel}}(\theta) = \frac{\xi_{\text{mod}}(\theta) - \xi_{\text{exp}}(\theta)}{\xi_{\text{exp}}(\theta)}, \quad (5.1)$$

where  $\xi_{\text{mod}}(\theta)$  is the value of the parameter determined by the material model and  $\xi_{\text{exp}}(\theta)$  is the value of the parameter determined by the experiment. The relative error is considered over the entire observed temperature range for each parameter.

### 5.1.2 Constant Coefficients

For the material model with constant coefficients (Section 3.2.1), the values of the modeled parameter are set to the room temperature values  $\xi_{\text{RT}}$  (see Section 4.3.1).

Measurement of stiffness is conducted in form of Young's modulus and Poisson's ratio. The Young's modulus  $E(\mathbf{n})$  is defined as the ratio of tensile stress  $\sigma$  and tensile strain  $\varepsilon$  when applying uniaxial stress in direction  $\mathbf{n}$ . Young's modulus can then be expressed in terms of the stiffness tensor  $\mathbb{C}$  by

$$E(\mathbb{C}, \mathbf{n}) = ((\mathbf{n} \otimes \mathbf{n}) \cdot \mathbb{C}^{-1}[\mathbf{n} \otimes \mathbf{n}])^{-1}. \quad (5.2)$$

Considering the directions  $\mathbf{n} = e_1$  and  $\mathbf{n} = e_2$ ,  $E(\mathbb{C}, e_1) = E_1$  and  $E(\mathbb{C}, e_2) = E_2$  correspond to the the Young's modulus measurements in  $0^\circ$ - and  $90^\circ$ -direction, respectively. For the same case of uniaxial tensile stress into direction  $\mathbf{n}$ , Poisson's ratio is defined as the negative ratio of normal strain in one perpendicular direction  $\mathbf{n}_\perp$  to normal strain in

loading direction  $\mathbf{n}$ . It can then be expressed in terms of stiffness tensor as

$$\nu(\mathbb{C}, \mathbf{n}) = -\frac{((\mathbf{n} \otimes \mathbf{n}) \cdot \mathbb{C}^{-1}[\mathbf{n}_\perp \otimes \mathbf{n}_\perp])^{-1}}{((\mathbf{n} \otimes \mathbf{n}) \cdot \mathbb{C}^{-1}[\mathbf{n} \otimes \mathbf{n}])^{-1}}. \quad (5.3)$$

Considering again directions  $\mathbf{n} = \mathbf{e}_1$  and  $\mathbf{n} = \mathbf{e}_2$ ,  $\nu(\mathbb{C}, \mathbf{e}_1) = \nu_{12}$  and  $\nu(\mathbb{C}, \mathbf{e}_2) = \nu_{21}$  corresponds to the Poisson's ratio of measurements in in  $0^\circ$ -direction (with lateral contraction in  $90^\circ$ -direction) and vice versa, respectively.

The results for two individual SMC specimens are considered, one with  $0^\circ$  and one with  $90^\circ$  as measuring direction, taken from the same plate with similar microstructure (27f-18-0 and 27f-14-90, FOTs can be found in Appendix A.6) and one pure resin specimen (arbitrary direction). The values from the tensile experiments presented in Section 4.3.2 lead for these specimens and the pure resin material to the following identified parameters:

- $E_{\text{PR}} = 2619 \text{ MPa}$
- $E_{\text{SMC},1} = 11415 \text{ MPa}$
- $E_{\text{SMC},2} = 8352 \text{ MPa}$

From the dilatometer measurements presented in Section 4.3.3, the components of the thermal expansion coefficient can be identified. The thermal expansion coefficient, evaluated in one direction  $\mathbf{n}$  can be expressed in dependence of the thermal expansion tensor  $\boldsymbol{\alpha}$  as

$$\alpha(\boldsymbol{\alpha}, \mathbf{n}) = \boldsymbol{\alpha} \cdot (\mathbf{n} \otimes \mathbf{n}). \quad (5.4)$$

Considering again the directions  $\mathbf{n} = \mathbf{e}_1$  and  $\mathbf{n} = \mathbf{e}_2$ ,  $\alpha(\mathbf{e}_1) = \alpha_{11}$  and  $\alpha(\mathbf{e}_2) = \alpha_{22}$  correspond to the the thermal expansion taken from dilatometer measurements in  $0^\circ$ - and  $90^\circ$ -direction, respectively. The same two specimens are considered as for Young's modulus. The following parameter values are identified:

- $\alpha_{\text{PR}} = 6.30 \cdot 10^{-5} \text{ 1/K}$

- $\alpha_{\text{SMC},11} = 1.76 \cdot 10^{-5} \text{ 1/K}$
- $\alpha_{\text{SMC},22} = 2.39 \cdot 10^{-5} \text{ 1/K}$

Analogously to the thermal expansion coefficient, thermal conductivity or thermal diffusivity can be expressed, whereas here, the measuring direction is the third, plate thickness direction corresponding to  $\mathbf{n} = \mathbf{e}_3$ . Thus, the parameters  $\kappa_{33}$  and  $a_{33}$  are identified:

- $\kappa_{\text{PR}} = 2.27 \cdot 10^{-4} \text{ W/(mm K)}$
- $\kappa_{\text{SMC},33} = 2.79 \cdot 10^{-4} \text{ W/(mm K)}$
- $a_{\text{PR}} = 0.142 \text{ mm}^2/\text{s}$
- $a_{\text{SMC},33} = 0.172 \text{ mm}^2/\text{s}$

Heat capacity is measured as  $c_p$ , which is the heat capacity at constant pressure, where in the material model (Section 3.1) the heat capacity at constant strain  $c_\varepsilon$  is considered. It is assumed that the difference is very small, and therefore  $c_\varepsilon \approx c_p$  is valid. As  $c_p$  is no directional coefficient, the following two parameter values are identified:

- $c_{p\text{PR}} = 1.40 \text{ J/(g K)}$
- $c_{p\text{SMC}} = 1.06 \text{ J/(g K)}$

The remaining parameters are the reference temperature, which is here chosen as the room temperature ( $\text{RT}=20^\circ\text{C}$ ) and the constant mass density, taken from Trauth (2018) ( $\rho_{\text{PR}} = 1.14 \text{ g/cm}^3$  and  $\rho_{\text{SMC}} = 1.53 \text{ g/cm}^3$ ). In the following diagrams, Figures 5.1 to Figure 5.5, all individual parameters are displayed over temperature for the different SMC directions and pure resin. For each parameter, the modeled values, which means here the constant value over the entire temperature range, the experimental results, and the relative error as defined in Equation (5.1) is shown.

Young's modulus (Figure 5.1), shows an increasing error of up to 25 % for pure resin and slightly more than 10 % for  $90^\circ$  SMC and slightly less than 10 % for  $0^\circ$  SMC at  $80^\circ\text{C}$  due to the decreasing trend of the experimental data. In a temperature range up to approximately  $50^\circ\text{C}$

the error for SMC in both directions remains under 5 %.

The increasing course of the thermal expansion coefficient (see Figure 5.2), leads to negative error values with up to about -20 % for pure resin and 90° SMC. The approximately constant course in the 0° direction leads to a maximum error of below 5 %. On the other hand, for SMC in 90°-direction, the 5 % are already exceeded at a temperature of 40°C.

Heat capacity (Figure 5.3) reaches relative errors of up to about 10 % for pure resin and for SMC at 80°C as well as at -10°C whereas the error for SMC is slightly smaller than for the pure resin.

For the thermal conductivity (see Figure 5.4), the error remains always under 5 % for all temperatures for SMC as well as for pure resin.

The error of thermal diffusivity (Figure 5.5) reach absolute values of up to approximately 10 % at -10°C and 80°C for SMC and for pure resin due to the decreasing trend. The 5 % are exceeded already at 40°C and 0°C.

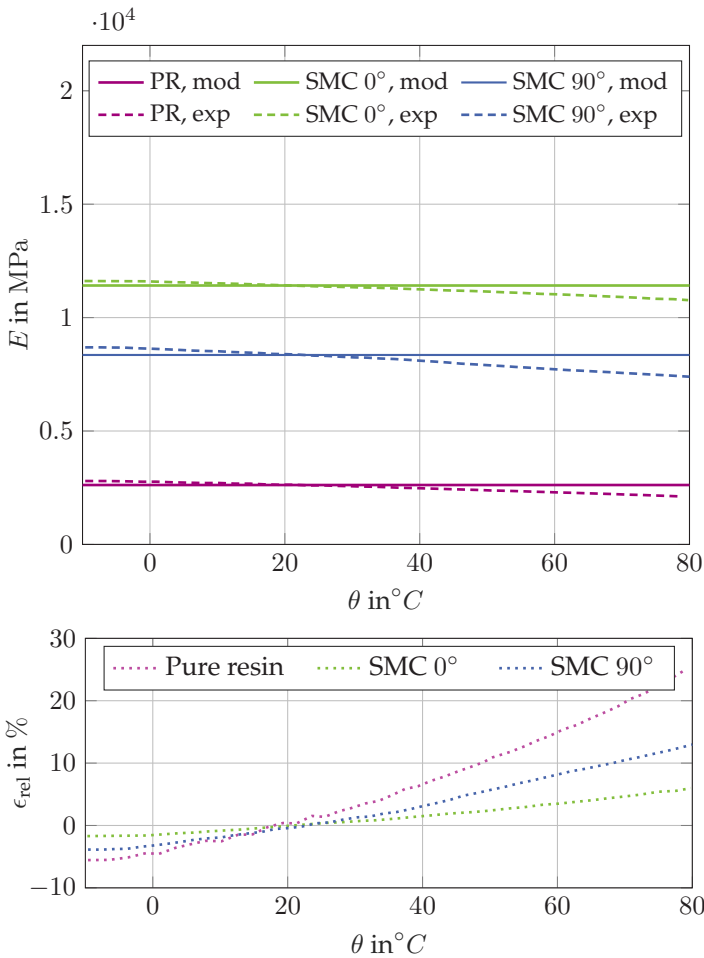


**Figure 5.1:** Young's modulus  $E(\theta)$  of pure resin and SMC over temperature  $\theta$ ; experimental results (selected specimens), modeled results (constant fit to the experimental data) (upper diagram) and relative error  $\epsilon_{rel}$  (see Equation (5.1)) (lower diagram).

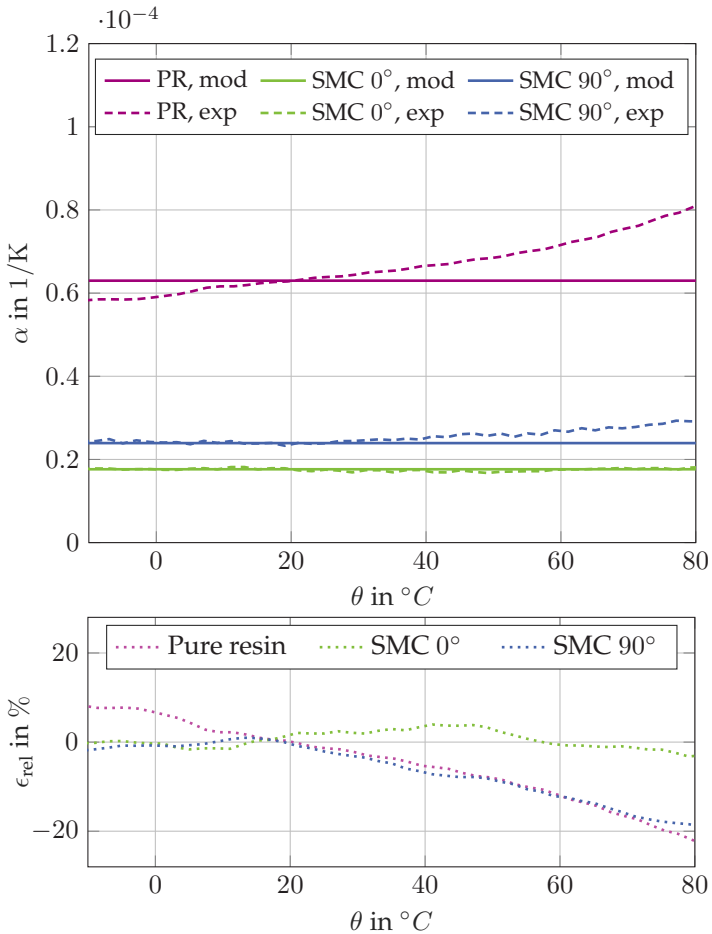


**Figure 5.2:** Thermal expansion coefficient  $\alpha(\theta)$  of pure resin and SMC over temperature  $\theta$ ; experimental results (selected specimens), modeled results (constant fit to the experimental data) (upper diagram) and relative error  $\epsilon_{\text{rel}}$  (see Equation (5.1)) (lower diagram).

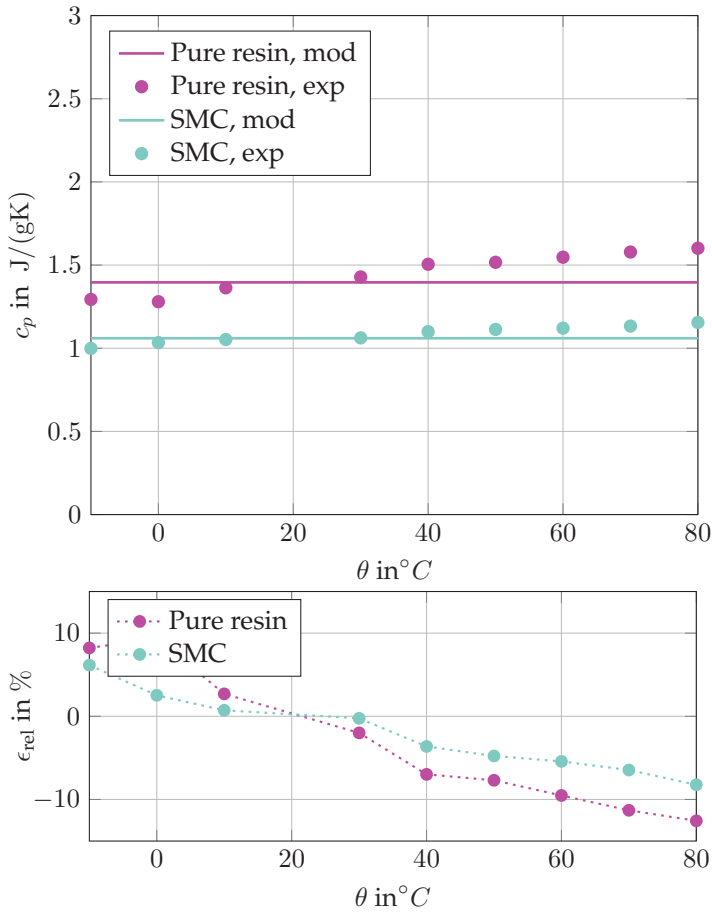


**Figure 5.3:** Heat capacity  $c_p(\theta)$  of pure resin and SMC over temperature  $\theta$ ; experimental results (mean of all measured specimens), modeled results (constant fit to the experimental data) (upper diagram) and relative error  $\epsilon_{rel}$  (see Equation (5.1)) (lower diagram).

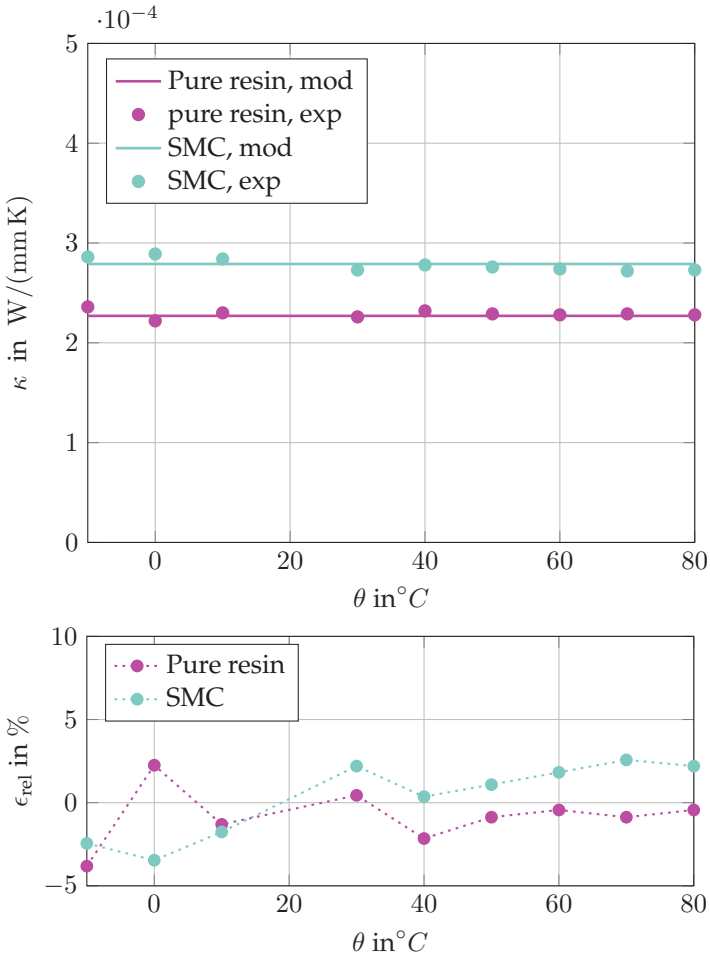


**Figure 5.4:** Thermal conductivity  $\kappa(\theta)$  (in plate thickness direction) of pure resin and SMC over temperature  $\theta$ ; experimental results (mean of all measured specimens), modeled results (constant fit to the experimental data) (upper diagram) and relative error  $\epsilon_{rel}$  (see Equation (5.1)) (lower diagram).

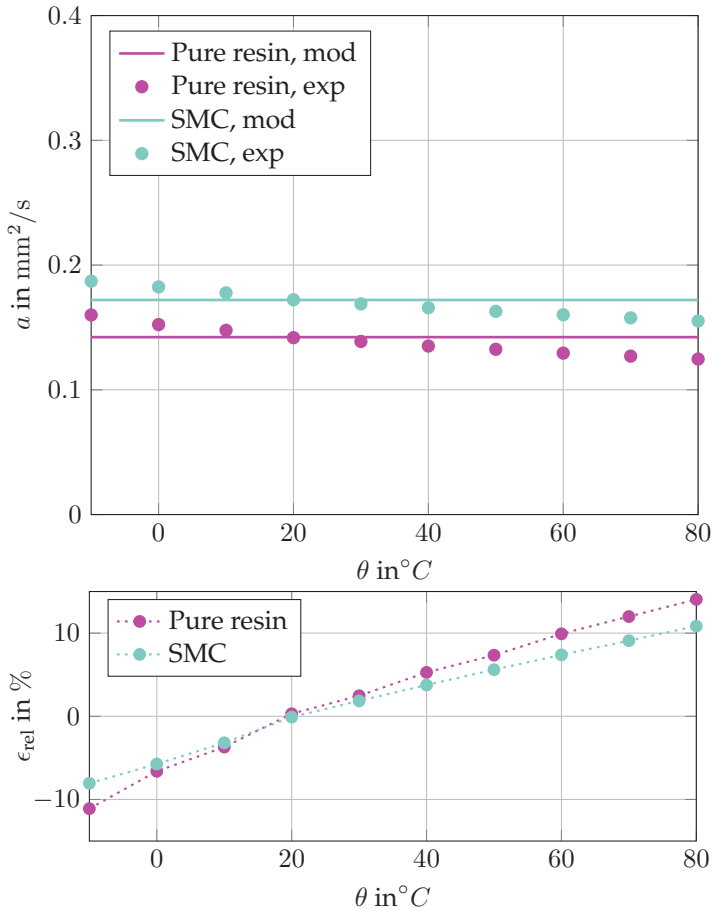


**Figure 5.5:** Thermal diffusivity  $a(\theta)$  (in plate thickness direction) of pure resin and SMC over temperature  $\theta$ ; experimental results (mean of all measured specimens), modeled results (calculated by the fits of  $c_p$  and  $\kappa$ ) (upper diagram) and relative error  $\epsilon_{\text{rel}}$  (see Equation (5.1)) (lower diagram).

### 5.1.3 Temperature-Dependent Coefficients

Analogously to the definition of the Young's modulus in Equation (5.2), the linearly temperature-dependent Young's modulus can be expressed as follows

$$E(\theta) = E'_0 \Delta\theta + E_0 \quad (5.5)$$

where  $E_0$  is the Young's modulus measured at the reference temperature  $\theta_0$ . This leads to

$$E_1(\theta) = E'_{01} \Delta\theta + E_{01}, \quad E_2(\theta) = E'_{02} \Delta\theta + E_{02} \quad (5.6)$$

for the two directions  $\mathbf{n} = \mathbf{e}_1$  and  $\mathbf{n} = \mathbf{e}_2$ . Considering the Ansatz in Equation (3.44)

$$\mathbb{C} = \mathbb{C}_0(1 + C'_0 \Delta\theta) \quad (5.7)$$

leads to

$$C'_0 = \frac{E'_{01}}{E_{01}} = \frac{E'_{02}}{E_{02}}. \quad (5.8)$$

For the thermal expansion coefficient yields as in Equation (3.60)

$$\boldsymbol{\alpha} = (1 + C'_0 \Delta\theta)^{-2} (-C'_0 \mathbb{C}_0^{-1}[\boldsymbol{\sigma}] + \mathbb{C}_0^{-1}[\boldsymbol{\beta}_0]). \quad (5.9)$$

with

$$\boldsymbol{\alpha}_{\sigma 0} = \mathbb{C}_0^{-1}[(-C'_0 \boldsymbol{\sigma} + \boldsymbol{\beta}_0)] \quad (5.10)$$

this leads to for the component  $\alpha_{11}$  to

$$\alpha_{11}(\theta) = \frac{1}{(1 + C'_0 \Delta\theta)^2} \alpha_{11, \sigma 0}, \quad (5.11)$$

where  $\alpha_{11, \sigma 0}$  corresponds to the value of the thermal expansion coefficient at the reference temperature measured by dilatometer. Thus, the course of the temperature-dependent thermal expansion coefficient is defined by the constant  $C'_0$ , taken from the identified temperature-

dependent Young's modulus from the DMA measurements and the thermal expansion coefficient measured at the reference temperature. According to the Ansatz in the thermomechanical material model with temperature-dependent coefficients, heat capacity at constant strain  $c_\varepsilon(\theta)$  is linear in temperature. With the above mentioned assumption of  $c_p \approx c_\varepsilon$  heat capacity in function of temperature reads

$$c_p(\theta) = c'_{p,0}(\Delta\theta) + c_{p,0}, \quad (5.12)$$

with  $\Delta\theta = \theta - \theta_0$ , with the reference temperature  $\theta_0 = 20^\circ\text{C}$ .

Thermal conductivity is still assumed to be constant. Thus for the measured component yields

$$\kappa_{33} = \kappa_{33,0}. \quad (5.13)$$

From the assumptions for heat capacity and thermal conductivity follows for the thermal diffusivity

$$a_{33}(\theta) = \frac{\kappa(\theta)}{\rho c_p(\theta)} = \frac{\kappa_{33,0}}{\rho (c'_{p,0}(\Delta\theta) + c_{p,0})}. \quad (5.14)$$

To identify the parameters of the coefficients assumed to be linear, stiffness and heat capacity, a linear fit using least square method is applied to the experimental data with the constraint, that the value at  $\theta = 20^\circ\text{C}$  corresponds to the reference temperature value  $\xi_{\text{RT}}$ . For the Young's moduli of SMC the additional constraint of Equation (5.8) is included. The thermal conductivity is the same as for the model with constant coefficients and thus set to the room temperature value for the entire temperature range. The derived quantities thermal expansion and thermal diffusivity are calculated using these identified parameters according to Equations (5.11) and (5.14). The constant reference temperature and mass density correspond to those of the

material model with constant coefficients.

Figures 5.6 to 5.10 show for each individual parameter the experimental data, the modeled values and the relative error as defined in Equation (5.1) for the different SMC directions and pure resin over temperature.

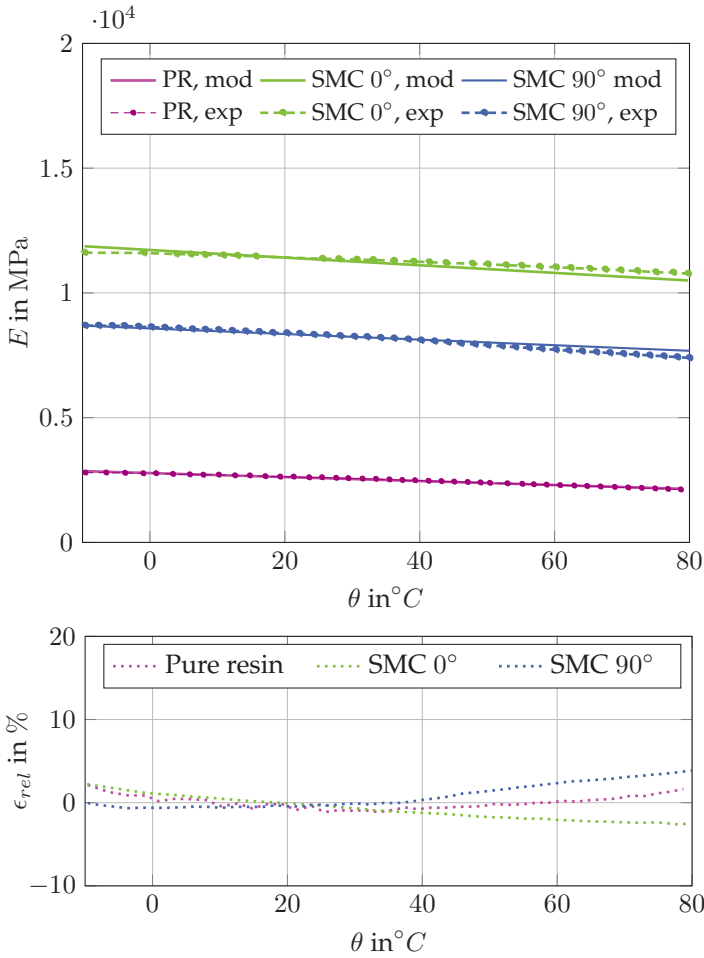
Young's modulus (Figure 5.6), shows for pure resin error of maximum 2%. For the two SMC directions the error remains under 4%. Here, the Young's modulus is slightly overestimated in the 90°-direction and slightly underestimated in the 0°-direction for high temperatures due to the constraint of Equation (5.8). Nevertheless up to a temperature of 50° the error remains under 2%.

Figure 5.7 shows that the principal course of the expansion coefficient for the two SMC directions and pure resin is well matched by the model. However, errors occur in the range of more than 10%, for 90° SMC only at low temperature and for 0° SMC and pure resin also at high temperatures.

The relative error for heat capacity (Figure 5.8) remains below 5% for pure resin and both SMC direction over the entire temperature range. For pure resin it remains even under 2% excluding one value.

For the thermal conductivity (see Figure 5.9) it yields the same as for the parameter identification of the model with constant coefficients. Thus, as already stated in the previous section, for the thermal conductivity (see Figure 5.9), the error remains below 5% for all materials and all temperatures.

The course of thermal diffusivity (Figure 5.10) remains under 5% for SMC in both directions and pure resin over the entire temperature range. The largest error occurs at low temperatures; at high temperatures the error remains under 2%.



**Figure 5.6:** Young's modulus  $E(\theta)$  of pure resin and SMC over temperature  $\theta$ ; experimental results (selected specimens), modeled results (linear fit to experimental data) (upper diagram) and relative error  $\epsilon_{rel}$  (see Equation (5.1)) (lower diagram).

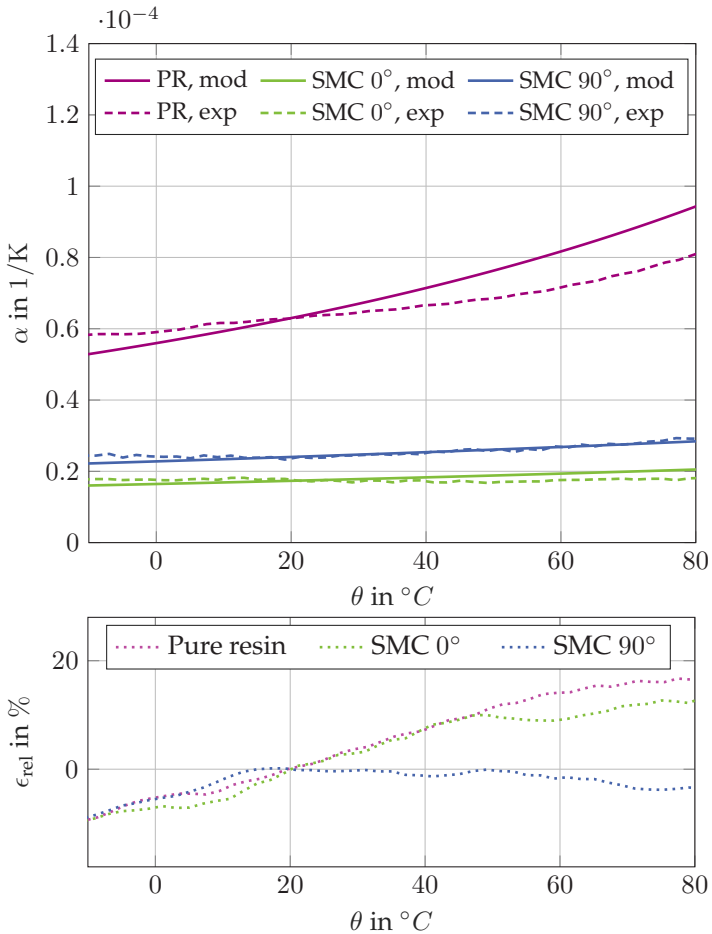


**Figure 5.7:** Thermal expansion  $\alpha(\theta)$  of pure resin and SMC over temperature  $\theta$ ; experimental results (selected specimens), modeled results (calculated from fit values from E) (upper diagram) and relative error  $\epsilon_{rel}$  (see Equation (5.1)) (lower diagram).

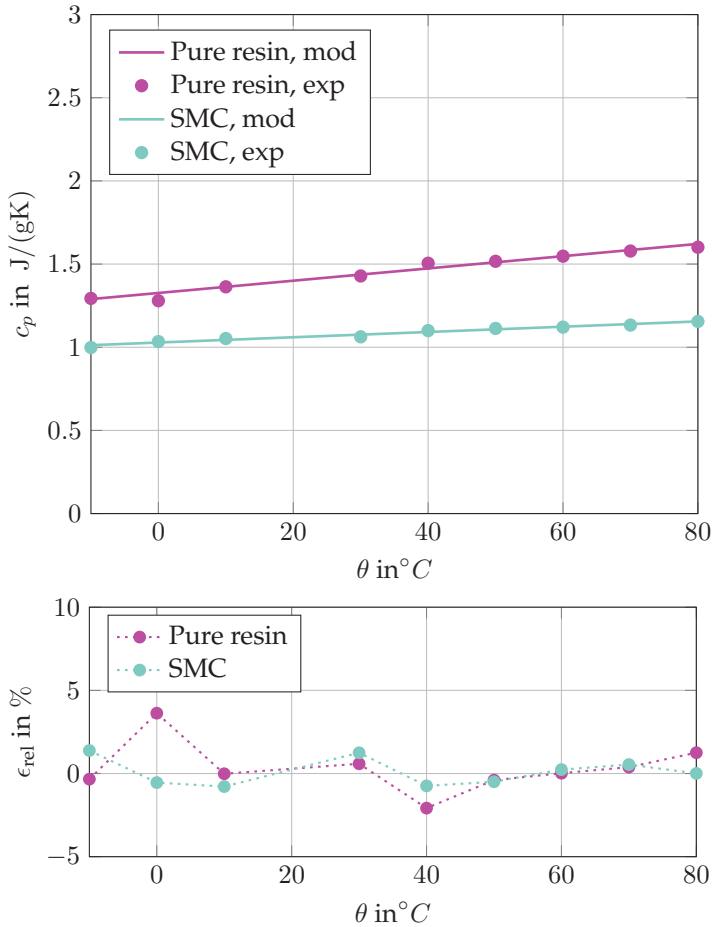


**Figure 5.8:** Heat capacity  $c_p(\theta)$  of pure resin and SMC over temperature  $\theta$ ; experimental results (mean of all measured specimens), modeled results (linear fit to experimental data) (upper diagram) and relative error  $\epsilon_{\text{rel}}$  (see Equation (5.1)) (lower diagram).

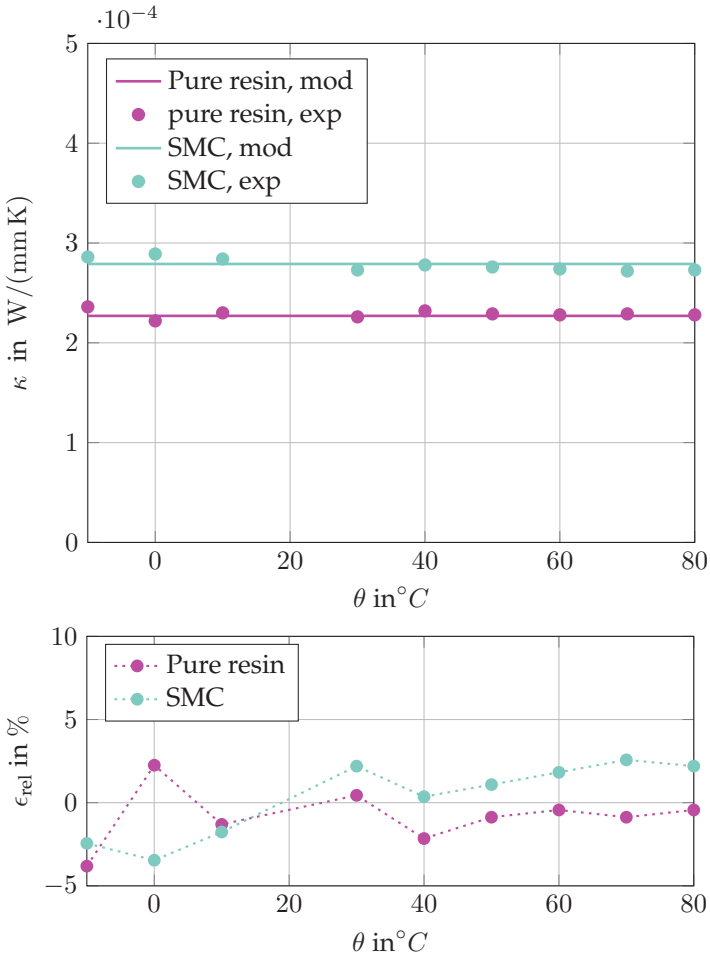


**Figure 5.9:** Thermal conductivity  $\kappa(\theta)$  (in plate thickness direction) of pure resin and SMC over temperature  $\theta$ ; experimental results (mean of all measured specimens), modeled results (constant fit to experimental data) (upper diagram) relative error  $\epsilon_{rel}$  (see Equation (5.1)) (lower diagram).

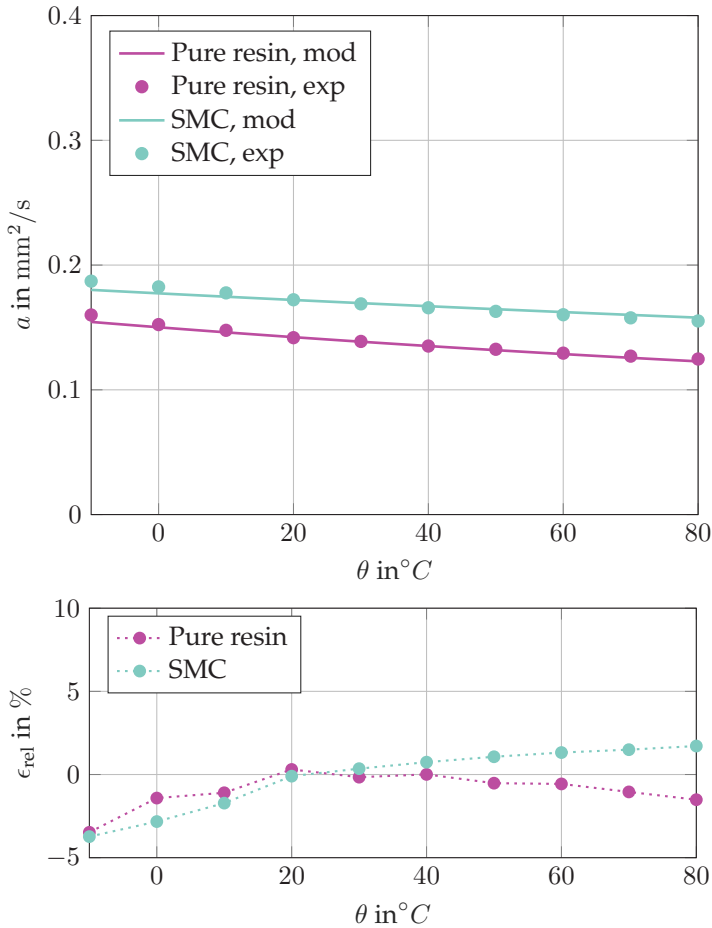


**Figure 5.10:** Thermal diffusivity  $a(\theta)$  (in plate thickness direction) of pure resin and SMC over temperature  $\theta$ ; experimental results (mean of all measured specimens), modeled results (calculated from  $c_p$  and  $\kappa$ ) (upper diagram) and relative error  $\epsilon_{rel}$  (see Equation (5.1)) (lower diagram).

## 5.2 Micromechanical Thermoelastic Model

### 5.2.1 Introducing Remarks

In the following sections the parameter identification of the micromechanical models presented in Section 3.2 is described. The considered material coefficients are stiffness and thermal expansion coefficient and thermal diffusivity or thermal conductivity. Results of the experiments of Section 4.3 at reference temperature are used for this purpose. The microstructure information was delivered by Ludwig Schöttl (Institute of Applied Materials (IAM-WK, KIT), working in the same IRGT in the research area characterization). The microstructure was analysed via micro computer tomography (micro-CT). Here, the averaged orientation tensors over "small" specimens were used (small specimens = specimens of the geometries in Figures 4.9, 4.10a, 4.10b, 4.11, depending on measuring method). This averaged orientation tensor is calculated according to Equations (2.95) and (2.96) with the data from micro-CT and evaluation algorithms identifying fibers from the micro-CT data. Details on this procedure can be found in Pinter et al. (2018) and Schöttl et al. (2020).

As for the thermomechanical parameter identification, the  $0^\circ$ - and  $90^\circ$ -direction of Figure 2.4 correspond to the  $e_1$ - and  $e_2$ -direction, respectively, and the plate thickness direction, perpendicular to the  $0^\circ$ - $90^\circ$ -plane, corresponds to the  $e_3$ -direction.

A relative error is defined as follows

$$\epsilon_{\text{rel}} = \frac{\xi_{\text{mod}} - \xi_{\text{exp}}}{\xi_{\text{exp}}} \quad (5.15)$$

where  $\xi_{\text{mod}}$  is the value of a parameter calculated via the microstructure information and the then identified parameters for an individual specimen and  $\xi_{\text{exp}}$  is the experimental value for this parameter of this specimen. The relative error is considered for each specimen.

## 5.2.2 Stiffness

For the micromechanical modeling of the stiffness tensor, the ansatz introduced in Section 3.2 (Equation (3.55)) is used

$$\mathbb{C}(\mathbf{k}, \mathbf{D}_i, \mathbb{D}_i) = k_1 \mathbb{P}_1 + k_2 \mathbb{P}_2 + k_3 (\mathbf{D} \otimes \mathbf{I} + \mathbf{I} \otimes \mathbf{D}) + k_4 \mathbb{J}[\mathbf{D}] + k_5 \mathbb{D} \quad (5.16)$$

with the parameter set  $\mathbf{k} = (k_1, k_2, k_3, k_4, k_5)$  that is to identify. To determine these five parameters, results of several tensile experiments are used of specimens with known microstructure, i.e. known fiber orientation tensor. Experimental investigations presented in Section 4.3.2 provide here the experimental results for Young's modulus and Poisson's ratio. Microstructure is provided by micro-CT scan as mentioned in Section 5.2.1. With these data, the parameters are optimized with least square minimization to the experimental results with  $n$  values (one value per specimen) for Young's modulus and  $m$  values for Poisson's ratio (there are not for all specimens values for Poisson's ratio). These values correspond to measurements in direction  $\mathbf{n}_i$  (or  $\mathbf{n}_j$ ) on specimen with averaged orientation tensor  $\mathbf{D}_i, \mathbb{D}_i$  (or  $\mathbf{D}_j, \mathbb{D}_j$ ). This can be expressed as

$$\mathbf{k} \text{ from: } \min \left( \sum_{i=1}^n \left( \frac{E_{i,\text{mod}} - E_{i,\text{exp}}}{E_{i,\text{exp}}} \right)^2 + \sum_{j=1}^m \left( \frac{\nu_{j,\text{mod}} - \nu_{j,\text{exp}}}{\nu_{j,\text{exp}}} \right)^2 \right), \quad (5.17)$$

with

$$E_{i,\text{mod}} = E(\mathbf{k}, \mathbf{D}_i, \mathbb{D}_i, \mathbf{n}_i) = E(\mathbb{C}(\mathbf{k}, \mathbf{D}_i, \mathbb{D}_i), \mathbf{n}_i) \quad (5.18)$$

and

$$\nu_{i,\text{mod}} = \nu(\mathbf{k}, \mathbf{D}_i, \mathbb{D}_i, \mathbf{n}_i) = \nu(\mathbb{C}(\mathbf{k}, \mathbf{D}_i, \mathbb{D}_i), \mathbf{n}_i) \quad (5.19)$$

with  $E(\mathbb{C}, \mathbf{n})$  and  $\nu(\mathbb{C}, \mathbf{n})$  as defined in Equation (5.3) and the parameter vector

$$\mathbf{k} = (k_1, k_2, k_3, k_4, k_5). \quad (5.20)$$

The differences between modeled and experimental value of Young's modulus and Poisson's ratio are normalized to the experimental values to have comparable weights of both. For the optimization the solver software Midaco (Mixed Integer Distributed Ant Colony Optimization) is used. Midaco uses a gradient-free, evolutionary algorithm that treats the problem as black-box. Limits for the parameters as well as equality and inequality constraints can be entered (Schlüter et al., 2009). Parts of the implementation are taken from Bauer and Lang (2021) and some tools from Bauer (2021a) are used. Since the parameter  $k_1$ , corresponding to  $3K$  ( $K$ : compression modulus), is indifferent to the optimization, because the strain in the  $e_3$ -direction (plate thickness direction) is not measurable, it is set to a fixed value. This value is estimated via a meanfield methods (Bauer, 2021b). Likewise, no Young's modulus can be determined in the  $e_3$ -direction ( $E_3$ ). In order to ensure that physically meaningful values are obtained, constraints were specified which stipulate that for all specimens the value of  $E_3$  is greater than the pure resin value and smaller than the  $90^\circ$  SMC value. In total, 7 specimens are considered, with values for Young's modulus for all of them and values for Poisson's ratio for 3 of them. This results in the weighting of Young's modulus being slightly greater than that of Poisson's ratio. The optimized parameters  $k$  are given in Appendix A.4. Table 5.1 depicts for all of the seven specimens the experimental values for Young's modulus, the modeled values (calculated with Equation (5.18) and the optimized parameters  $k$ ) and the relative error (see Equation (5.15)). Table 5.2 shows the same for the three specimens and Poisson's ratio. The tables show that absolute errors occur in the range 0% to 20% for both Young's modulus and Poisson's ratio. For most specimens, the error for Young's modulus remains in the range up to about 10%. For one specimen the Young's modulus is significantly underestimated ( $\epsilon_{\text{rel}} \approx -20\%$ ). For Poisson's ratio, the errors for all specimens remain below 10%, whereby the specimen for which Young's modulus has the large error of 20% the Poissons's ratio

error is approximately 5 %.

Performing the parameter identification/optimization procedure without two outlier specimens lead to the results in Tables 5.3 and 5.4. The relative error remains now below 10 % for all considered specimens for Young’s modulus, and below 6 % for all specimens except one. Poisson’s ratio errors occur up to 10 %.

Specimen (dir.)	$E_{\text{exp}}$ in MPa	$E_{\text{mod}}$ in MPa	$\epsilon_{\text{rel}}$ in %
T1f-1-0 (0°)	10200	11539	13.1
T1f-3-90 (90°)	7590	7656	0.9
27f-18-0 (0°)	11400	11358	-0.4
27f-14-90 (90°)	8390	7613	-9.3
28f-2-45 (45°)	10480	10080	3.8
28f-9-0 (0°)	13500	10693	-20.8
27f-3-45 (45°)	7610	8539	12.2

**Table 5.1:** Young’s modulus of SMC; experimental results  $E_{\text{exp}}$ , modeled results  $E_{\text{mod}}$  (calculated by Equation (5.18) with optimized parameters) and relative error  $\epsilon_{\text{rel}}$  (see Equation (5.15)).

Specimen (dir.)	$\nu_{\text{exp}}$ in -	$\nu_{\text{mod}}$ in -	$\epsilon_{\text{rel}}$ in %
27f-14-90 (90°)	0.27	0.30	9.75
28f-2-45 (45°)	0.34	0.33	-3.97
28f-9-0 (0°)	0.38	0.36	-5.87

**Table 5.2:** Poisson’s ratio of SMC; experimental results  $\nu_{\text{exp}}$ , modeled results  $\nu_{\text{mod}}$  (calculated by Equation (5.19) with optimized parameters) and relative error  $\epsilon_{\text{rel}}$  (see Equation (5.15)).

Specimen (dir.)	$E_{\text{exp}}$ in MPa	$E_{\text{mod}}$ in MPa	$\epsilon_{\text{rel}}$ in %
T1f-1 0 (0°)	10200	11165	9.46
T1f-3-90 (90°)	7590	7966	4.95
27f-18-0 (0°)	11400	10878	4.57
27f-14-90 (90°)	8390	7889	-5.97
28-2-45 (45°)	10480	9854	-5.97

**Table 5.3:** Young's modulus of SMC; experimental results  $E_{\text{exp}}$ , modeled results  $E_{\text{mod}}$  (calculated by Equation (5.18) with optimized parameters) and relative error  $\epsilon_{\text{rel}}$  (see Equation (5.15)); parameter identification without outliers.

Specimen (dir.)	$\nu_{\text{exp}}$ in -	$\nu_{\text{mod}}$ in -	$\epsilon_{\text{rel}}$ in %
27f-14-90 (90°)	0.27	0.29	7.2
28f-2-45 (45°)	0.34	0.31	-10.7

**Table 5.4:** Poisson's ratio of SMC; experimental results  $\nu_{\text{exp}}$ , modeled results  $\nu_{\text{mod}}$  (calculated by Equation (5.19) with optimized parameters) and relative error  $\epsilon_{\text{rel}}$  (see Equation (5.15)); parameter identification without outliers.

### 5.2.3 Coefficient of Thermal Expansion

For the micromechanical modeling of the thermal expansion coefficient, the ansatz introduced in Section 3.2 (Equation (3.56)) is used

$$\boldsymbol{\alpha} = k_{\alpha 1} \mathbf{I} + k_{\alpha 2} \mathbf{D}. \quad (5.21)$$

To identify the two parameters  $k_{\alpha 1}$  and  $k_{\alpha 2}$ , several dilatometer experiments are used of specimens with known microstructure, i.e. known fiber orientation tensor. The experimental investigations presented

in Section 4.3.3 deliver here the results for the thermal expansion coefficient. Microstructure is provided by micro ct scan as mentioned in Section 5.2.1. With these data,  $k_{\alpha 1}$  and  $k_{\alpha 2}$  are fitted with least square method to the  $n$  experimental results, measured in direction  $\mathbf{n}_i$  on specimen with averaged orientation tensor  $\mathbf{D}_i$ . This can be expressed as

$$k_{\alpha 1}, k_{\alpha 2} \text{ from: } \min \left( \sum_{i=1}^n (\alpha_{i,\text{mod}} - \alpha_{i,\text{exp}})^2 \right). \quad (5.22)$$

with

$$\begin{aligned} \alpha_{i,\text{mod}} &= \alpha(k_{\alpha 1}, k_{\alpha 2}, \mathbf{D}_i, \mathbf{n}_i) \\ &= \boldsymbol{\alpha}_{i,\text{mod}} \cdot (\mathbf{n}_i \otimes \mathbf{n}_i) \\ &= (k_{\alpha 1} \mathbf{I} + k_{\alpha 2} \mathbf{D}_i) \cdot \mathbf{n}_i \otimes \mathbf{n}_i \end{aligned} \quad (5.23)$$

being the component of the thermal expansion coefficient corresponding to the experimental dilatometer result  $\alpha_{i,\text{exp}}$ . Evaluating Equation (5.23), for example, in  $e_1$ -direction leads to

$$\alpha_{i,\text{mod}} = k_{\alpha 1} + k_{\alpha 2} D_{11} \hat{=} \alpha_{11,\text{exp}}. \quad (5.24)$$

In total, 8 specimens corresponding to 8 experiments (one experiment per specimen) are considered for the optimization. As experimental value, the room temperature value  $\alpha_{\text{RT}}$  (introduced in Section 4.3.1) is taken.

For the optimization python's polyfit algorithm is used (Python NumPy Developers (2022)). For coding tools from Bauer (2021a) are used. The optimization delivers values for  $k_{\alpha 1}$  and  $k_{\alpha 2}$ . These values can be found in Appendix A.4.

Table 5.5 depicts for all of these 8 specimens the experimental values, the modeled values (calculated with Equation (5.23) and the optimized parameters  $k_{\alpha 1}$  and  $k_{\alpha 2}$ ) and the relative error (see Equation (5.15)). The absolute relative error is below 8 % for all specimens except two, where

errors of up to  $-27\%$  and  $16\%$  occur. The parameter identification procedure is in a second step performed without these outlier specimens. The results are depicted in Table 5.6. The error remains now below  $4\%$  for all specimens and for most even below  $3\%$ . This means that for the specimens considered, the model can predict the coefficient of expansion with a maximum error of less than  $4\%$ .

Specimen (dir.)	$\alpha_{\text{exp}}$ in $10^{-5}$ 1/K	$\alpha_{\text{mod}}$ in $10^{-5}$ 1/K	$\epsilon_{\text{rel}}$ in %
T1f-1-0 ( $0^\circ$ )	1.51	1.44	4.39
T1f-2-0 ( $0^\circ$ )	1.62	1.59	1.32
T1f-3-90 ( $90^\circ$ )	2.27	2.45	$-7.76$
27f-18-0 ( $0^\circ$ )	1.76	1.64	6.79
27f-14-90 ( $90^\circ$ )	2.39	2.47	$-3.30$
28f-2-45 ( $45^\circ$ )	2.00	2.01	$-0.68$
28f-9-0 ( $0^\circ$ )	1.46	1.85	$-27.00$
27f-3-45 ( $45^\circ$ )	2.78	2.32	16.40

**Table 5.5:** Thermal expansion coefficient of SMC; experimental results  $\alpha_{\text{exp}}$ , modeled results  $\alpha_{\text{mod}}$  (calculated by Equation (5.23) with optimized parameters and orientation) and relative error  $\epsilon_{\text{rel}}$  (see Equation (5.1)).

Specimen (dir.)	$\alpha_{\text{exp}}$ in $10^{-5}$ 1/K	$\alpha_{\text{mod}}$ in $10^{-5}$ 1/K	$\epsilon_{\text{rel}}$ in %
T1f-1-0 (0°)	1.51	1.53	-1.76
T1f-2-0 (0°)	1.62	1.66	-2.43
T1f-3-90 (90°)	2.27	2.33	-2.61
27f-18-0 (0°)	1.76	1.69	3.93
27f-14-90 (90°)	2.39	2.35	1.79
28f-2-45 (45°)	2.00	1.99	0.65

**Table 5.6:** Thermal expansion coefficient of SMC; experimental results  $\alpha_{\text{exp}}$ , modeled results  $\alpha_{\text{mod}}$  (calculated by Equation (5.23) with optimized parameters and orientation) and relative error  $\epsilon_{\text{rel}}$  (see Equation (5.1)); parameter identification without outliers.

As there is no measurement in the  $e_3$ -direction (plate thickness direction), this cannot be taken into account in the optimization. However, it was checked whether evaluation of Equation (5.23) with optimized parameters yields physically reasonable results for the third diagonal component  $\alpha_{33}$ . This means in this case that the values are between the pure resin and the 90° value which is true for all specimens. The non-diagonal components are not measurable either. The evaluation of equation (5.23) provides values for these components that are at least one order of magnitude, mostly more, below those of the diagonal component.

## 5.2.4 Thermal Diffusivity and Conductivity

The ansatz for micromechanical modeling of thermal conductivity is given in Equation (3.57) and reads

$$\kappa = k_{\kappa 1} \mathbf{I} + k_{\kappa 2} \mathbf{D} \quad (5.25)$$

This ansatz can be transferred to the thermal diffusivity, which is related to thermal conductivity (for constant temperature or constant coefficients) by a constant factor. It yields

$$\mathbf{a} = \frac{1}{\rho c_p} \boldsymbol{\kappa}. \quad (5.26)$$

This leads to the micromechanical ansatz for thermal diffusivity

$$\mathbf{a} = k_{a1} \mathbf{I} + k_{a2} \mathbf{D} = \frac{1}{\rho c_p} k_{\kappa 1} \mathbf{I} + \frac{1}{\rho c_p} k_{\kappa 2} \mathbf{D}. \quad (5.27)$$

The parameter identification is performed with the thermal diffusivity, since it is the directly measured coefficient and there is a higher measurement accuracy here. Three specimens with known microstructure were considered here. The identification procedure corresponds exactly to the one described for the thermal expansion coefficient. The identified parameters can be found in the Appendix A.4. Table 5.7 depicts for the three experimental values, the modeled values (calculated with Equation (5.27) and the optimized parameters  $k_{a1}$  and  $k_{a2}$ ) and the relative error (see Equation (5.15)). The relative error remain below 1 % for all of the three specimens.

Specimen (dir.)	$a_{\text{exp}}$ in $\text{mm}^2/\text{s}$	$a_{\text{mod}}$ in $\text{mm}^2/\text{s}$	$\epsilon_{\text{rel}}$ in %
T1f-q-1	0.1736	0.1742	0.33
T1f-q-2	0.1760	0.1756	0.24
28f-q-3	0.1701	0.1700	0.08

**Table 5.7:** Thermal expansion coefficient of SMC; experimental results  $\alpha_{\text{exp}}$ , modeled results  $\alpha_{\text{mod}}$  (calculated by Equation (5.27) with optimized parameters and orientation) and relative error  $\epsilon_{\text{rel}}$  (see Equation (5.1)).

As described before, the only measuring direction here was the plate thickness direction (perpendicular to the  $0^\circ$ - $90^\circ$ -direction). Calculating the other two diagonal components of thermal diffusivity with the identified parameters lead to values that are 4 to 6 times greater than the ones in the measuring direction.

### 5.2.5 Remark on Micromechanical Temperature Dependent Thermoelastic Model

As discussed in Section 3.2.2 no additional parameters are to identify for the micromechanical material model with temperature-dependent coefficients.

## 5.3 Failure Model

The Tsai-Wu failure criterion is applied to the experimental failure data of the uniaxial, equibiaxial and shear experiment. Here, the assumption of orthotropic material behavior is made, whereby the principal direction of material symmetry corresponds to the plate directions ( $0^\circ$ ,  $90^\circ$ , perp.). This assumption is supported by the experimental studies, where the shear strains are negligibly small for biaxial loading and also stated in Trauth (2018). Thus, all planar Tsai-Wu parameters can be identified (see Equation (3.63)).

Although the scattering is considerable, mean values are taken to identify the Tsai-Wu parameters to identify the principle performance of the Tsai-Wu ansatz.

As no compression failure experiments were performed in the scope of this theses, the tension compression ratio of the dissertation Trauth (2018) are taken, where specimens from the same manufacturing process were analysed. She distinguishes between  $0^\circ$  and  $90^\circ$  and for each direction between flow region and charge region. Charge region

corresponds to the grey area in Figure 2.4 in the center (initial placement of SMC semifinished material before hot pressing) and flow region corresponds to the white area besides (which the material reaches during flow during hot pressing). This leads to four different ratios. A comparison of the results of this thesis with the results of the thesis of Trauth shows that the same tendency is observed. A table with the comparable values can be found in Appendix A.5. Thus, for each specimen the corresponding compression failure value is calculated and from these values a mean value for compression in  $0^\circ$  and  $90^\circ$  is computed (flow and charge region here considered together for mean calculation).

From these data, the following components of the failure tensors of the Tsai-Wu criterion can be identified according to Equations (3.64) to (3.67):

- $F_{11} = 2.528 \cdot 10^{-4} \text{ 1/MPa}$
- $F_{22} = 6.396 \cdot 10^{-4} \text{ 1/MPa}$
- $F_{1111} = 2.213 \cdot 10^{-5} \text{ (1/MPa)}^2$
- $F_{2222} = 4.684 \cdot 10^{-5} \text{ (1/MPa)}^2$

To identify the parameter  $F_{1122}$  the equibiaxial experiments are needed. As the experiments are performed equi-path-controlled and the material is anisotropic, the stress state is not equibiaxial (see Table 4.15). Thus, Equation (3.68) is slightly changed to

$$F_{1122} = \frac{1}{2 \sigma_{fb11} \sigma_{fb22}} (1 - \sigma_{fb11} F_{11} - \sigma_{fb22} F_{22} - \sigma_{fb11}^2 F_{1111} - \sigma_{fb22}^2 F_{2222}). \quad (5.28)$$

This results in the following for the parameter  $F_{1122}$ :

- $F_{1122} = -2.451 \cdot 10^{-5} \text{ (1/MPa)}^2$ .

To identify the parameter  $F_{1212}$ , the two variants described in Section 3.3 are applied and compared. Deriving  $F_{1212}$  from the  $45^\circ$  experimental data according to Equation (3.72) lead to

- $F_{1212} = 3.824 \cdot 10^{-5} (1/\text{MPa})^2$ .

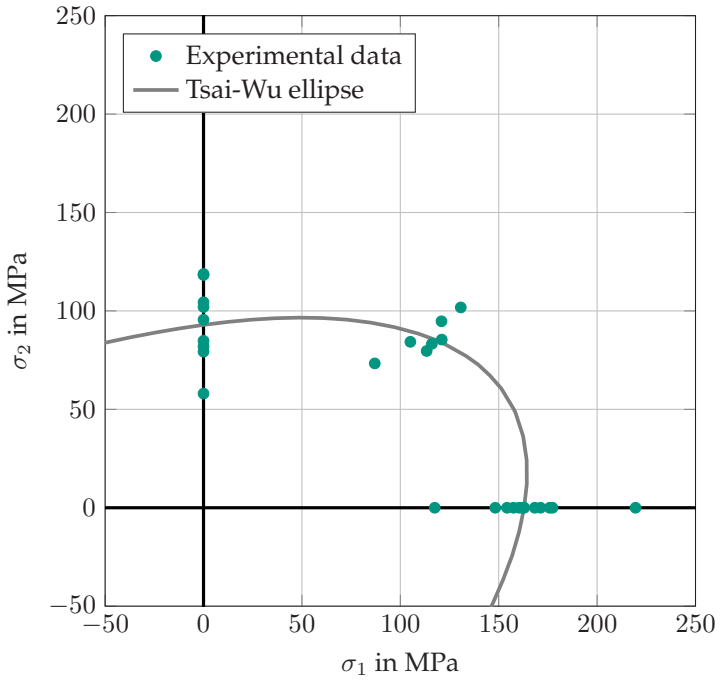
The calculation using the experimental data of the shear experiment and Equation (3.70) lead to

- $F_{1212} = 8.1 \cdot 10^{-5} (1/\text{MPa})^2$ .

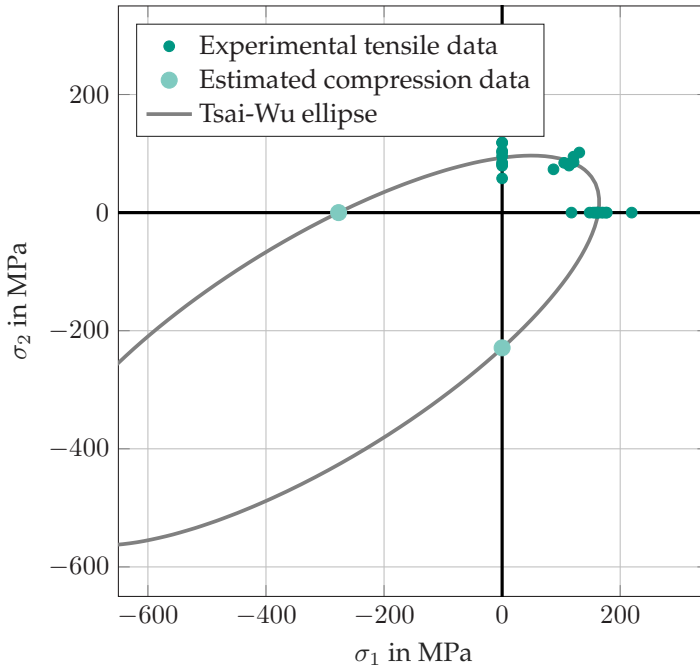
The results are in the same order of magnitude, but differ by about a factor of two. It must be mentioned here that the result of the shear test is critical, since there was a failure in the edges and, in addition, there was not a pure shear stress state. Furthermore, the calculation according to equation (3.72) is very sensitive to slight changes of the other parameters.

Figure 5.11 visualizes the resulting failure surface in the planar principal stress space ( $\sigma_1$ - $\sigma_2$ -plane) for the first quadrant (tension-tension quadrant). The shape of the failure surface resulting from the identified parameters represents an ellipse. In addition, the individual experimental results are plotted in the diagram (all uniaxial and biaxial from Section 4.4.2) scattering around the ellipse.

Figure 5.12 shows a larger section of the ellipse over all four quadrants and additionally the averaged compression failure values estimated from the experiments.



**Figure 5.11:** Failure loci in the principal stress space in the  $e_1$ - $e_2$ -plane, experimental failure stress values from uniaxial and biaxial tensile experiments and failure surface, calculated by the mean values of the experimental failure stresses after the Tsai-Wu failure criterion for the planar, orthotropic case (see Equation (3.63)).



**Figure 5.12:** Failure loci in the principal stress space in the  $e_1$ - $e_2$ -plane, experimental failure stress values from uniaxial and biaxial tensile experiments and estimated compression data and failure surface, calculated by the mean values of the experimental failure stresses after the Tsai-Wu failure criterion for the planar, orthotropic case (see Equation (3.63)).

## 5.4 Micromechanical Failure Model

For the parameter identification of the micromechanical failure model (Section 3.4), some remarks are mentioned here first. Due to the lack of a large enough number of specimens with known microstructure which could be tested until failure, a procedure with comparative specimens was performed. The Young's modulus of specimens (of the geometry

in Figure 4.9) with known microstructure, tested for stiffness only, was compared with the Young's modulus of specimens (of the same geometry) with unknown microstructure, tested for failure. The assumption was made that specimens with similar Young's modulus have also similar microstructure. A comparison of the specimens can be found in Appendix A.5. A comparison procedure was also carried out for the equibiaxial tested cruciform specimens with missing microstructure information. Here, the anisotropy ratio of the biaxial specimen was compared with the anisotropy ratio of two small rectangular specimens, which have very similar (known) microstructure and were oriented in  $0^\circ$  and  $90^\circ$ . In total, 5 uniaxial and 2 biaxial specimens with matching properties (Young's modulus and anisotropy ratio, respectively) were found.

For the uniaxial specimens the same tension compression relation taken from Trauth (2018) is used as described in the previous section. Thus, the four different factors connecting compression to tension are applied to the experimental tensile data for each individual specimen. Thus, a slight microstructure information is included for tension-compression ratio with the assumption that microstructure is similar in same plates with distinction in  $0^\circ$ -flow,  $0^\circ$ -charge,  $90^\circ$ -flow,  $90^\circ$ -charge. The assumption is supported by the comparison of the tendency of the failure stresses depicted in Table A.5 in Appendix A.5.

The shear experiment is not considered for the parameter identification due to a lack of comparable microstructure information and uncertainties in the experimental result.

Thus, with the experimental failure data of the above mentioned specimens, the above mentioned assumptions and the microstructure, the parameters of the micromechanical failure model can be identified according to Equations (3.74) and (3.73)

$$\mathbb{F} = k_{f1}\mathbb{P}_1 + k_{f2}\mathbb{P}_2 + k_{f3}(\mathbf{D} \otimes \mathbf{I} + \mathbf{I} \otimes \mathbf{D}) + k_{f4}\mathbb{J}[\mathbf{D}] + k_{f5}\mathbb{D}, \quad (5.29)$$

$$\mathbf{F} = k_{f6}\mathbf{I} + k_{f7}\mathbf{D}. \quad (5.30)$$

As  $k_{f1}$  is not independently sensitive from  $k_{f2}$  for the considered experimental data, the two parameters are merged as a new parameter  $k_{f12}$ . In Appendix A.5 selected components of  $F_{ijkl}$  are given in written out form, which clarifies the relationships.

The parameters are identified with a least square method using the solver software Midaco (Schlüter et al., 2009) as described in Section 5.2.2. The parameters were identified with the modeled values from Equations (5.30) and (5.29) and the corresponding experimental values calculated according to Equations (3.64) to (3.67) and (5.28). The resulting values for the parameters are given in Appendix A.4. With these parameters the full failure surface in the planar principal stress space can be derived from the microstructure.

Figure 5.13 shows the ellipses that result from the different microstructures of the specimens that served for the identification and the corresponding experimental failure results. The markers of the experimental failure stress value and the corresponding ellipse, calculated with the microstructure corresponding to the specimen have the same color. For each ellipse there are at least two experimental points, the tensile failure stress value and the corresponding calculated compression failure value. For some ellipses, there is an additional experimental point at the biaxial stress state, because the same comparative specimen with known microstructure is taken. From this visualisation the matching of model and experiment and the variety of different ellipse shapes due to microstructure can be assessed. Table 5.8 depicts the experimental tensile and after Trauth (2018) calculated compression failure stress values, the modeled values and the relative error as defined in Equation (5.15). The modeled values are calculated using the micromechanical ansatz for failure (Equation (5.30) and (5.29)), and evaluating the Tsai-Wu criterion (Equation (3.62)) for the corresponding stress state. For most

specimens the error remains below 10%, most even less and a few above. One outlier is identifiable, with an error of 45%.

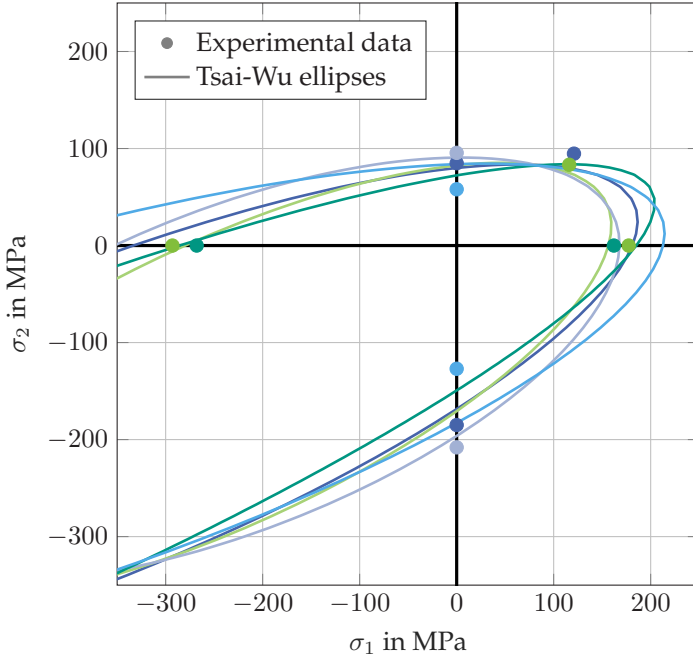


**Figure 5.13:** Failure loci in the the  $e_1$ - $e_2$ -plane, experimental failure stress values and failure surface, calculated by the microstructure and the identified parameters of the micromechanical failure model. The same color indicates the corresponding failure ellipses and experimental failure values.

Specimen	$\sigma_{f, \text{exp}}$ in MPa	$\sigma_{f, \text{mod}}$ in MPa	$\epsilon_{\text{rel}}$ in %
26f-19-90	85	80	5.8
26f-19-90	-185	-168	9.2
26f-37-0	177	156	11.9
26f-37-0	-293	-280	4.4
26f-18-90	58	84	-44.7
26f-18-90	-127	-183	-44.1
26f-36-0	162	185	-14.2
26f-36-0	-268	-285	-6.3
26f-33-90	96	91	5.1
26f-33-90	-208	-196	5.8

**Table 5.8:** Failure stress  $\sigma_f$ . Experimental results  $\sigma_{f, \text{exp}}$  (real experimental data for tensile failure stress (positive values) and from experimental tensile values estimated values for compression tensile stress (negative values)), modeled results  $\sigma_{f, \text{mod}}$  (calculated by micromechanical failure model with optimized parameters and orientation) and relative error  $\epsilon_{\text{rel}}$  (see Equation (5.1)).

## 5.5 Summary and Discussion of Results

### 5.5.1 Thermoelastic Model

In the following, the parameter identification results of the two presented thermoelastic material models (with constant coefficients and with temperature-dependent coefficients) are summarized, analyzed and compared. Causes for weaknesses are identified and the suitability for application is discussed. Table 5.9 summarizes the results for both models. For each parameter and both models, the maximum absolute values of the relative error (see Equation (5.1)) of the entire temperature range are depicted for pure resin and SMC (partly in

different directions:  $E$  and  $\alpha$  in  $0^\circ$  and  $90^\circ$ ,  $\kappa$  and  $a$  in plate thickness direction). Additionally, the temperature range in which the absolute relative error remains below 5 % is given .

From the table it can be seen that the model with constant coefficients matches the material behavior for most parameters only in a temperature range around reference temperature (corresponding here to room temperature). Only the relative errors of the thermal expansion coefficient of  $0^\circ$ -SMC and the thermal conductivity for SMC and pure resin remain under the 5 % for the entire temperature range. For other parameters errors of up to 25 % for pure resin and up to 20 % for SMC occur. The model with temperature-dependent coefficients shows a better matching for almost all parameters. All parameters except thermal expansion coefficient remain under 5 % for the entire temperature range. For SMC the values remain even below 4 %. It can be concluded that the model with temperature-dependent coefficients describes the real material behavior very well.

The additional assumption of Equation (3.44), leading to the constraint of Equation (5.8), lead to a slight underestimation of Young's modulus in  $0^\circ$ -direction and a slight overestimation in  $90^\circ$ -direction for high temperatures. Without this constraint, the Young's modulus' error would be even lower (below 2 %). But also with this assumption the error remains small (below 4 %). The advantage of this assumption is a simplification regarding the parameter identification, reducing the number of parameters from 58 to 38 for the fully 3D anisotropic case. And an error of below 4 % is still acceptable. The higher error values for thermal expansion occur as no direct fit was applied, but instead the temperature dependence was calculated using the fitted values from Young's modulus fit according to Equation (5.11) and (5.8). A direct fit, (not taking  $C'_0$  from  $E$  fit, see Equation (5.8)) would lead to smaller errors. This means, that the relation between Young's modulus and thermal expansion coefficient can not be fully represented. However, the principal course and the difference of the course of the different

SMC directions and pure resin of the modeled and experimental temperature-dependent coefficients of thermal expansion match very well (see Figure 5.7).

	Constant coefficients			Temp. dep. coefficients		
	$ \epsilon_{rel,max} $ in %	Temp. range for $ \epsilon_{rel}  < 5\%$ in °C		$ \epsilon_{rel,max} $ in %	Temp. range for $ \epsilon_{rel}  < 5\%$ in °C	
$E_{PR}$	24.8	−1	to 35	1.7	full	
$E_{SMC0^\circ}$	6.0	−10	to 72	2.6	full	
$E_{SMC90^\circ}$	13.0	−10	to 46	3.6	full	
$\alpha_{PR}$	26.0	5	to 37	17.3	1	to 31
$\alpha_{SMC0^\circ}$	3.9	full		12.2	10	to 35
$\alpha_{SMC90^\circ}$	18.4	−10	to 35	8.5	3	to 80
$\kappa_{PR}$	3.8	full		3.8	full	
$\kappa_{SMC}$	2.6	full		2.6	full	
$c_{pPR}$	9.4	10	to 35	3.6	full	
$c_{pSMC}$	8.2	−5	to 50	1.4	full	
$a_{PR}$	14.1	5	to 35	3.5	full	
$a_{SMC}$	10.8	5	to 45	2.8	full	

**Table 5.9:** Maximum absolute value of relative errors  $\epsilon_{rel,max}$  (see Equation (5.1)) and temperature range with an absolute relative error below 5 % for all thermoelastic material parameters for the material model with constant coefficients (Section 5.1.2) and the material model with temperature-dependent coefficients (Section 5.1.3). "full" indicates full temperature range.

## 5.5.2 Micromechanical Thermoelastic Model

In the following, the parameter identification of the micromechanical thermoelastic model (Section 5.2) is summarized and discussed for the different parameters. Table 5.1 and Table 5.5 show that large relative errors between model and experimental results up to 20 %

can occur for Young's modulus and for thermal expansion coefficient. Table 5.3 and in particular Table 5.6 show that excluding some outliers can lead to better results. For Young's modulus errors of up to 10 % remain. For thermal expansion coefficient, the errors remain below 4 %. This means that thermal expansion coefficient can be predicted with the micromechanical model and the optimized parameters (without outliers) with an accuracy of 4 %, which is a good result.

There are several possible reasons for errors for the occurring errors. One possibility is that the linear approach cannot represent real material behavior with sufficient accuracy. Another possibility is that it is not optimum to consider the microstructure data averaged over an entire sample. Maybe the fiber orientation is not homogenous within one specimen and the specimen size over which is averaged could play a role.

One likely important reason is that the assumption of a homogeneous fiber volume fraction in the material does not hold. Trauth (2018) analyzed the fiber volume content and found that it varies between 21.5, vol% and 28.0 vol%. This could also be a reason for the outliers. There could be fiber accumulations or fiber gaps in these specimens. The fact that the outliers in stiffness and thermal expansion coefficient occur at the same specimens, with the same shift to fiber and resin properties, respectively, supports this supposition. Measurement inaccuracies, especially for Poisson's ratio, may also be a factor, leading to higher errors for stiffness (Young's modulus and Poisson's ratio) than for thermal expansion.

The evaluation of errors between experiment and model for thermal diffusivity yields that here occur only very small errors below 1%. It must be noted that the optimization was performed for only 3 samples and measured values. As previously described, the only measurement direction here was the plate thickness direction (perpendicular to the 0°-90°-direction). The microstructure in this direction varies only slightly. Therefore, the points for the linear fit are very close to each other. This

can lead to larger errors for more strongly varying microstructure in the other directions, which could not be validated.

For all tensorial material coefficients, all components can be calculated using the identified/optimized parameters and microstructure information (FOT). For the measurable parameters/components, the accuracy can be validated.

### 5.5.3 Failure Model

Using the mean values of the uniaxial tensile experiments of this thesis combined with the tension-compression ratio of Trauth (2018), the equibiaxial experiments and the  $45^\circ$ -tensile tests or shear test, all parameters of the Tsai-Wu failure criterion were determined for the planar case and the assumption of orthotropic material behavior.

The latter assumption is supported by equibiaxial tensile experiments (with only normal tensile stress), where the strain has been measured by DIC. The values of the shear components of the strains were magnitudes below the normal strain components. Also Trauth (2018) postulated this assumption. The planar stress case corresponds to the experiments performed in this thesis.

The appearance of an elliptic shape (and not a hyperbolic) in the planar principal stress space shows that the Tsai-Wu failure criterion is principally suitable for the description of failure for SMC.

In the scope of this thesis only experiments in the tensile-tensile quadrant have been performed. Additionally the uniaxial compression experiments of Trauth (2018) were available. According to Figure 5.12 in the compression-compression biaxial stress state large failure stresses of above 600 MPa would occur according to the model with the identified parameters. The shape of the ellipse is very sensitive to changes in the tension-tension and uniaxial compression failure stress values. Thus, it must be considered critically, if these failure stresses would be reached in experiments. Furthermore large scattering occurs for failure stresses.

Thus, with only the failure criterion derived by the mean values, no reliable failure stresses can be predicted. Microstructure considerations are essential here.

### **5.5.4 Micromechanical Failure Model**

Using the assumptions described in Section 5.4, it was possible to estimate the parameters of the micromechanical failure model. Table 5.8 shows that the errors between modeled and experimental failure stress values remain below 10% for most specimens. Compared to a maximum relative difference to the mean value of 25% (outliers excluded) of the experimental data it represents an improvement. One outlier can be identified in Table 5.8 with a large error of 40%. Here, the influence of defects plays an important role, because these defects can cause early failure independent of the general microstructure. Quality assurance can be a solution here to identify outliers before. Figure 5.13 visualizes the matching of model and experiment. Furthermore, this diagram visualizes the variety of the different ellipses created by the optimized parameters and the microstructure of considered specimens.



## Chapter 6

# Applications

## 6.1 Thermoelasticity

In order to combine and validate all results, all findings are applied to a sample SMC specimen with known microstructure. For this specimen, the material parameters are calculated via the material models with the optimized parameters and measured by different testing devices and subsequently compared. To measure all of the parameters, the specimen has to match into different testing devices. Thus, the specimen must be machined between the different experiments. Figure 6.1 shows the different stages of the specimen and indicates which testing device belongs to the respective step. With the known microstructure and the micromechanical material model, the directional material coefficients (stiffness tensor, thermal expansion coefficient, thermal diffusivity) are determined. The experimental assessable parameters are derived from the tensorial coefficients. As the considered specimen is a  $90^\circ$ -specimen, these are Young's modulus  $E_2$ , Poisson's ratio  $\nu_{21}$ , thermal expansion coefficient  $\alpha_{22}$ , and thermal diffusivity  $a_{22}$ . For heat capacity as non-directional material coefficient the identified averaged value is considered.

Exemplarily, the full modeled tensorial coefficient of thermal expansion at room temperature  $\alpha_{RT}$  is given:

$$\begin{pmatrix} 1.75 \cdot 10^{-5} & 8.15 \cdot 10^{-9} & -1.32 \cdot 10^{-7} \\ & 2.24 \cdot 10^{-5} & 1.46 \cdot 10^{-7} \\ \text{sym} & & 2.88 \cdot 10^{-5} \end{pmatrix} 1/\text{K}, \quad (6.1)$$

where the second diagonal component corresponds to the measured value ( $\alpha_{22}$ ). Table 6.1 depicts the modeled and the experimental values at reference temperature and the relative error (see Equation (5.15)). For all parameters except heat capacity and thermal conductivity the relative error is below 3%. The reason for this higher error lies probably in measuring inaccuracies and reproducibility weakness of the LFA method for heat capacity and thus also for thermal conductivity which is derived from heat capacity. Also the temperature-dependent behavior of the parameters is considered. For Young's modulus, Equation (5.6) is used with the value for  $E_0$  calculated by the micromechanical model (see Table 6.1).  $E'_0$  is determined with Equation (5.8) with  $C'_0$  determined in the thermoelastic parameter identification being not microstructure dependent. For thermal expansion, Equation (5.11) is used with  $\alpha_0$  calculated by the micromechanical model (see Table 6.1). This is valid because the applied stress in the dilatometer measurement is negligible small. Temperature-dependent thermal diffusivity is evaluated according to Equation (5.14). Figure 6.2 shows for Young's modulus and thermal expansion coefficient experimental data, the modeled values and the relative error as defined in Equation (5.1). The principle trend is matched well for both parameters. Only at the edges of the considered temperature range errors of up to 10% occur, in a wide temperature range (0°C to 70°C) the error remains below 5% for both parameters. Figure 6.3 shows the modeled and the experimental thermal diffusivity over temperature and the relative error. For the entire temperature range the error remains below 5%.

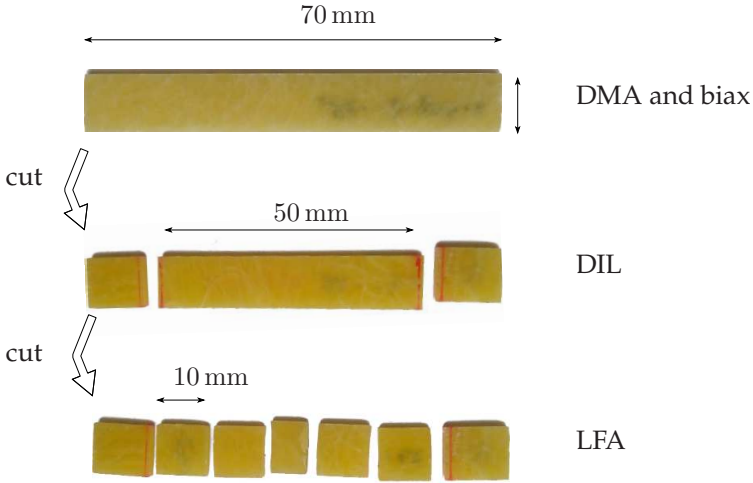
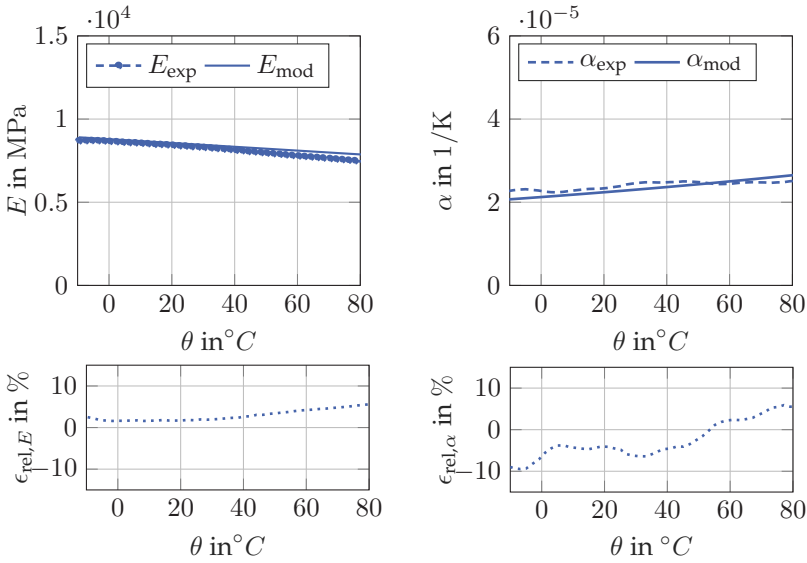


Figure 6.1: Sample validation specimen.

	$\xi_{RT,exp}$	$\xi_{mod}$	$\epsilon_{RT,rel}$ in %
$E_{RT}$ in MPa	8420	8564	1.7
$\nu_{RT}$ in -	0.30	0.29	-2.7
$\alpha_{RT}$ in $10^{-5}$ 1/K	2.31	2.24	-3.0
$a_{RT}$ in $mm^2/s$	0.170	0.172	1.1
$c_{p,RT}$ in J/(gK)	1.21	1.06	-11.6
$\kappa_{RT}$ in $10^{-4}$ W/(mmK)	3.12	2.79	10.6

Table 6.1: Experimental and modeled values at RT and relative error of the different material parameters for the validation specimen.



**Figure 6.2:** Young's modulus  $E$  and thermal expansion coefficient  $\alpha$  of validation specimen over temperature  $\theta$ ; experimental results and modeled results (upper diagrams) and relative error  $\epsilon_{rel}$  (see Equation (5.1)) (lower diagrams).

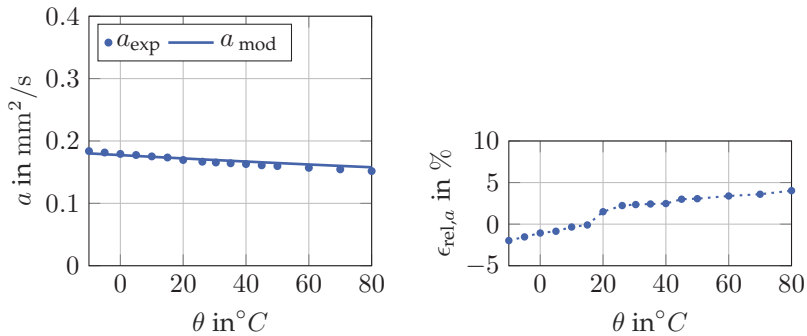


**Figure 6.3:** Thermal diffusivity  $a$  of validation specimen over temperature  $\theta$ ; experimental results and modeled results (left diagram) and relative error  $\epsilon_{rel}$  (see Equation (5.1)) (right diagram).

## 6.2 Failure

Two sample specimens were considered for the validation of the micromechanical failure model. The geometry of the specimens corresponds to Figure 4.9. Using the known microstructure of the specimens and the micromechanical model for (Equations (3.74) and (3.73)), the planar components of the Tsai-Wu strength tensors are calculated. The planar failure ellipse is determined. Evaluating Equation (3.62), for the load case which is here uniaxial tension leads to the modeled failure stress values. The failure stress values were also determined experimentally. Figure 6.4 shows for both considered specimens the failure ellipse, determined by the micromechanical model and the known microstructure, and the corresponding experimental failure values in the same color, respectively. For one of the two specimens (the one loaded in  $e_2$ -direction), modeled and experimental failure stress match well, for the other one early failure in the experiment occurred. The relative errors between model and experiment is approximately 5 % and 20 % respectively for the failure stress values.

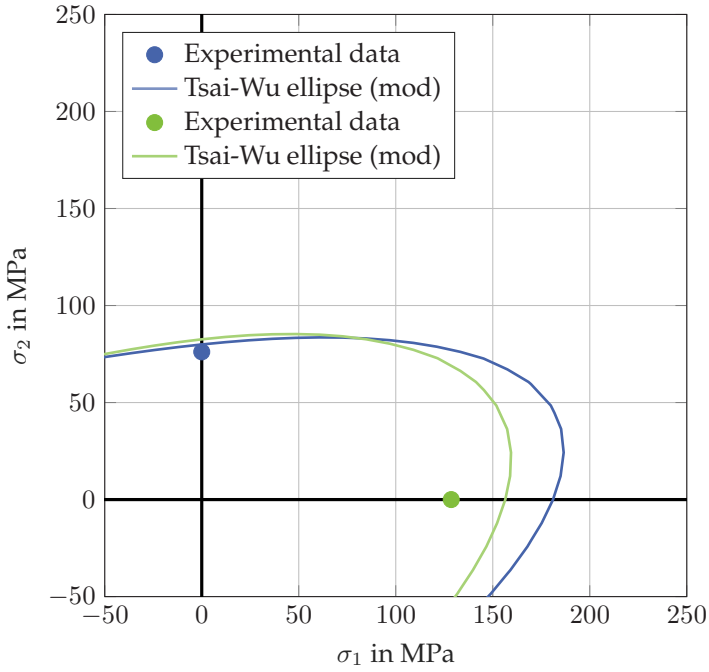


**Figure 6.4:** Failure loci in the the  $e_1$ - $e_2$ -plane, experimental failure stress values of the validation specimens and failure surface (Tsai-Wu ellipse), calculated by micromechanical model and the known microstructure of the validation specimens.

## Chapter 7

# Summary and Conclusion

As stated in Section 1.2 the overall objective of this thesis is to model and to experimentally characterize the anisotropic temperature-dependent thermomechanical behavior of SMC composites on the macroscale, taking into account the microstructure. In the following, the results of these tasks are summarized and concluded. The results are structured along the main subjects, which are represented by the chapters of this work: Firstly, the material model development (Chapter 3), secondly a detailed experimental investigation (Chapter 4), thirdly, the combination of both, to identify the material parameters and to validate the model (Chapter 5) and finally the application on sample specimens (Chapter 6).

Two thermodynamically consistent material models for thermoelasticity are presented: one with constant material coefficients and one with temperature-dependent coefficients. The considered material coefficients are heat capacity, stiffness/ compliance, thermal expansion/ thermal stress, thermal conductivity. For the first model, all of these material coefficients are assumed to be constant, in particular independent of temperature. For the second one, the material coefficients are expressed as functions of temperature, starting with the assumption that heat capacity and stiffness are linear in temperature. This leads to a  $1/\theta^2$  dependence in temperature of the thermal expansion coefficient. Thermal conductivity is still assumed to be constant. These assumptions were made in close accordance

with preliminary experimental studies. The number of parameters which can be more than one per coefficient for the fully anisotropic 3D case is analyzed and the reduction of parameters for special cases is considered.

In a second step the microstructure is taken into account. The overall assumption is that all directional material coefficients (of the thermoelastic material model with constant coefficients) are linear in terms of fiber orientation tensors. In particular this means that the stiffness tensor is expressed linear in terms of fiber orientation tensors of kanatani 3rd kind of second and fourth order, which reduces the number of parameters from 21 to 5. For the coefficient of thermal expansion and for the thermal diffusivity or conductivity, this assumption leads to 2 parameters instead of 6. Here, these two coefficients are expressed linearly as a function of the 2nd order fiber orientation tensor of kanatani 3rd kind. The micromechanical ansatz includes the assumption of a homogeneous fiber volume content distribution. The approach is also applicable for the model with temperature-dependent coefficients. Here, the parameter value calculated by means of the micromechanical model corresponds to the reference temperature value.

For failure modeling a Tsai-Wu ansatz is chosen, considering only the behavior at room temperature. The general 3D fully anisotropic case is considered and as special case the planar, orthotropic case, where the number of parameters reduces to 6.

Here, as for the thermoelastic model, in a second step the microstructure is taken into account. Now, the fully anisotropic case is considered again. The assumption is, similar as for the thermoelastic parameters, that the Tsai-Wu strength tensors are linear in orientation tensors. They are expressed in terms of kanatani 3rd kind orientation tensors of fourth and second (fourth order strength tensor) or only second order (second order strength tensor). The number of parameters is reduced from 27 to 7.

Detailed experimental investigations of the SMC composite and partly the pure resin material were performed with several testing devices to characterize the full thermoelastic material behavior as well as the damage and failure behavior. On the one hand, the results of the experimental investigations in themselves represent an added research value. On the other hand, they serve as a basis for the parameter identification of the models described above.

The investigated thermoelastic material parameters are Young's modulus, Poisson's ratio, thermal expansion, heat capacity, thermal conductivity, and thermal diffusivity. Due to different required specimen geometries the parameters are measured in different directions. The first three mentioned are measured in the  $0^\circ$ - $90^\circ$ -plane, the latter two in the thickness direction of the plate. For heat capacity as scalar parameter the measuring direction doesn't play a role. All of the parameters (except Poisson's ratio) were determined in dependence of temperature in a considered range of  $-10^\circ\text{C}$  to  $80^\circ\text{C}$ . Thermal expansion coefficient for SMC measured in  $0^\circ$ -direction and thermal conductivity show an almost constant behavior. All other parameters exhibit a significant temperature dependence of up to 20% relative change of the parameter values between the edges of the temperature range. Statistical considerations are made to assess the scattering of the parameters. The coefficient of variation (CV) of pure resin is maximum 3% for all measured parameters, indicating a high measuring accuracy and reproducibility. The CV of the heat capacity is slightly higher, which is due to the fact that there are limits of the measurement accuracy of the used LFA method for heat capacity. The scattering of the SMC parameters measured in the  $0^\circ$ - $90^\circ$ -plane is higher (CV of approx. 10%) than those of the parameters measured in the plate thickness direction (CV below 10%). The reason here is that the orientation of the fibers in the plate thickness direction can vary much less than in the  $0^\circ$ - $90^\circ$ -plane. Further reason for the scatter of all parameters of SMC probably lies in other microstructure differences,

such as inhomogeneous fiber volume content distribution.

Detailed damage investigation on SMC composite were performed. As a measure for damage, stiffness degradation was considered. To assess the influence of load case and initial anisotropy, uniaxial and biaxial tensile experiments were performed. A testing procedure was used that allowed to distinguish between different mechanical phenomena, so that the differences in stiffness could be clearly attributed to damage. Stiffness degradation of the biaxial and corresponding uniaxial experiments matched well. The summarized result is that the stiffness degradation depends on the initial anisotropy and on the load case (uniaxial load or equibiaxial load), whereas the influence of initial anisotropy is even more pronounced. Stiffness reduces to maximum 80 % of its initial value. Damage is not included in the material model, but the detailed experimental results represent added value in themselves.

Using the same experimental setup the failure behavior was investigated. Results for uniaxial and biaxial tensile failure stresses were found. A high scattering was observed including several outliers. A reasonable explanation is that additional to microstructure variations in fiber orientation and volume content, microdefects play an important role for early failure.

These biaxial damage and failure experiments were possible due to a special cruciform specimen design introduced by Schemmann et al. (2018c) and further investigated in this thesis. The cruciform specimens arms are reinforced by unidirectional carbon tapes which leads to the advantage that no early failure in the arms occur before damage can be observed in the center area.

Finally all experimental results are discussed, compared and related to each other.

The material model and experiments are combined in a parameter identification. Starting with the thermoelastic modeling, the 3D model is evaluated in the directions that correspond to the measured material parameters (for the tensorial coefficients). The pure resin material and SMC in different directions is considered. Because of the stronger variation of fiber orientation and thus varying material properties in the  $0^\circ$ - $90^\circ$  plane, sample specimens are considered here for the corresponding parameters (Young's modulus, Thermal expansion), whereas the mean values are taken for the other parameters. For the material model with constant coefficients, the material parameters are set to the experimental values at room temperature. For the material model with temperature-dependent material coefficients, a linear fit is performed for Young's modulus and heat capacity with the constraint that the value at room temperature is exact (for comparability with the constant coefficient model). Thermal conductivity is still constant. For the thermal expansion coefficient, the values of the linear fit of Young's modulus and the measured room temperature value are combined to calculate thermal expansion over temperature. Thermal diffusivity is calculated using the fits of heat capacity and thermal conductivity. For all material parameters and both models, the error between experimental results and modeled results is evaluated for the entire temperature range ( $-10^\circ\text{C}$  to  $80^\circ\text{C}$ ). The two models are analyzed and compared. The model with constant coefficients is only suitable for temperatures around reference temperature (approx.  $5^\circ\text{C}$  to  $35^\circ\text{C}$ ) to ensure an error below 5%. On the other side, the material model with temperature-dependent parameters provides very good results. The error between experimental and modeled values remains below 5% for both materials (for SMC even below 4%) for the entire considered temperature range for all parameters, except the thermal expansion coefficient. The occurring errors for thermal expansion suggest, that the model cannot represent the relation between Young's modulus and thermal expansion coefficient perfectly. However, the principle course

of the temperature dependence of the coefficient of thermal expansion agrees very well.

For the parameter identification of the micromechanical thermoelastic model, results from the experimental investigations on specimens with known averaged microstructure were used. The microstructure information is taken from micro-CT scans (provided by Ludwig Schöttl from IAM, KIT). Thus, the parameters of the micromechanical model for stiffness tensor (using the experimental results for Young's modulus and Poisson's ratio), thermal expansion and thermal diffusivity or conductivity can be identified. The complete coefficients (i.e. all components of tensors) are thus determined by the optimized parameters of the model and the microstructure. For the measured material parameters the error between modeled value and experimental value is analysed. Excluding outliers, for Young's modulus relative errors of up to 10 % occur, for thermal expansion coefficient, the relative error remains below 4 %. For thermal diffusivity the error is even below 1 %, but here few experimental data were available. Possible reasons for the occurring errors are that the assumption of constant fiber volume content in all samples does not hold and uncertainties exist in the measurement of Poisson's ratio.

For the Tsai-Wu failure criterion under the assumption of orthotropic material behavior and considering the planar stress state, all parameters, i.e. the remaining components of the strength tensors, were determined using the experimental results of the failure experiments of this thesis and tension compression relation of Trauth (2018). The used experiments of this work are uniaxial tensile tests in different directions, one shear experiment and in particular equibiaxial tensile tests with the above mentioned special cruciform specimen design. The identification of the Tsai-Wu parameters provides results that lead to an elliptic representation of the failure surface in the planar principal stress space. This shows that failure behavior of SMC can principally be described by the Tsai-Wu failure criterion. The high scatter of the

experimental data suggests that the microstructure should be taken into account.

Parameter identification of the micromechanical failure material model was not performed directly. However, using assumptions that allow the microstructure to be estimated (for uniaxial and biaxial specimens), it was possible to perform a parameter identification. This leads to a first estimation of the parameters of the micromechanical failure model. Using these parameters, the failure surface in the planar principal stress space can be calculated with the optimized parameters and microstructure. Comparison of the experimental failure stresses and the modeled failure stresses from the model leads to relative errors of up to about 10% for most specimens. Outliers with large errors are present. As mentioned above, a likely reason is that microdefects can lead to early failure, regardless of the overall microstructure of a sample. Quality assurance could be a measure to identify such outliers.

To conclude and validate all investigations, all results are applied to exemplary specimens with known microstructure. One specimen was tested in all testing devices. The directional thermoelastic parameters (Young's modulus, Poisson's ratio, thermal expansion coefficient, thermal diffusivity) were determined using the micromechanical model with the known microstructure and the identified parameters. Those modeled and experimental values are compared and the relative error considered. The relative error is below 3% at room temperature. For almost the full temperature range (0°C to 70°C) the error remains below 5%. For heat capacity the experimental values were compared to the model that was fit to the mean values. Thermal conductivity was derived from heat capacity and thermal diffusivity. Heat capacity and thermal conductivity exhibit larger errors around 10%. The reason is probably as mentioned above the lack of measuring accuracy/reproducibility for heat capacity and (thus also for conductivity) of the LFA method.

For two specimens the failure surface in the planar principal stress space was calculated using the micromechanical failure model. For one of these two specimens the failure stress prediction matches well, for the other one early failure occurred.

Overall, the temperature-dependent thermomechanical material behavior and the failure behavior were completely determined with the help of the material models in combination with known microstructure. The material behavior could be predicted with an accuracy of approximately 95 % for a large part of the material parameters in accordance with the experiments.

## Appendix A

# Appendix

## A.1 Specimen Designation

The specimen names used throughout this thesis are composed of plate name, specimen number, direction and partly on shape information. For rectangular (non quadratic) and bone specimens (Figures 4.7, 4.10a, 4.10b, 4.9, 4.10, 6.1) specimen names are schematically as follows:

$$Pp-n-d,$$

where "P" is the plate designation, "p" is the plate (flow path) variant (f:flow, v:full), "n" is the specimen number, and "d" indicates the direction of the specimen in the plate ( $0^\circ$ ,  $90^\circ$ ,  $45^\circ$ ). For example, the specimen "28f-14-90" is a specimen from plate "28f" which is a plate with long flow path (see Figure 2.4), specimen number is "14" and the length direction is in  $90^\circ$ -direction according to Figure 2.4.

For small quadratic specimens (Figure 4.11) the designation is

$$Pp-q-n,$$

where "q" indicates the quadratic shape.

General specimen designations are sometimes shortened. For example, "flow specimen" means specimen cut from plate with long flow path (Figure 2.4).  $90^\circ$  specimen means for rectangular or bone specimens that the specimen length direction corresponds to the  $90^\circ$ -direction of

the plate. "Small" specimen includes all specimens with dimensions up to 70 mm x 10 mm.

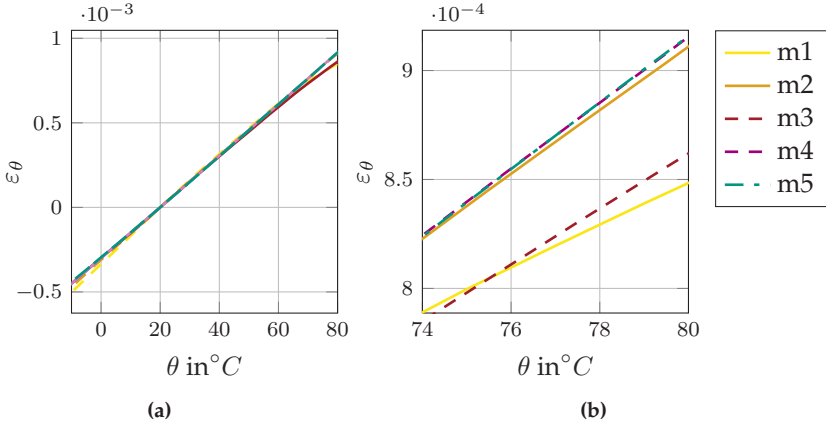
## A.2 Preliminary Study on Dilatometer Measurements

Figure A.2.1 depicts the results for the strain over temperature for several measurement of a sample specimen (Geometry: 35 mm x 8 mm x 2 mm, Orientation: 0°). Reference temperature is room temperature (20 °C), so here the thermal strain is equal to zero. The five measurements (m1 to m5) are as follows:

- m1: no preliminary conditioning, temperature range of -30 °C to 100 °C
- m2: directly after m1
- m3: a few month later than m1 and m2
- m4: directly after m3
- m5: a few month than m4 after conditioning of 1 hour at 100 °C

Figure A.2.1a depicts the a large temperature range of -10 °C to 80 °C. It can be seen that the principle course of the different measurements coincide. But at higher temperature there are slight differences. Figure A.2.1b depicts the corresponding detail. The line of measurement m1 is different from that of m2. The first measurement can be considered as temperature conditioning (during measurement the specimen has a temperature of approximately 100 °C during approximately one hour). m3 is similar to m1, which implies that the conditioning is reversible. m4 and m5 match perfectly and are similar to m2. The conditioning could change the specimen in terms of curing or moisture. That it is reversible suggests that moisture is more likely. In any case, conditioning at 100 °C in the oven ensures reproducibility of

measurements, so all specimens are conditioned by this procedure before measurement.



**Figure A.2.1:** Exemplary specimen (T1f-1-0) several dilatometer measurements,  $\varepsilon_\theta$  ( $=\Delta l/l_0$ ) over temperature  $\theta$ . (a) T1f-1-0 several DIL measurements, (b) T1f-1-0 several DIL measurements, detail.

## A.3 Statistics

### A.3.1 Statistical Quantities

In the following, statistical quantities are defined that are used for data evaluation. Here,  $n$  data value are considered.

The mean  $\bar{x}$  of a quantity  $x$  is defined as the arithmetic average of all data values

$$\bar{x} = \frac{1}{n} \sum_{i=1}^n x_i. \quad (\text{A.1})$$

The median separates the upper and the lower half of all data values. The standard deviation  $\mu$  (std) is defined by

$$\mu = \sqrt{\frac{1}{n-1}(\bar{x} - x_i)^2}. \quad (\text{A.2})$$

Coefficient of variation  $\mu_{\text{rel}}$  (CV) is the standard deviation normalized to the mean value

$$\mu_{\text{rel}} = \frac{\mu}{\bar{x}}. \quad (\text{A.3})$$

The upper and lower quartiles ( $x_{0.25}$ ,  $x_{0.75}$ ) can be described as the medians of the upper and lower half.

The interquartile range (iqr) is the difference between upper and lower Quartile

$$r_{\text{iq}} = x_{0.25} - x_{0.75}. \quad (\text{A.4})$$

More detailed explanations can be found e.g. in Arens et al. (2018).

### A.3.2 Boxplot Representation

Figure A.3.1 shows a boxplot representation for sample data.

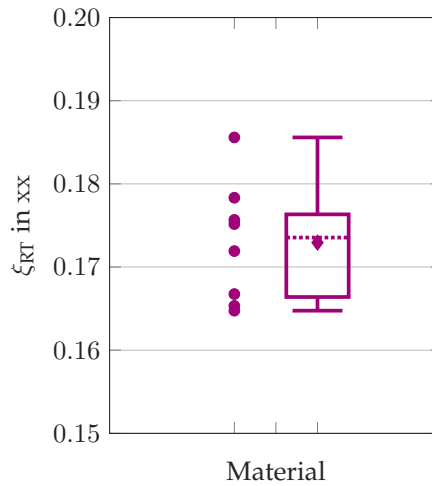


**Figure A.3.1:** Sample boxplot representation:  $\bullet$  = individual experimental data,  $\blacklozenge$  = mean,  $\cdots$  = median, box = lower and upper quartile, T-lines = minimum and maximum or 1.5 iqr

The whiskers (T-lines) are extended to the outerst data point within 1.5 iqr. Data points which are out of this range are defined as outliers. If there are no outliers, the T-lines correspond to maximum and minimum data value (which is the case in Figure A.3.1). More detailed explanations can be found in e.g. Hunter et al. (2012) and Arens et al. (2018).

## A.4 Values of the Optimized Material Parameters

### A.4.1 Thermoelasticity

Tables A.1 and A.2 depict the values of the identified material parameters of the thermoelastic material model with temperature-dependent coefficients (see Section 3.1.2 and Section 5.1.3) for SMC and pure resin.

Parameter	Value	Unit
$E_{1,0}$	11414.89	MPa
$E_{2,0}$	8352.43	MPa
$C'_0$	-0.00134125	1/K
$c_0$	1.060	J/(gK)
$c'_0$	0.00157	J/(gK <sup>2</sup> )
$\alpha_{11,\sigma 0}$	$1.7638 \cdot 10^{-5}$	1/K
$\alpha_{22,\sigma 0}$	$2.392 \cdot 10^{-5}$	1/K
$\kappa_{33,0}$	$2.79 \cdot 10^{-4}$	W/(mm K)

**Table A.1:** Values of the identified material parameters of the thermoelastic material model with temperature-dependent coefficients for SMC.

Parameter	Value	Unit
$E_0$	2619.218	MPa
$C'_0$	-0.00304	1/K
$c_0$	1.3996	J/(gK)
$c'_0$	0.00368	J/(gK <sup>2</sup> )
$\alpha_{\sigma 0}$	$6.299 \cdot 10^{-5}$	1/K
$\kappa_0$	$2.270 \cdot 10^{-4}$	W/(mm K)

**Table A.2:** Values of the identified material parameters of the thermoelastic material model with temperature-dependent coefficients for pure resin.

## A.4.2 Micromechanical Modeling of Thermoelasticity

Table A.3 depicts the values of the identified material parameters of the micromechanical thermoelastic material model (see Section 3.2 and Section 5.2).

Coefficient	Parameter	Value	Unit
Stiffness	$k_1$	27000	MPa
	$k_2$	5969.99	MPa
	$k_3$	994.2627	MPa
	$k_4$	1308.817	MPa
	$k_5$	126.9981	MPa
Thermal expansion	$k_{\alpha 1}$	$2.2901 \cdot 10^{-5}$	1/K
	$k_{\alpha 2}$	$-2.42658 \cdot 10^{-6}$	1/K
Thermal diffusivity	$k_{\alpha 1}$	0.10599	mm <sup>2</sup> /s
	$k_{\alpha 2}$	0.42871	mm <sup>2</sup> /s

**Table A.3:** Values of the identified material parameters of the micromechanical thermoelastic material model for SMC.

### A.4.3 Micromechanical Failure Modeling

Table A.4 depicts the values of the identified material parameters of the micromechanical failure model (see Section 3.4 and Section 5.4).

Coefficient	Parameter	Value	Unit
$\mathbb{F}$	$k_{f12}$	0.000084247	$(1/\text{MPa})^2$
	$k_{f3}$	-0.000001419	$(1/\text{MPa})^2$
	$k_{f4}$	-0.000035460	$(1/\text{MPa})^2$
	$k_{f5}$	0.000025743	$(1/\text{MPa})^2$
$\mathbf{F}$	$k_{f6}$	0.006213415	1/MPa
	$k_{f7}$	-0.001383797	1/MPa

**Table A.4:** Values of the identified material parameters of the micromechanical failure model for SMC.

## A.5 Additional Tables Parameter Identification of Micromechanical Failure Model

Table A.5 depicts the failure stress values taken from Trauth (2018) and measured in this theses under distinct consideration of the two directions,  $0^\circ$  and  $90^\circ$  and flow region and charge region (cf. Figure 2.4).

	Mean $\sigma_{f,AT}$ in MPa	Mean $\sigma_{f,JL}$ in MPa	$\epsilon_{rel}$ in %
FR 0°	183	167	-8.743
CR 0°	167	157	-5.988
FR 90°	101	105	3.960
CR 90°	84	84	0.000

**Table A.5:** Comparison of failure values measured by Trauth (2018) ( $\sigma_{f,AT}$ ) and in this thesis ( $\sigma_{f,JL}$ ) under consideration of flow region (FR) and charge region (CR)

Table A.6 depicts Young’s modulus of specimens with known microstructure (FOT), measured via micro CT scan and Young’s modulus of specimens with known experimental failure stress. In one row are specimens with similar Young’s modulus. For parameter identification of micromechanical failure model the orientation information of these specimens is used for the corresponding destructively tested specimens with thus known failure stress (cf. Section 5.4). The values for Young’s modulus are both taken from measurements with biaxial testing device, respectively.

Comp. scan specimen	Exp. failure specimen	$E_{scan}$ in MPa	$E_{expfail}$ in MPa	$\epsilon_{rel}^E$ in %	$\sigma_{f,expfail}$ in %
28f-16-90	26f-33-90	8150	8288	1.69	96
27f-18-0	26f-37-0	11172	11283	0.99	177
27f-14-90	26f-19-90	8222	8182	-0.49	85
T1f-1-0	26f-36-0	10290	10216	-0.71	162
T1f-3-90	26f-18-90	6860	7010	2.19	58

**Table A.6:** Young’s modulus  $E_{scan}$  of specimens with known microstructure (Comp. scan specimen) and Young’s modulus  $E_{expfail}$  of specimens with known experimental failure stress ( $\sigma_{f,expfail}$ ), and relative difference  $\epsilon_{rel}^E$ .

Table A.7 depicts the values of anisotropy ratio of two uniaxial specimens with similar known microstructure (FOT) and the anisotropy ratio of cruciform biaxial specimens with known failure stress.

$\Gamma_{0/90}$ uniax in -	$\Gamma_{0/90}$ biax in -	$\epsilon_{\text{rel}}^E$ in %
1.39	1.42	2.16 %
1.39	1.43	2.88 %

**Table A.7:** Anisotropy ratio  $\Gamma_{0/90}$  uniax of two uniaxial specimens with similar known microstructure (FOT), anisotropy ratio  $\Gamma_{0/90}$  biax of cruciform biaxial specimens, and relative difference  $\epsilon_{\text{rel}}^E$ .

The following equations (Equations (A.5) to (A.10)) show components of the micromechanical modeled Tsai-Wu strength tensors

$$F_{11} = k_{f6} + k_{f7}D_{11}, \quad (\text{A.5})$$

$$F_{22} = k_{f6} + k_{f7}D_{22}, \quad (\text{A.6})$$

$$F_{1111} = \frac{1}{3}k_{f1} + \frac{2}{3}k_{f2} + 2D_{11}k_{f3} + D_{11}k_{f4} + D_{1111}k_{f5}, \quad (\text{A.7})$$

$$F_{2222} = \frac{1}{3}k_{f1} + \frac{2}{3}k_{f2} + 2D_{22}k_{f3} + D_{22}k_{f4} + D_{2222}k_{f5}, \quad (\text{A.8})$$

$$F_{1122} = \frac{1}{3}k_{f1} + \frac{2}{3}k_{f2} + (D_{11} + D_{22})k_{f3} + 0k_{f4} + D_{1122}k_{f5}, \quad (\text{A.9})$$

$$F_{1212} = 0k_{f1} + 0k_{f2} + 0k_{f3} + \frac{1}{4}(D_{11} + D_{22})k_{f4} + D_{1212}k_{f5}. \quad (\text{A.10})$$

## A.6 Orientation Tensors of Specimens

Table A.8 depicts the components of the fiber orientation tensors of fourth order (kanatani first kind (see Section 2.5.3)) for the considered specimens in Section 5.2 and Section 5.4. The first row shows the order of the 15 independent components.

Specimen	Components of $\mathbb{N}$
	$N_{3333}, N_{3323}, N_{3322}, N_{2322}, N_{2222},$ $N_{3313}, N_{3312}, N_{2312}, N_{2212}, N_{3311},$ $N_{2311}, N_{2211}, N_{1311}, N_{1211}, N_{1111}$
28f-16-90	0.000640, -0.000279, 0.003183, -0.005110, 0.231767, 0.000100, -0.000053, 0.001567, -0.000725, 0.003998, -0.002615, 0.126273, 0.005570, 0.000329, 0.500684
28f-9-0	0.001238, -0.000235, 0.006121, -0.004404, 0.433549, -0.000060, 0.000296, -0.000284, 0.029459, 0.004844, -0.001414, 0.129597, -0.000932, 0.028251, 0.284088
28f-2-45	0.000735, -0.000151, 0.004434, -0.002842, 0.364408, -0.000090, 0.000268, -0.000977, 0.016455, 0.004311, -0.001212, 0.131080, -0.002501, 0.014135, 0.355208
27f-18-0	0.000645, -0.000212, 0.004466, -0.004282, 0.540313, 0.000380, 0.000039, 0.002046, 0.018572, 0.003417, -0.000533, 0.115772, 0.004757, 0.014643, 0.211733
27f-14-90	0.001068, -0.000302, 0.003675, -0.002552, 0.180144, 0.000439, -0.000149, 0.001733, -0.008827, 0.005819, -0.001467, 0.116599, 0.007333, -0.022144, 0.566603
27f-3-45	0.001097, -0.000345, 0.004030, -0.003318, 0.23877, 0.000294, -0.000220, 0.001824, -0.001578, 0.005612, -0.001027, 0.122594, 0.006748, -0.025353, 0.495653
T1f-3-90	0.000107, -0.000006, 0.001735, 0.000028, 0.183037, -0.000142, 0.000357, -0.001193, 0.034552, 0.003762, -0.001413, 0.125909, -0.008407, 0.061640, 0.554045
T1f-1-0	0.000138, -0.000003, 0.003800, 0.000443, 0.637317, 0.000037, -0.000439, 0.000595, -0.061085, 0.001997, -0.000256, 0.107902, 0.000936, -0.023785, 0.135145

**Table A.8:** Fiber orientation tensors of the specimens considered in this work.

# Bibliography

Advani, S. G., Tucker, C. L., 1987. The Use of Tensors to Describe and Predict Fiber Orientation in Short Fiber Composites. *Journal of Rheology* 31 (8), 751–784.

Anagnostou, D., Chatzigeorgiou, G., Chemisky, Y., Meraghni, F., 2018. Hierarchical micromechanical modeling of the viscoelastic behavior coupled to damage in SMC and SMC-hybrid composites. *Composites Part B: Engineering* 151, 8–24.

Arens, T., Hettlich, F., Karpfinger, C., Kockelkorn, U., Lichtenegger, K., Stachel, H., 2018. *Mathematik*, 4th Edition. Springer Spektrum.

Bauer, J., 2021a. Mechkit: Basic continuum mechanics toolkit. URL <https://github.com/JulianKarlBauer/mechkit>, date accessed: December 11 2021.

Bauer, J., 2021b. Orientation Averaged Meanfield: Sensitivity Analysis of the Compression Modulus (internal communication).

Bauer, J., Lang, J., 2021. Paramid. URL [https://git.scc.kit.edu/julian\\_e/paramid](https://git.scc.kit.edu/julian_e/paramid), date accessed: December 11 2021.

Bertram, A., 2014. *Elasticity and plasticity of large deformations: An introduction*. Springer, Berlin, Heidelberg.

Böhlke, T., Brüggemann, C., 2001. Graphical representation of the generalized Hooke's law. *Technische Mechanik* 21 (2), 145–158.

Böhlke, T., Henning, F., Hrymak, A., Kärger, L., Weidenmann, K. A., Wood, J. T., 2019. Continuous Discontinuous Fiber Reinforced Polymers An Integrated Engineering Approach. Hanser, Cincinnati, Munich.

Böhlke, T., Jöchen, K., Piat, R., Langhoff, T.-a., Tsukrov, I., Reznik, B., 2010. Elastic properties of pyrolytic carbon with axisymmetric textures. *Technische Mechanik* 30 (4), 343–353.

Brylka, B., 2017. Charakterisierung und Modellierung der Steifigkeit von langfaserverstärktem Polypropylen. Doctoral dissertation, Karlsruhe Institute of Technology (KIT).

Bücheler, D., 2017. Locally Continuous-fiber Reinforced Sheet Molding Compound. Doctoral dissertation, Karlsruhe Institute of Technology (KIT).

Cape, J., Lehman, G., 1963. Temperature and finite pulse time effects in the flash method for measuring thermal diffusivity. *Journal of Applied Physics* 34 (7), 1909–1913.

Catapano, A., Desmorat, B., Vannucci, P., 2012. Invariant formulation of phenomenological failure criteria for orthotropic sheets and optimisation of their strength. *Mathematical Methods in the Applied Sciences* 35 (15), 1842–1858.

Cecen, V., Tavman, I. H., Kok, M., Aydogdu, Y., 2009. Epoxy- and polyester-based composites reinforced with glass, carbon and aramid fabrics: Measurement of heat capacity and thermal conductivity of composites by differential scanning calorimetry. *Polymer Composites* 30 (9), 1299–1311.

Chen, Z., Tang, H., Shao, Y., Sun, Q., Zhou, G., Li, Y., Xu, H., Zeng, D., Su, X., mar 2019. Failure of chopped carbon fiber Sheet Molding Compound (SMC) composites under uniaxial tensile loading: Computational prediction and experimental analysis. *Composites Part A: Applied Science and Manufacturing* 118, 117–130.

- Coleman, B. D., Noll, W., 1963. The thermodynamics of elastic materials with heat conduction and viscosity. *Archive for Rational Mechanics and Analysis* 13 (1), 167–178.
- Colón Quintana, J. L., Teuwsen, J., Mazzei Capote, G. A., Osswald, T., 2021. Application of the stress interaction failure criterion in platelet composite compression molded parts. *Polymer Composites* 42 (7), 3632–3643.
- Cowan, R., 1963. Pulse method of measuring thermal diffusivity at high temperatures. *Journal of Applied Physics* 34 (4), 926–927.
- Cowin, S. C., 1989. Properties of the anisotropy elasticity tensor. *Quarterly Journal of Mechanics and Applied Mathematics* 42 (3), 249–266.
- Daniel, I. M., 2007. Failure of composite materials. *Applied Mechanics Reviews* 43, 4–12.
- Dano, M.-L., Gendron, G., Maillette, F., Bissonette, B., 2006. Experimental Characterization of Damage in Random Short Glass Fiber Reinforced Composites. *Journal of Thermoplastic Composite Materials* 19, 79–96.
- Desrumaux, F., Meraghni, F., Benzeggagh, M. L., 2000. Micromechanical Modelling Coupled to a Reliability Approach for Damage Evolution Prediction in Composite Materials. *Applied Composite Materials* 7, 231–250.
- Dos Santos, W. N., Mummery, P., Wallwork, A., 2005. Thermal diffusivity of polymers by the laser flash technique. *Polymer Testing* 24, 628–634.
- Eshelby, J. D., 1957. The determination of the elastic field of an ellipsoidal inclusion, and related problems. *Proceedings of the Royal Society A: Mathematical, Physical and Engineering Sciences* 241 (1226), 376–396.

- Fitoussi, J., Bourgeois, N., Guo, G., Baptiste, D., 1996a. Prediction of the anisotropic damaged behavior of composite materials: Introduction of multilocal failure criteria in a micro-macro relationship. *Computational Materials Science* 5 (1-3), 87–100.
- Fitoussi, J., Guo, G., Baptiste, D., 1996b. Determination of a tridimensional failure criterion at the fibre/matrix interface of an organic-matrix/discontinuous-reinforcement composite. *Composites Science and Technology* 56, 755–760.
- Fitoussi, J., Guo, G., Baptiste, D., 1998. A statistical micromechanical model of anisotropic damage for S.M.C. composites. *Composites Science and Technology* 58 (5), 759–763.
- Gabo, 2010. GaboQualimeter, Bedienungsanleitung für die EPLEXOR8-Software.
- Gandhi, U. N., Goris, S., Osswald, T. A., Song, Y.-Y., 2020. *Discontinuous Fiber-Reinforced Composites*. Hanser, Munich, Cincinnati.
- Gol'denblat, I. I., Kopnov, V. A., mar 1965. Strength of glass-reinforced plastics in the complex stress state. *Polymer Mechanics* 1 (2), 54–59.
- Görthofer, J., Schneider, M., Ospald, F., Hrymak, A., Böhlke, T., 2020. Computational homogenization of sheet molding compound composites based on high fidelity representative volume elements. *Computational Materials Science* 174, Article 109456.
- Grellmann, W., Seidler, S., 2011. *Kunststoffprüfung*. Hanser, Munich.
- Gross, D., Hauger, W., Wriggers, P., 2007. *Technische Mechanik 4*. Springer, Heidelberg, Dordrecht, London, New York.
- Gross, D., Seelig, T., 2007. *Bruchmechanik*. Springer, Berlin, Heidelberg.
- Hartmann, S., Gilbert, R. R., Sguazzo, C., 2018. Basic studies in biaxial tensile tests. *GAMM Mitteilungen* 41 (1), 1–14.

- Hashin, Z., Shtrikman, S., 1962. A variational approach to the theory of the elastic behaviour of polycrystals. *Journal of the Mechanics and Physics of Solids* 10 (4), 343–352.
- Haupt, P., 2002. *Continuum Mechanics and Theory of Materials*. Springer, Berlin, Heidelberg.
- Hill, R., 1952. The elastic behaviour of a crystalline aggregate. *Proceedings of the Physical Society. Section A* 65 (5), 349–354.
- Hohberg, M., Kärger, L., Bücheler, D., Henning, F., 2017. Rheological In-Mold Measurements and Characterizations of Sheet-Molding-Compound (SMC) Formulations with Different Constitution Properties by Using a Compressible Shell Model. *International Polymer Processing* 32 (5), 659–668.
- Hori, M., Nemat-Nasser, S., 1999. On two micromechanics theories for determining micro macro relations in heterogeneous solids. *Mechanics of Materials* 31, 667–682.
- Hunter, J., Dale, D., Firing, E., Droettboom, M., 2012. `matplotlib.pyplot.boxplot`, *Matplotlib 3.1.2 documentation*, URL: [https://matplotlib.org/3.1.1/api/\\_as\\_gen/matplotlib.pyplot.boxplot.html](https://matplotlib.org/3.1.1/api/_as_gen/matplotlib.pyplot.boxplot.html), date accessed: December 11 2021.
- Jendli, Z., Meraghni, F., Fitoussi, J., Baptiste, D., 2004. Micromechanical analysis of strain rate effect on damage evolution in sheet molding compound composites. *Composites Part A: Applied Science and Manufacturing* 35 (7-8), 779–785.
- Johra, H., 2019. Description of the Laser Flash Analysis Method for Thermal Diffusivity Measurement with the LFA 447, URL: <https://vbn.aau.dk/en/publications/description-of-the-laser-flash-analysis-method-for-thermal-diffus>, date accessed: November 11 2020.

Kachanov, L. M., 1958. Time of the rupture process under creep conditions. *Nank SSR Otd Tech Nauk.* 8, 26–31.

Kanatani, K.-I., 1984. Distribution of directional data and fabric tensors. *International Journal of Engineering Science* 12 (2), 149–164.

Kehrer, L., Pinter, P., Böhlke, T., 2017. Mean and full field homogenization of artificial long fiber reinforced thermoset polymers. *Proceedings in Applied Mathematics and Mechanics* 17, 603–604.

Kehrer, L., Wood, J. T., Böhlke, T., 2020. Mean-field homogenization of thermoelastic material properties of a long fiber-reinforced thermoset and experimental investigation. *Journal of Composite Materials* 54 (25), 3777–3799.

Kehrer, M. L., 2019. Thermomechanical Mean-Field Modeling and Experimental Characterization of Long Fiber-Reinforced Sheet Molding Compound Composites. Doctoral dissertation, Karlsruhe Institute of Technology (KIT).

Kia, H. G., 2008. Thermal expansion of sheet molding compound materials. *Journal of Composite Materials* 42 (7), 681–695.

Kröner, E., apr 1977. Bounds for effective elastic moduli of disordered materials. *Journal of the Mechanics and Physics of Solids* 25 (2), 137–155.

Lang, J., 2013. Experimentelle und numerische Untersuchung der inhomogenen, anisotropen, temperatur- und frequenzabhängigen Steifigkeit von SMC. Bachelor thesis. Unpublished thesis. Supervised by Brylka, B, and Böhlke, T., Karlsruhe Institute of Technology (KIT), Institute of Engineering Mechanis, Chair for Continuum Mechanics.

Lang, J., Schemmann, M., Böhlke, T., 2019. Anisotropic Stiffness Degradation in Biaxial Tensile Testing of SMC. *Proceedings in Applied Mathematics and Mechanics* 19 (1), 31–32.

Lang, J., Schemmann, M., Seelig, T., Böhlke, T., 2018. Investigations of Cruciform Specimen Designs for Biaxial Tensile Testing of SMC. *Proceedings of the 18th International Conference on Experimental Mechanics 2* (8), Article 411.

Lemaitre, J., 1992. *A Course on Damage Mechanics*. Springer, Berlin, Heidelberg.

Lemaitre, J., Chaboche, J.-L., 1990. *Mechanics of Solid Materials*. Cambridge University Press, Cambridge.

Li, S., Sitnikova, E., Liang, Y., Kaddour, A. S., nov 2017. The Tsai-Wu failure criterion rationalised in the context of UD composites. *Composites Part A: Applied Science and Manufacturing* 102, 207–217.

Lubliner, J., Papadopoulos, P., 2014. *Introduction to Solid Mechanics*. Springer, New York.

McCormick, N., Lord, J., 2010. Digital Image Correlation. *Materials today* 13 (12), 52–54.

Mehta, G., Mohanty, A. K., Thayer, K., Misra, M., Drzal, L. T., 2005. Novel biocomposites sheet molding compounds for low cost housing panel applications. *Journal of Polymers and the Environment* 13 (2), 169–175.

Meraghni, F., Benzeggagh, M. L., 1995. Micromechanical modelling of matrix degradation in randomly oriented discontinuous-fibre composites. *Composites Science and Technology* 55 (2), 171–186.

Meraghni, F., Blakeman, C. J., Benzeggagh, M. L., 1996. Effect of interfacial decohesion on stiffness reduction in a random discontinuous-fibre composite containing matrix microcracks. *Composites Science and Technology* 56 (5), 541–555.

Meyer, N., Schöttl, L., Bretz, L., Hrymak, A. N., Kärger, L., 2020. Direct Bundle Simulation approach for the compression molding process of Sheet Molding Compound. *Composites Part A: Applied Science and Manufacturing* 132.

Mir, H., Fafard M., Bissonette, B., Dano, M.-L., 2005. Damage Modeling in Random Short Glass Fiber Reinforced Composites Including Permanent Strain and Unilateral Effect. *Journal of Applied Mechanics* 72, 249–258.

Mori, T., Tanaka, K., 1973. Average stress in matrix and average elastic energy of materials with misfitting inclusions. *Acta Metallurgica* 21 (5), 571–574.

Müller, V., 2015. Micromechanical modeling of short-fiber reinforced composites. Doctoral dissertation, Karlsruhe Institute of Technology (KIT).

Müller, V., Böhlke, T., 2016. Prediction of effective elastic properties of fiber reinforced composites using fiber orientation tensors. *Composites Science and Technology* 130, 36–45.

Müller, W., 2011. *Streifzüge durch die Kontinuumstheorie*. Springer-Verlag, Heidelberg, Dordrecht, London, New York.

Mura, T., 1987. *Micromechanics of defects in solids*. Springer, Dordrecht.

Murali, M., Finosh, G. T., Jayabalan, M., 2013. Studies on Biodegradable Polymeric Nanocomposites Based on Sheet Molding Compound for Orthopedic Applications. *Advances in Materials Science and Applications* 2 (2), 73–87.

Neitzel, M., Mitschang, P., 2004. *Handbuch Verbundwerkstoffe*. Carl Hanser Verlag München Wien.

- Nemat-Nasser, S., Hori, M. M., 1999. *Micromechanics: overall properties of heterogeneous materials*. North-Holland Series in Applied Mathematics and Mechanics, Amsterdam, London, New York, Tokyo.
- NETZSCH, 2021. *Light Flash Apparatus*. Product brochure LEA 467 HyperFlash Series. NETZSCH-Gerätebau GmbH, Selb.
- Oldenbo, M., Gernbergc, S. P., Berglundd, L. A., 2003. Mechanical behavior of smc composites with toughening and low density additives. *Composites Part A Applied Science and Manufacturing* 34 (9), 875–885.
- Orgéas, L., Dumont, P. J. J., 2011. *Sheet Molding Compounds*. Wiley Encyclopedia of Composites 5, 2683–2718.
- Osswald, P. V., Osswald, T. A., 2018. A strength tensor based failure criterion with stress interactions. *Polymer Composites* 39 (8), 2826–2834.
- Pang, S.-S., Pandian, A., Bradshaw, R. D., 1992. Modified Tsai-Wu Failure Criterion. *Polymer Composites* 13 (4), 273–277.
- Parker, W. J., Jenkins, R. J., Butler, C. P., Abbott, G. L., 1961. Flash Method of Determining Thermal Diffusivity, Heat Capacity, and Thermal Conductivity. *Journal of Applied Physics* 32, 1679–1684.
- Pinter, P., Dietrich, S., Bertram, B., Kehrer, L., Elsner, P., Weidenmann, K. A., 2018. Comparison and error estimation of 3D fibre orientation analysis of computed tomography image data for fibre reinforced composites. *NDT and E International* 95, 26–35.
- Python NumPy Developers, 2022. `numpy.polyfit`, URL: <https://numpy.org/doc/stable/reference/generated/numpy.polyfit.html>, date accessed: January 14, 2022.
- Rabotnov, Y. N., 1969. Creep Rupture. In: Hetényi, M., Vincenti, W. G. (Eds.), *Applied Mechanics*. Proceedings of the Twelfth International Congress of Applied Mechanics. Springer, Berlin, Heidelberg.

Reddy, N., 2015. A review on completely biodegradable composites developed using soy-based matrices. *Journal of Reinforced Plastics and Composites* 34 (18), 1457–1475.

Reuss, A., 1929. Berechnung der Fließgrenze von Mischkristallen auf Grund der Plastizitätsbedingung für Einkristalle. *Journal of Applied Mathematics and Mechanics / Zeitschrift für Angewandte Mathematik und Mechanik* 9 (1), 49–58.

Reyers, A., 2018. Design for success: a design and technology manual for SMC BMC, URL: [https://smcbmc-europe.org/design\\_for\\_success/rapport\\_design\\_for\\_success.pdf](https://smcbmc-europe.org/design_for_success/rapport_design_for_success.pdf), date accessed: October 26 2020.

Ribeiro, M. C., Reis, J. M., Ferreira, A. J., Marques, A. T., 2003. Thermal expansion of epoxy and polyester polymer mortars - Plain mortars and fibre-reinforced mortars. *Polymer Testing* 22 (8), 849–857.

Rosendahl, P. L., 2020. *From Bulk to Structural Failure: Fracture of Hyperelastic Materials*. Springer Vieweg.

Salazar, A., 2003. On thermal diffusivity. *European Journal of Physics* 24 (4), 351–358.

Schemmann, M., Gajek, S., Böhlke, T., 2018a. Biaxial Tensile Tests and Microstructure-Based Inverse Parameter Identification of Inhomogeneous SMC Composites. *Advanced Structured Materials* 80, 329–342.

Schemmann, M., Görthofer, J., Seelig, T., Hrymak, A., Böhlke, T., 2018b. Anisotropic meanfield modeling of debonding and matrix damage in SMC composites. *Composites Science and Technology* 161, 143–158.

Schemmann, M., Lang, J., Helfrich, A., Seelig, T., Böhlke, T., 2018c. Cruciform Specimen Design for Biaxial Tensile Testing of SMC. *Journal of Composites Science* 2 (1), Article 12.

Schlüter, M., Egea, J. A., Banga, J. R., 2009. Extended ant colony optimization for non-convex mixed integer nonlinear programming. *Computers and Operations Research* 36 (7), 2217–2229.

Schmidt, C., 2019. Characterization of the anisotropic damage behavior of SMC. Bachelor thesis. Unpublished thesis. Supervised by Lang, J. and Böhlke, T., Karlsruhe Institute of Technology (KIT), Institute of Engineering Mechanics, Chair for Continuum Mechanics.

Schöttl, L., Dörr, D., Pinter, P., Weidenmann, K. A., Elsner, P., Kärger, L., 2020. A novel approach for segmenting and mapping of local fiber orientation of continuous fiber-reinforced composite laminates based on volumetric images. *NDT & E international* 110, Article 102194.

Schöttl, L., Weidenmann, K. A., Sabiston, T., Inal, K., Elsner, P., jan 2021. Fiber bundle tracking method to analyze sheet molding compound microstructure based on computed tomography images. *NDT & E international* 117, Article 102370.

Schulenberg, L., Seelig, T., Andrieux, F., Sun, D. Z., 2017. An anisotropic elasto-plastic material model for injection-molded long fiber-reinforced thermoplastics accounting for local fiber orientation distributions. *Journal of Composite Materials* 51 (14), 2061–2078.

Schwiedrzik, J. J., Wolfram, U., Zysset, P. K., 2013. A generalized anisotropic quadric yield criterion and its application to bone tissue at multiple length scales. *Biomechanics and Modeling in Mechanobiology* 12 (6), 1155–1168.

Serna Moreno, M., Martínez Vicente, J., López Cela, J., 2013. Failure strain and stress fields of a chopped glass-reinforced polyester under biaxial loading. *Composite Structures* 103, 27–33.

Shimamura, A., Hotta, Y., Hyuga, H., Hotta, M., Hirao, K., 2020. Improving the thermal conductivity of epoxy composites using a combustion-synthesized aggregated  $\beta$ -Si<sub>3</sub>N<sub>4</sub> filler with randomly oriented grains. *Scientific Reports* 10 (1), 1–9.

Shirinbayan, M., Fitoussi, J., Abbasnezhad, N., Meraghni, F., Surowiec, B., Tcharkhtchi, A., 2017a. Mechanical characterization of a Low Density Sheet Molding Compound (LD-SMC): Multi-scale damage analysis and strain rate effect. *Composites Part B: Engineering* 131, 8–20.

Shirinbayan, M., Fitoussi, J., Bocquet, M., Meraghni, F., Surowiec, B., Tcharkhtchi, A., 2017b. Multi-scale experimental investigation of the viscous nature of damage in Advanced Sheet Molding Compound (A-SMC) submitted to high strain rates. *Composites Part B: Engineering* 115, 3 – 13.

Smits, A., Van Hemelrijck, D., Philippidis, T. P., Cardon, a., 2006. Design of a cruciform specimen for biaxial testing of fibre reinforced composite laminates. *Composites Science and Technology* 66 (7-8), 964–975.

Taggart, D. G., Pipes, R. B., Blake, R. A., Gillespie JR., J. W., Prabhakaran, R., Whitney, J., 1979. *Properties of SMC Composites*. Center for Composite Materials, University of Delaware, Delaware.

Talreja, R., Singh, C. V., 2012. *Damage and Failure of Composite Materials*. Cambridge University Press, Cambridge.

Tang, H., Chen, Z., Xu, H., Liu, Z., Sun, Q., Zhou, G., Yan, W., Han, W., Su, X., nov 2020. Computational micromechanics model based failure criteria for chopped carbon fiber sheet molding compound composites. *Composites Science and Technology* 200, Article 108400.

Torquato, S., 2002. *Random Heterogeneous Materials: Microstructure and Macroscopic Properties*. Springer, New York.

- Trauth, A., 2018. Characterisation and Modelling of Continuous-Discontinuous Sheet Moulding Compound Composites for Structural Applications. Doctoral dissertation, Karlsruhe Institute of Technology (KIT).
- Truesdell, C., Toupin, R., 1960. Encyclopedia of Physics: Principles of Thermodynamics and Statics. Springer, Berlin, Heidelberg.
- Tsai, S. W., Wu, E. M., 1971. Theory of Strength for Anisotropic Materials. *Journal of Composite Materials* 5, 58–80.
- Urapakam Ramakrishnan, M., Mallick, P. K., 2019. Strength and failure characteristics of a glass fiber SMC-R composite under combined tensile and shear stresses. *Composites Part B: Engineering* 176, Article 107141.
- Van Hemelrijck, D., Ramault, C., Makris, A., Clarke, A., Williamson, C., Gower, M., Shaw, R., Mera, R., Lamkanfi, E., Van Paepegem, W., 2007. Biaxial Testing of Fibre Reinforced Composites. Proceedings of the 16th International Conference on Composite Materials, Kyoto, Japan 2, 750–751.
- Van Paepegem, W., Degrieck, J., 2003. Calculation of damage-dependent directional failure indices from the Tsai-Wu static failure criterion. *Composites Science and Technology* 63 (2), 305–310.
- Voigt, W., 1889. Ueber die Beziehung zwischen den beiden Elasticitätsconstanten isotroper Körper. *Annalen der Physik* 274 (12), 573–587.
- Wehrle, F., 2020. Investigation of the Thermomechanical Properties of SMC with Laser Flash Analysis. Bachelor Thesis. Unpublished thesis. Supervised by Lang, J., Kehrer, M. L., and Böhlke, T., Karlsruhe Institute of Technology (KIT), Institute of Engineering Mechanics, Chair for Continuum Mechanics.
- Wu, E. M., 1972. Optimal Experimental Measurement of Anisotropic Failure Tensors. *Journal of Composite Materials* 6, 472–489.

Yoneyama, S., Murasawa, G., 2000. Digital Image Correlation. In: Encyclopedia of Life Support Systems (EOLSS). URL: [https://www.eolss.net/ebooklib/sc\\_cart.aspx?File=E6-194-04](https://www.eolss.net/ebooklib/sc_cart.aspx?File=E6-194-04), date accessed: July 09 2016.

Zheng, Q. S., Du, D. X., 2001. An explicit and universally applicable estimate for the effective properties of multiphase composites which accounts for inclusion distribution. *Journal of the Mechanics and Physics of Solids* 49 (11), 2765–2788.





**Schriftenreihe Kontinuumsmechanik im Maschinenbau  
Karlsruher Institut für Technologie (KIT)  
(ISSN 2192-693X)**

---

- Band 1** Felix Fritzen  
**Microstructural modeling and computational homogenization of the physically linear and nonlinear constitutive behavior of micro-heterogeneous materials.**  
ISBN 978-3-86644-699-1
- Band 2** Rumena Tsotsova  
**Texturbasierte Modellierung anisotroper Fließpotentiale.**  
ISBN 978-3-86644-764-6
- Band 3** Johannes Wippler  
**Micromechanical finite element simulations of crack propagation in silicon nitride.**  
ISBN 978-3-86644-818-6
- Band 4** Katja Jöchen  
**Homogenization of the linear and non-linear mechanical behavior of polycrystals.**  
ISBN 978-3-86644-971-8
- Band 5** Stephan Wulfinghoff  
**Numerically Efficient Gradient Crystal Plasticity with a Grain Boundary Yield Criterion and Dislocation-based Work-Hardening.**  
ISBN 978-3-7315-0245-6
- Band 6** Viktor Müller  
**Micromechanical modeling of short-fiber reinforced composites.**  
ISBN 978-3-7315-0454-2

- Band 7** Florian Rieger  
**Work-hardening of dual-phase steel.**  
ISBN 978-3-7315-0513-6
- Band 8** Vedran Glavas  
**Micromechanical Modeling and Simulation  
of Forming Processes.**  
ISBN 978-3-7315-0602-7
- Band 9** Eric Bayerschen  
**Single-crystal gradient plasticity with an accumulated  
plastic slip: Theory and applications.**  
ISBN 978-3-7315-0606-5
- Band 10** Bartholomäus Brylka  
**Charakterisierung und Modellierung der Steifigkeit von  
langfaserverstärktem Polypropylen.**  
ISBN 978-3-7315-0680-5
- Band 11** Rudolf Neumann  
**Two-Scale Thermomechanical Simulation  
of Hot Stamping.**  
ISBN 978-3-7315-0714-7
- Band 12** Mauricio Lobos Fernández  
**Homogenization and materials design of mechanical  
properties of textured materials based on zeroth-,  
first- and second-order bounds of linear behavior.**  
ISBN 978-3-7315-0770-3
- Band 13** Malte Schemmann  
**Biaxial Characterization and Mean-field Based Damage  
Modeling of Sheet Molding Compound Composites.**  
ISBN 978-3-7315-0818-2
- Band 14** Jürgen Albiez  
**Finite element simulation of dislocation  
based plasticity and diffusion in multiphase  
materials at high temperature.**  
ISBN 978-3-7315-0918-9

- Band 15** Maria Loredana Kehrer  
**Thermomechanical Mean-Field Modeling and Experimental Characterization of Long Fiber-Reinforced Sheet Molding Compound Composites.**  
ISBN 978-3-7315-0924-0
- Band 16** Peter Hölz  
**A dynamic and statistical analysis of the temperature- and fatigue behavior of a race power unit – The effect of different thermodynamic states.**  
ISBN 978-3-7315-0988-2
- Band 17** Andreas Prahs  
**A Gradient Crystal Plasticity Theory Based on an Extended Energy Balance.**  
ISBN 978-3-7315-1025-3
- Band 18** Johannes Ruck  
**Modeling martensitic phase transformation in dual phase steels based on a sharp interface theory.**  
ISBN 978-3-7315-1072-7
- Band 19** Hannes Erdle  
**Modeling of Dislocation - Grain Boundary Interactions in Gradient Crystal Plasticity Theories.**  
ISBN 978-3-7315-1196-0
- Band 20** Johannes Görthofer  
**Microstructure generation and micromechanical modeling of sheet molding compound composites.**  
ISBN 978-3-7315-1205-9
- Band 21** Daniel Wicht  
**Efficient fast Fourier transform-based solvers for computing the thermomechanical behavior of applied materials.**  
ISBN 978-3-7315-1220-2
- Band 22** Juliane Lang  
**Thermomechanical Modeling and Experimental Characterization of Sheet Molding Compound Composites.**  
ISBN 978-3-7315-1232-5

Sheet molding compound (SMC) composites belong to the fiber reinforced plastics and are a versatile high-performance class of materials. The aim of this work is to model and experimentally characterize the thermomechanical material behavior of SMC composites on the macroscale with consideration of the microstructure. The unified approach of modeling and experiments is significant to this work. Anisotropic temperature-dependent thermoelastic material behavior and failure behavior are considered in the modeling. To account for microstructure, the material coefficients are expressed in terms of fiber orientation tensors. Experiments with various testing devices are performed, including temperature-dependent investigations of the thermoelastic properties. A focus of the experiments is on biaxial damage and failure investigations using special cruciform tensile specimens with reinforced arms. Using the experimental results in combination with microstructural information taken from micro-CT scans, the model parameters are determined. Thus, with the model containing the determined parameters, all material properties considered can be calculated if the microstructure is known. The model is applied to sample specimens whose microstructure is obtained from micro-CT scans. To validate the whole process, those modeled results are compared with experimentally determined properties of the sample specimens.

ISSN 2192-693X

ISBN 978-3-7315-1232-5

Gedruckt auf FSC-zertifiziertem Papier

